Structural and Deformation Heterogeneities of Chemically Complex Multicomponent Alloys

A Dissertation Presented for the

Doctor of Philosophy

Degree

The University of Tennessee, Knoxville

Tingkun Liu

August 2019

DEDICATION

I dedicate this work to my parents and my wife, for their love and supports.

ACKNOWLEDGEMENTS

First and foremost, I would like to express my sincere appreciation to adviser Dr. Yanfei Gao for his support, guidance, criticism and encouragement throughout my entire graduate research work. I would also like to thank my co-advisor, Dr. Hongbin Bei, for his valuable suggestions and generous aids. It has been a great pleasure to work with him during my time at Oak Ridge National Laboratory.

I am also very thankful to my committee members. I would like to thank Dr. Hahn Choo, Dr. Claudia Rawn and Dr. Anming Hu for serving on my committee, providing critical comments and suggestions on the research work.

My special appreciation goes to Dr. Ke An at Spallation Neutron Source, where I spend most of time conducting neutron diffraction experiments. Thanks to his enormous support and devotional help both on my academic and personal life. I am also grateful to Dr. Yanwen Zhang for her help with ion irradiation experiments, data analysis and discussions.

Many thanks are also given to fellow graduate students, postdoctoral researchers and staff members. Thanks to group members, past and present, including Dr. Chao Pu, Dr. Wei Zhang, Mr. Liubin Xu, Mrs. Xue Wang and Mrs. Di Xie for their help and friendship. Great appreciation also goes to Dr. Zhenggang Wu, Dr. Yan Chen, Dr. Dunji Yu, Dr. Qingge Xie, Dr. Ke Jin, Dr. Yang Tong, Dr. Wei Guo for their experimental support and discussion on scientific issues.

Lastly but not the least, my thanks go to my parents and my wife who have been supporting me financially and spiritually at every stage of my life.

ABSTRACT

In the long history of alloy design, bulk metallic glasses (BMGs) and high entropy alloys (HEAs) are two new classes of chemically complex multicomponent alloys with unique structures and promising properties as the structural and functional materials. Due to the nature of dynamic structure at the atomistic scale, structural heterogeneities in BMGs play a significant role during deformation as plastic flow carriers. Hence, deformation heterogeneities occur as shear banding causes fatal failure in these amorphous alloys. However, the nature of structure and ductilization mechanism of BMGs is still not fully understood. On the other hand, different deformation heterogeneities exist in crystalline alloys, such as planar slip, twinning and stress-driven phase transformation. As a newer class of materials, more investigations are necessary for understanding deformation behaviors in HEAs, which although have gained extensive investigation of deformation behaviors by applying conventional strengthening methods as well as twinning or phase-transformation induced plasticity (TWIP/TRIP).

In this dissertation, we investigated the structural and deformation heterogeneities in BMGs and HEAs. The structural heterogeneities in BMGs were induced by elastic/plastic deformation and ion irradiation. Nanoindentation pop-in tests were performed to probe the atomistic structure which was quantitively evaluated by numerical study of a unified model. The computational method was proposed by unifying the homogenous shear band nucleation process and heterogeneous shear band nucleation process to characterize the defects as the plastic flow carriers structurally and mechanically. It turns out that deformation induce defect is effective to tuning the amorphous structure in

BMGs. Neutron diffraction was utilized to study behaviors of the deformation twinning and texture evolution during tensile deformation at different temperatures in TWIP HEAs. The deformation induced microstructure and texture change of CoCrFeMnNi alloy was investigated by multiple interrupted cryogenic tensile tests. The micromechanical behavior of carbon strengthened CoCrFeMnNi0.5C HEAs was studied by in situ neutron diffraction. Combined with microstructure observation, the role of dislocation slips and twinning of work hardening was clarified. Consequently, the current research provides insights into a deep understanding of structure-property relationship of these two classes of chemically complex multicomponent alloys.

TABLE OF CONTENTS

LIST OF TABLES

LIST OF FIGURES

INTRODUCTION

Research background

Alloying is the most powerful and effective method in the thousand-year history of metallurgy. Until 1960s, the first metallic glass was produced by being cooled rapidly from the liquid state at a rate of around 106 K/s to avoid crystallization and possess non-crystalline or glass-like structure [1]. Another milestone of MGs is the discovery of the bulk metallic glass (BMG) in the 1990s [2]. Metallic glasses or called amorphous metals/alloys are novel engineering alloys with unique structures: on the one hand, MGs are amorphous materials without long-range structural order; on the other hand, topological and chemical short-to-medium range order is expected to be pronounced in these alloys account to their high atomic packing density and the varying chemical affinity among the constituent elements. Bulk metallic glasses (BMGs) are chemically complex, usually contains more than three elements. They are formed at very low critical cooling rates, which is fundamentally different from traditional MGs formed at very high cooling rates in order to suppress the nucleation of crystalline phases. BMGs do not have the crystalline defects i.e. dislocations that govern many of the mechanical properties of more common alloys. In this scenario the challenge in understanding properties and behaviors comes about because it is much more difficult to characterize the structure defects. Through extensive research, some theories have been proposed such as free volume model, shear transformation zone (STZ) model and local density function model [3, 4].

Yet, a new class of materials, high entropy alloy (HEA) was proposed more recently, which is described as a multi-component metallic solid solution containing at least five equimolar principle elements with simple face-centered cubic (FCC), body-

centered cubic (BCC), or hexagonal close-packed (HCP) structures [5-8]. Being different from the conventional alloys, compositions in HEAs are complex due to the equimolar concentration of each component. The four core effects for HEAs were summarized, that is: (1) high-entropy effects; (2) sluggish diffusion; (3) lattice distortion; and (4) cocktail effects [9]. The high entropy tends to stabilize the high-entropy phases, i.e., solid-solution phases, rather than intermetallic phases. Sluggish diffusion leads to the alloys developing nano-sized precipitates or even amorphous structures. Lattice distortion further influences mechanical, physical and chemical properties. Finally, the cocktail effects result in a composite effect on properties, wherein the interactions among the different elements themselves play an important role. All of the aforementioned factors provide HEAs with numerous versatile properties and therefore make them suitable for a number of applications.

Due to the unique atomistic structure, both of these two classes of chemically complex multicomponent alloys exhibit outstanding mechanical properties such as high strength and fracture toughness [10], which make them promising structural materials in engineering applications. BMGs have attracted numerous studies due to superior mechanical properties including high strength, high hardness, high toughness and excellent corrosion resistance [11-15]. But the low ductility has been a major concern in the engineering application. Pre-deformation and irradiation have been found to be effective methods to enhance ductility by increasing structural heterogeneities [16-18]. However, the underlying mechanism of deformation and irradiation induced structural heterogeneities is not clear and their effects on deformation behaviors has not been fully

understood. CrCoFeMnNi is one of the most widely studied HEAs, which is single phase solid solution with simple face centered cubic structure [19]. Nano-twinning is activated during the cryogenic deformation [19, 20]. But the mechanism of this phenomenon is still under discussion. Furthermore, the addition of carbon even activates twinning during ambient deformation [21]. Even though twinning activity is highly grain-orientation dependent, deformation induced texture evolution has rarely been studied so far. The profound and complete understanding of the relationship connecting the property, microstructure and bulk texture in the CrCoFeMnNi HEA is lacking.

Research objectives

The general objective of this work is to understand the fundamental deformation mechanisms in these two classes of advanced engineering alloys. Both BMGs and HEAs have unique structures at the length scales of micro- and nanometers, and exhibit unique properties, which make them potential materials for structural applications. To investigate their deformation behaviors, the current proposal is divided by two parts as follows:

1) Elastic/plastic deformation and irradiation induced rejuvenation in Zr-based bulk metallic glasses.

The objective of this part is to study the deformation mechanism of elastically and plastically deformed BMGs in atomistic length scale, and to investigate the deformation mechanism of ion irradiated BMGs aiming to identify the crucial physical factors to characterize the extrinsically induced structural heterogeneities. The study of deformation and irradiation induced structure-property relationship improves the understanding of structural heterogeneity and rejuvenation behaviors in BMGs.

2) Deformation mechanism and texture evolution in CrCoFeMnNi high entropy alloys and carbon effect.

The objective of this work is to study the deformation mechanism and texture evolution of CrCoFeMnNi HEAs in cryogenic tensile deformation and deformation mechanism of carbon containing HEAs CrCoFeMnNi0.5C at room temperature and elevated temperature. This study provides a profound and complete understanding of the relationship connecting the property, microstructure and bulk texture and the carbon effect on twinning activity in the CrCoFeMnNi HEA.

Thesis overview

This dissertation is organized such that each chapter can be a standalone document based on four journal articles. The present section introduces the research background, objectives and the organization of this dissertation. The first article in Chapter 1 is "Probing Elastically or Plastically Induced Structural Heterogeneities in Bulk Metallic Glasses by Nanoindentation Pop-In Tests", published in *AIP Advance*s in 2017. In Chapter 2, the second article in the title of "Effect of Ion Irradiation on Structural and Mechanical Changes in A Zr-base Metallic Glass" will be submitted to *Acta Materialia*. Chapter 3 presents the article "Twinning-mediated Work Hardening and Texture Evolution in CrCoFeMnNi High Entropy Alloys at Cryogenic Temperature," as published in *Materials & Design* in 2017. The last chapter in this dissertation, Chapter 4 is based on the article published in *Journal of Materials Research* in 2018, titled by "In Situ Neutron Diffraction Study on Tensile Deformation Behavior of Carbon Strengthened CoCrFeMnNi High Entropy Alloys at Room and Elevated Temperatures". The focus of these four articles is

the deformation behaviors of two kinds of chemically complex multicomponent alloys, BMGs and HEAs, which provides insight of understanding their structure-property relationship.

References

[1] W. Klement, R.H. Willens, P. Duwez, Nature, 187 (1960) 869-870.

[2] A. Peker, W.L. Johnson, Appl Phys Lett, 63 (1993) 2342-2344.

[3] A.S. Argon, Acta Metall Mater, 27 (1979) 47-58.

[4] D. Srolovitz, T. Egami, V. Vitek, Phys Rev B, 24 (1981) 6936-6944.

[5] J.W. Yeh, S.K. Chen, S.J. Lin, J.Y. Gan, T.S. Chin, T.T. Shun, C.H. Tsau, S.Y. Chang, Adv Eng Mater, 6 (2004) 299-303.

[6] C.J. Tong, M.R. Chen, S.K. Chen, J.W. Yeh, T.T. Shun, S.J. Lin, S.Y. Chang, Metall Mater Trans A, 36a (2005) 1263-1271.

[7] M.A. Hemphill, T. Yuan, G.Y. Wang, J.W. Yeh, C.W. Tsai, A. Chuang, P.K. Liaw, Acta Mater, 60 (2012) 5723-5734.

[8] M.C. Gao, B. Zhang, S.M. Guo, J.W. Qiao, J.A. Hawk, Metall Mater Trans A, 47a (2016) 3322-3332.

[9] J.W. Yeh, Ann Chim-Sci Mat, 31 (2006) 633-648.

[10] B. Gludovatz, A. Hohenwarter, D. Catoor, E.H. Chang, E.P. George, R.O. Ritchie, Science, 345 (2014) 1153-1158.

[11] J. Schroers, W.L. Johnson, Phys Rev Lett, 93 (2004).

[12] C.A. Schuh, T.C. Hufnagel, U. Ramamurty, Acta Mater, 55 (2007) 4067-4109.

[13] G. Kumar, H.X. Tang, J. Schroers, Nature 457(7231) (2009) 868.

[14] A. Inoue, A. Takeuchi, Acta Mater., 59(6) (2011) 2243-2267.

[15] M.D. Demetriou, M.E. Launey, G. Garrett, J.P. Schramm, D.C. Hofmann, W.L. Johnson, R.O. Ritchie, Nature materials 10(2) (2011) 123.

[16] Y. Tong, T. Iwashita, W. Dmowski, H. Bei, Y. Yokoyama, T. Egami, Acta Mater, 86 (2015) 240-246.

[17] W. Dmowski, T. Iwashita, C.P. Chuang, J. Almer, T. Egami, Phys Rev Lett, 105 (2010).

[18] L. Wang, H. Bei, Y.F. Gao, Z.P. Lu, T.G. Nieh, Acta Mater, 59 (2011) 7627-7633.

[19] J.W. Yeh, S.K. Chen, S.J. Lin, J.Y. Gan, T.S. Chin, T.T. Shun, C.H. Tsau, S.Y. Chang, Adv Eng Mater, 6 (2004) 299-303.

[20] B. Gludovatz, A. Hohenwarter, D. Catoor, E.H. Chang, E.P. George, R.O. Ritchie, Science, 345 (2014) 1153-1158.

[21] Z. Wu, C.M. Parish, H. Bei, J Alloy Compd, 647 (2015) 815-822.

CHAPTER I

PROBING ELASTICALLY OR PLASTICALLY INDUCED STRUCTURAL HETEROGENEITIES IN BULK METALLIC GLASSES BY NANOINDENTATION POP-IN TESTS

A version of this chapter was originally published by Tingkun Liu, Yanfei Gao, and Hongbin Bei in 2017:

Tingkun Liu, Yanfei Gao, and Hongbin Bei. "Probing elastically or plastically induced structural heterogeneities in bulk metallic glasses by nanoindentation pop-in tests." AIP Advances 7.8 (2017): 085216.

Authors:

Tingkun Liu

Materials Science and Engineering Department, University of Tennessee, Knoxville, TN 37996, USA

Yanfei Gao, Hongbin Bei

Materials Science and Engineering Department, University of Tennessee, Knoxville, TN 37996, USA; and Materials Science and Technology Division, Oak Ridge National Laboratory, Oak Ridge, TN 37831, USA

Tingkun Liu's contributions in the article: designed and conducted experiments, analyzed the experimental data, wrote and revised the article.

Co-authors' contributions are listed as follows: Hongbin Bei assisted with the direction of this work, the operation of nanoindentation tests and the discussion of data. Yanfei Gao provided research guidelines and worked with Tingkun Liu to analyze the experimental data, the calculation procedure and revised the article.

Abstract

Shear banding dynamics in bulk metallic glasses (BMGs) is manifested by the spatiotemporal evolution of strain fields which in turn depend on structural heterogeneities. The spacing of these heterogeneities, as a characteristic length scale, was determined from the analysis of nanoindentation pop-in tests using a stochastic model. Furthermore, the pre-stress by elastic bending and residual stress by plastic bending of BMG plates were found to dramatically decrease such spacings, thus increasing heterogeneity density and mechanically rejuvenating the glass structure.

1. Introduction

The amorphous nature of the atomic structure of bulk metallic glasses (BMGs) and their promising mechanical properties make them competitive materials for structural applications. However, the biggest challenge limiting the use of BMGs is their catastrophic failure caused by strain localization into shear bands (SBs) at temperatures far below their glass transition temperatures, especially in uniaxial tension [1, 2]. It is now well accepted that SBs usually initiate at local structural heterogeneities, e.g., shear transformation zones (STZs) or regions with high free volume [3-5]. At present, there has been a wide range of research to probe these local structural heterogeneities computationally and experimentally [6-10]. For example, recent studies suggest the scenario of a cooperative rearrangement of nanoscale/atomic structural heterogeneities overcoming a local energy barrier or called β-relaxation which is closely related to the formation of STZs in the view of energy landscape [11, 12]. Some other studies suggest the presence of local elastic heterogeneities with the

size of a few Angstroms and the spacing of a few nanometers [13, 14]. Lacking well defined configurational defects, the nature of dynamic amorphous structure and direct observation of local structural heterogeneities still remain unclear even nowadays.

To study the structural aspects of plasticity mechanisms, it requires the knowledge of how SBs initiate at these structural heterogeneities and the spatiotemporal distributions of these activated heterogeneities. It is usually found that as-cast BMGs have more pronounced ductility than the annealed ones, suggesting that annealing "relaxes" the atomic structure and removes the structural heterogeneities [15-17]. Due to the nature of thermally activated processes in BMGs, temperature, as well as mechanical stress, affects their atomic structural evolution. Therefore, it is anticipated that the structural heterogeneities can also be introduced, e.g., by a macroscopically homogeneous deformation via compressing the BMG at temperatures slightly below the glass transition temperature. Using high-energy X-ray diffraction and anisotropic pair density function, it is found that the above "rejuvenation" arises from the increase of structural disordering, or more precisely, the local changes in the atomic connectivity network [18, 19]. Similar rejuvenation can be realized thermally by re-heating samples above the glass transition temperature. More recently, it is also found that the drop of both the stress required to initiate a shear band and the shear band propagation velocity were derived from rejuvenation by severe plastic deformation, but the population of shear bands was attributed to the residual stresses rather than rejuvenation [20]. The residual stress was also found to reduce the size of STZ in a different metallic glass [21].

In the above studies of intrinsic ductility enhancement [10-14, 18-20], however, a direct connection or evolution of such nanoscale heterogeneities and the eventual SBs cannot be determined. From these activated heterogeneities, the resulting inhomogeneous strain fields will evolve, both spatially and temporally, until one or several major shear bands appear. Moreover, these efforts based on the high-energy X-ray diffraction do not provide a length scale of the structural rejuvenation [18]. On much larger scales, results obtained by in-situ digital image correlation (DIC) show distinct fluctuations and irreversible local strains before the onset of macroscopic yielding, suggesting that spatiotemporal fluctuations might be related to the spacing of these intrinsic activated structural heterogeneities [22]. These results also indicate that the evolution history and characteristics of local strain fields play an important role in the subsequent initiation of shear bands. Due to the resolution limit (~10μm) of DIC measurement, the spacing of these activated heterogeneities has not been determined.

The vast spatial gap between the above atomic heterogeneities and the full dynamics revealed by the DIC technique can be bridged by a quantitative nanoindentation pop-in test. As a structural probe technique in nanoscale, nanoindentation has been widely utilized to investigate deformation behaviors of BMGs; for instance, the pop-in tests were successfully applied to characterize the structural heterogeneity [23, 24].

In addition, this work further extends to investigate how the mechanical rejuvenation affects the spacing of the activated structural heterogeneities, in which we elastically bend a BMG plate and keep it in a ring frame, and plastically bend a BMG plate and then unload. Even though the effects of plastic deformation on the hardness and onset

of yield in BMGs were studied using indentation testing [25] and the local strain fields induced by elastic and plastic deformation were measured by synchrotron diffraction [26], these studies do not establish a structure-property relationship to understand the effect of pre-stress or residual stress on deformation behaviors in BMGs. In the present work, nanoindentation experiments were employed to measure the pop-in stresses representing the onset of plasticity. A stochastic model was used to investigate the activated structural heterogeneities induced by prior elastic or plastic deformation. Pre-stress and residual stress induced structure-property relationship was presented to improve the understanding of structural heterogeneity and rejuvenation behaviors in BMGs.

2. Materials and experiments

A metallic glass with a nominal composition of $Zr_{52.5}Al_{10}Ti_5Cu_{17.9}Ni_{14.6}$ (BMG-11) was fabricated by arc melting and subsequent drop casting. Two thin plate samples with the thickness of 1.5 mm and 2.5 mm, denoted as A and B, were cut from the cast rod with a diameter of 7 mm by electrical discharge machining. Sample A was elastically bent and constrained in a steel ring with an internal diameter of 15mm. Sample B was plastically loaded by three-point bending beyond yielding and then unloaded. The side surfaces of sample A and B were observed using scanning electron microscopy after deformation as shown in Fig. 1.1 (all tables and figures are located in the appendix). Prior to nanoindentation tests, both samples were mounted in the epoxy resin, then ground and electrochemically polished to eliminate surface damage. Nanoindentation tests were performed on different areas of sample A and B using Nanoindenter® XP system equipped with a spherical indenter of radius R=1.78 μm in the continuous stiffness mode (CSM)

with a constant strain rate $\dot{p}/p$ =0.05 s^{-1}. Test areas are shown in Fig. 1.1, denoted as Top, Mid and Bottom. Both Top and Bottom areas are placed 0.3 mm away to the edges. For the statistical analysis purpose, around 80 indents were conducted and placed far enough to avoid interference at each indent. The first pop-in loads of 80 indents were recorded to convert to maximum shear stresses, $\tau_{\max}$, so as to generate the cumulative probability curves.

3. Results and discussion

As shown in Fig. 1.1, no shear bands were observed in the test areas on sample A, indicating that the deformation is still in elastic regime. The estimated bending curvatures of inner and outer edges are 27.55 mm^{-1} and 28.27 mm^{-1}. Thus, the pre-stresses at Top and Bottom areas are estimated to be 1.57 GPa and -1.61 GPa, while Mid area on the neutral plane is stress-free. Compared to the yield stress of 1.65 GP [27], the pre-stresses are in the elastic stage, but very close to macroscopic yield. Considering that Sample B has the curvatures of 33.85 mm^{-1} and 30.39 mm^{-1}, the residual strain is estimated to be 2.8% of tension at Top area, 3.1% of compression at Bottom area, and again zero at Mid area.

Evident pop-ins on the indentation load-displacement curves were observed on almost all indents. The initial elastic load-displacement curve is interrupted by a sudden discontinuous excursion as a signal of the onset of plastic deformation where the load of first pop-in is termed as P_{pop-in}. The maximum shear stress $\tau_{\max}$ under the spherical nanoindentation can be calculated by [28]

$$\tau_{\max} = 0.445\left(\frac{16P_{pop-in}E_r^2}{9\pi^3R^2}\right)^{1/3}. \quad (1)$$

The reduced modulus E_r is determined by $E_r = \left[\left(1-\nu_s^2\right)/E_s + \left(1-\nu_i^2\right)/E_i\right]^{-1}$, where E_s =89GPa, ν_s =0.37, E_i =1141GPa and ν_i =0.07 are the Young's moduli and Poisson ratios of BMG sample and diamond indenter, respectively.

The cumulative probability curves as a function of $\tau_{\max}$ for sample A are plotted in Fig. 1.2. $\tau_{\max}$ at the stress-free Mid area varies in a narrow range from 2.9 GPa to 3.1 GPa. Since sample A was subjected to tensile pre-stresses at the Top area, $\tau_{\max}$ reduced dramatically to a mean value of 2.6 GPa, whereas the compressive pre-stresses at the Bottom area slightly increased $\tau_{\max}$ to a mean value of 3.2 GPa. Consistent with our previous works [25, 29] compressive stress showed less significant effect on the pop-in load than tensile stress. A straightforward mechanics analysis shows that $\tau_{\max}$ of both compressive and tensile sides needs to be corrected by the pre-stress or residual stress. After correction, the cumulative probability curves as a function of maximum effective shear stress, τ_{eff}, is shown in Fig. 1. 2(d). It is noted that the value τ_{eff} at all test areas are nearly identical, except for the different extended tails of the cumulative probability curves at the low stress levels, which arises from the distribution of local structural inhomogeneities prone to shear deformation.

Similarly, Fig. 1. 3 illustrates the cumulative probability curves for sample B. Note that the plastically bent sample B is the same as the one used in the previous work [26]. The Top and Bottom areas yielded during three-point bending in the stress states of tension

and compression. After unloading, an elastic bending stress field with negative bending moment would balance the loading moment. Therefore, the Top and Bottom areas reversely experienced compressive residual stress and tensile residual stress, respectively. The opposite stress states at similar locations of samples A and B explain the reverse trends regarding to the shift from $\tau_{\max}$ to τ_{eff} in Figs. 2 and 3. That is, $\tau_{\max}$ increased at Top area under the compressive residual stress while it decreased at Bottom area under the tensile residual stress. The cumulative probability curve for Mid area in Fig. 1.3(a) shows the narrowest distribution of $\tau_{\max}$ ranging from 2.6 GPa to 3.2 GPa, while the residual stresses broaden the distribution in Fig. 1.3(b) and 2.3(c). $\tau_{\max}$ was corrected by the residual stresses analyses in our previous work [25], and the cumulative probability was replotted as a function of τ_{eff} as presented in Fig. 1.3(d). Compared to the elastic deformation, plastic deformation resulted in a broader distribution on cumulative probability curves and larger tails at the low stress levels, which arises from the additional structural heterogeneities by the tiny shear bands as given in Fig. 1.1(b).

A stochastic model has been applied to correlate the structural heterogeneity to the cumulative pop-in probability for both conventional alloys and metallic glasses, thus giving a structure-property relationship [30, 31]. This model develops a unified expression of the thermally activated homogeneous nucleation process (near the theoretical strength) and the pre-existing defect-assisted heterogeneous process (at strengths lower than the theoretical value) for pop-ins. Particularly, the nucleation process is designated to shear band initiation in BMGs. For the homogeneous process, the shear bands will nucleate when the applied stress, τ, approaches the theoretical shear stress, τ_{th}. The nucleation rate is given by,

$\dot{n} = \dot{n}_0 \cdot \exp\left(-\frac{\varepsilon - \tau V^*}{k_B T} \right)$, where $\dot{n}_0$ is a pre-factor, V^* is the activation volume, T is the absolute temperature, ε is the intrinsic nucleation energy barrier, and k_B is the Boltzmann constant. The survivability for the homogeneous nucleation process, q_{homo}, is given by

$$q_{homo} = \exp\left(A_0 \int_{-\infty}^{\tau_{eff}^{pop-in}} \exp\left(\frac{\tau_{eff} V^*}{kT} \right) \frac{1}{\tau_{eff}} d\tau_{eff} \right) \quad (2)$$

where A_0 (dimensionless) and V^* are two fitting parameters. Thus, the cumulative probability for homogeneous shear band nucleation process is simply written as $f_{homo} = 1 - q_{homo}$. The heterogeneous shear band formation process is governed by the pre-existing defects, defined as the activated structural heterogeneities randomly distributed within a well-relaxed glass matrix, which is similar to 'liquid-like' zones [32]. It assumes that the first pop-in will occur if the applied stress is larger than the defect strength, τ_{def}, in a given stressed volume of V_{d}, within which a pre-existing defect can be found. For simplicity, the value of the defect strength, τ_{def}, is given by the flow stress of the bulk sample. The probability of not finding defects in V_{d} is given by a Poisson distribution,

$$q_{hetero} = \exp(-\rho_{defect} V_d). \quad (3)$$

The defect density ρ_{defect} and strength τ_{def} are fitting parameters The stressed volume V_{d} is determined by a dimensionless relationship, $V_d / a^3 = \hat{V}_d \left(\tau_{def} / \tau_{eff} \right)$, where a is the contact radius [33]. Hence, the cumulative probability for heterogeneous shear band formation process is determined by $f_{hetero} = 1 - q_{hetero} = 1 - \exp(-\rho_{defect} V_d)$. Considering that

the homogeneous and heterogeneous processes are two independent events, the total survivability will be $q_{total} = q_{hetero} \times q_{\mathrm{homo}}$. Consequently, the unified cumulative pop-in probability is given by $f_{total} = 1 - q_{total}$ and further simplified as

$$f_{total} = 1\text{-}\exp\left(-A_0 I\left(V^* \tau_{eff}^{pop-in} / k_B T\right) - \rho_{defect} V_d\right) \quad (4).$$

The exponential integral I is defined by $I(x) = \int_{-\infty}^{x} t^{-1} e^t dt$.

Solid lines in Figs. 2 and 3 represent the predicted results by the above unified model. The values of all fitting parameters are listed in Table 1. The thermally activated homogeneous nucleation process is supposed to be independent on the pre-stress and residual stress, when using the effective pop-in stress, τ_{eff}^{pop-in} . Because of the same experimental condition, the parameters A_0 and V^* are obtained from our previous work and the values only vary slightly [23, 31]. Another fitting parameter τ_{def} is related to bulk flow stress and clearly a function of the defect density. Thus, the major fitting parameter ρ_{defect} varies greatly, depending on the different pre-indentation state. Fitting results show ρ_{defect} with the lowest value at the Mid area in sample A, corresponding to the smallest tail in Fig. 2.2 (d), which suggests that these pop-ins are almost entirely governed by the homogeneous process. The pre-stress increases ρ_{defect} to $39.4\times10^{15}\mathrm{m}^{-3}$ and $54.7\times10^{15}\mathrm{m}^{-3}$ in the tension and compression sides suggesting that the sample has increased structural heterogeneity upon the elastic deformation. From the perspective of atomic level stress, the distribution of local stressed regions in amorphous metals varies significantly due to local structural defects on the nanometer scale. These local structural configurations can be

characterized by local shear modulus [34], which is 'soft', and become the potential regions for local plastic events [35]. It thus suggests that, instead of an overall homogeneous elastic deformation, local plastic deformation occurs inhomogeneously and generates additional heterogeneities, leading to increased ρ_{defect}. Plastically bent Sample B possesses a similar value of ρ_{defect} at the Mid area as it is a stress-free area as well. Residual stress increases ρ_{defect} to larger values of 211×10^{15}m^{-3} and 502×10^{15}m^{-3}, as compared to the elastically bent sample. Specifically, the increase of ρ_{defect} is more significantly influenced by tensile residual stress at the Bottom area. However, the area with residual tensile stress undergoes compressive stress during the plastic deformation, which would induce irreversible defects even via unloading process. It elucidates that the compressive plastic stress creates more structural heterogeneities. What's more, τ_{def} increases when fitting Sample B compared to Sample A, which means the plastically induced heterogeneities have higher strength than the elastically induced heterogeneities. This observation may be rationalized by the tiny and immature shear bands observed in the plastically bent samples. The defect spacing defined by $1/\sqrt[3]{\rho_{defect}}$ is summarized at each area in Fig. 1.4. The inset sketches illustrate the defect distribution under different cases. Both samples have the equivalent defect spacing at Mid areas, i.e., a pristine state mostly governed by the homogeneous nucleation process for pop-in. But the defect spacing of sample B reduced significantly by plastic deformation to 1.67 μm and 1.26 μm, while sample A show a little larger defect spacing of 2.94 μm and 2.63 μm. As a great number of tiny shear bands were observed on sample B, the spacing of the heterogeneous nucleation sources was dramatically reduced, giving rise to the higher

defect density and smaller defect spacing. Consequently, solid lines in Fig. 1.3 showed small tail for Middle case, but elevated tails for Top and Bottom cases.

Both the pre-stress and residual stress rejuvenates BMGs to a high defect density state, decreasing the spacing of activated heterogeneities. Moreover, many small shear bands are generated after plastic deformation in sample B. The density of material in the shear band differs from the surrounding matrix [36]. The higher degree of structural disorder in the shear band was also found in Ref. [37]. The above configurational variation would be the reason to form additional heterogeneities. For example, that would lower the stress required to initiate a shear band by the cooperative assembly of multiple STZs when the indenter encountered these structural heterogeneities. These many small shear bands can also redistribute the applied strain field, block each other, and restrain the propagation of a catastrophic shear band. Plasticity can thus be improved by pre-formed shear bands with highly rejuvenated atomic structure.

It should be noted that the size effect and strain rate effect on nanoindentation pop-in events have been extensively studied [38-40]. Our previous work [31] studied the effect of indenter radius on pop-in events, which showed the larger the indenter, the lower the pop-in stress and the higher the variation in the pop-in stress. Because the contact radius at pop-in increases with the increase of indenter radius, so that the increase of the stressed volume size increases the probability of sampling the pre-existing defects. The size of indenter used in the current study is 1.78 μm for all the indentation tests. Hence, our results exclude any changes caused by these size effects. The constant loading rate in the current study also eliminates the strain rate effect. It was reported that the homogeneous nucleation

of shear banding is rate-independent, while the heterogeneous process trigged by structural inhomogeneities is rate-dependent. In other words, the increased loading rate will trigger more structural heterogeneities to initiate the shear bands.

It would be interesting to evaluate the size of STZs by the activation volume V^* obtained in our stochastic model. It should be noted that if using Eq. (2) alone to fit the cumulative pop-in curves, the obtained activation volume V^* will be misleadingly high for those curves with long tails, whereas V^* should not vary noticeably for all these cases. Based on the cooperative shear model [41], the STZ volume can be estimated by

$$\Omega = \frac{\tau_{C0}/G_0}{6R'\gamma_C^2\xi\left(1-\tau_{C0}/\tau_{CT}\right)^{1/2}}V^* \tag{5}$$

where τ_{C0} and τ_{CT} are the threshold shear resistances at 0 K and T, G_0 is the shear modulus at 0 K, the constants $R' \approx 1/4$ and $\xi \approx 3$. The critical shear γ_C is obtained by a scaling law by averaging 30 different metallic glasses,

$$\gamma_C = \frac{\tau_{CT}}{G} = \gamma_{C0} - \gamma_{C1}\left(\frac{T}{T_g}\right)^{2/3} \tag{6}$$

in which $\gamma_{C0} = 0.036 \pm 0.002$, $\gamma_{C1} = 0.016 \pm 0.002$ and the glass transformation temperature of current BMG is 671 K. It is noted here that the shear modulus G has a weak temperature dependency. Following the equations (5) and (6), the STZ sizes were calculated by the determined V^* and summarized in Table 2. The number of atoms (N) in the STZ can be estimated by considering the metallic glasses consisting of dense-packing hard spheres with an average atomic radius, $R = \left(\sum_i^n A_i r_i^3\right)^{1/3}$ [42], where A_i and r_i are the

atomic fraction and the atomic radius of each element, respectively. The average atomic radius for current BMG is calculated to be 0.182 nm. The STZ volume Ω of as-cast material is about 2 nm^3, and it decreased by ~10% and ~5% after elastic and plastic deformation, respectively. The corresponding atom number varies from 72 to 81 in the STZ. Contradictorily, it was found that the tensile stress would increase Ω; however, they failed to take into accounts the change of density [21]. A higher defect density likely tends to activate more STZs prior to yielding. The relationship of defect density and STZ needs further studies. The question of whether the structural heterogeneities induced elastically and plastically possess different atomic configurations, such as disorder degree, density and elastic moduli, needs further study beyond the investigation of nanoindentation pop-in tests.

4. Summary

In summary, despite a vast number of studies on the structural heterogeneities, this work provides an indirect and quantitative study of the spacing of activated heterogeneities from pop-in measurements in both elastically and plastically bent Zr-base BMGs. Defect densities and spacing were explained by a stochastic model convoluting thermally activated process and heterogeneous nucleation process. The results indicate that structural heterogeneity increases from strain heterogeneity induced by elastic deformation when the applied stress approaches the yield limit. Plastic deformation induced structural heterogeneity is significantly enhanced by tiny shear bands, showing higher defect density and much smaller defect spacing compared to elastic deformation. These results and

previous work imply that as an effective method to enhance ductility, mechanical rejuvenation induces high structural inhomogeneities by accumulating extensive defects.

References

[1] C.A. Schuh, T.C. Hufnagel, U. Ramamurty, Acta Mater, 55 (2007) 4067-4109.

[2] J. Schroers, W.L. Johnson, Phys Rev Lett, 93 (2004).

[3] F. Spaepen, Acta Metall Mater, 25 (1977) 407-415.

[4] A.S. Argon, Acta Metall Mater, 27 (1979) 47-58.

[5] D. Srolovitz, T. Egami, V. Vitek, Phys Rev B, 24 (1981) 6936-6944.

[6] S.D. Feng, K.C. Chan, S.H. Chen, L. Zhao, R.P. Liu, Sci Rep-Uk, 7 (2017).

[7] J. Ding, Y.Q. Cheng, H. Sheng, M. Asta, R.O. Ritchie, E. Ma, Nat Commun, 7 (2016).

[8] X.F. Cao, M. Gao, L.Z. Zhao, W.H. Wang, H.Y. Bai, J Appl Phys, 119 (2016).

[9] S.D. Feng, L. Qi, S.P. Pan, N. Xu, S.L. Zhang, M.Z. Ma, X.Y. Zhang, G. Li, R.P. Liu, J Alloy Compd, 656 (2016) 518-523.

[10] F. Zhu, H.K. Nguyen, S.X. Song, D.P.B. Aji, A. Hirata, H. Wang, K. Nakajima, M.W. Chen, Nat Commun, 7 (2016).

[11] E. Ma, J. Ding, Mater Today, 19 (2016) 568-579.

[12] Y. Fan, T. Iwashita, T. Egami, Nat Commun, 5 (2014).

[13] Q. Wang, C.T. Liu, Y. Yang, Y.D. Dong, J. Lu, Phys Rev Lett, 106 (2011).

[14] B.A. Sun, Y.C. Hu, D.P. Wang, Z.G. Zhu, P. Wen, W.H. Wang, C.T. Liu, Y. Yang, Acta Mater, 121 (2016) 266-276.

[15] G.R. Garrett, M.D. Demetriou, M.E. Launey, W.L. Johnson, P Natl Acad Sci USA, 113 (2016) 10257-10262.

[16] P. Murali, U. Ramamurty, Acta Mater, 53 (2005) 1467-1478.

[17] U. Ramamurty, M.L. Lee, J. Basu, Y. Li, Scripta Mater, 47 (2002) 107-111.

[18] Y. Tong, T. Iwashita, W. Dmowski, H. Bei, Y. Yokoyama, T. Egami, Acta Mater, 86 (2015) 240-246.

[19] W. Dmowski, T. Iwashita, C.P. Chuang, J. Almer, T. Egami, Phys Rev Lett, 105 (2010).

[20] P. Denis, C.M. Meylan, C. Ebner, A.L. Greer, M. Zehetbauer, H.J. Fecht, Mat Sci Eng a-Struct, 684 (2017) 517-523.

[21] C. Wang, Q.P. Cao, X.D. Wang, D.X. Zhang, S.X. Qu, J.Z. Jiang, Scripta Mater, 122 (2016) 59-63.

[22] Y. Wu, H. Bei, Y.L. Wang, Z.P. Lu, E.P. George, Y.F. Gao, Int J Plasticity, 71 (2015) 136-145.

[23] W.D. Li, Y.F. Gao, H.B. Bei, Sci Rep-Uk, 5 (2015).

[24] Y.F. Gao, H.B. Bei, Prog Mater Sci, 82 (2016) 118-150.

[25] L. Wang, H. Bei, Y.F. Gao, Z.P. Lu, T.G. Nieh, Acta Mater, 59 (2011) 7627-7633.

[26] Y. Wu, A.D. Stoica, Y. Ren, D. Ma, Y.F. Gao, H. Bei, Intermetallics, 67 (2015) 132-137.

[27] C.T. Liu, L. Heatherly, D.S. Easton, C.A. Carmichael, J.H. Schneibel, C.H. Chen, J.L. Wright, M.H. Yoo, J.A. Horton, A. Inoue, Metall Mater Trans A, 29 (1998) 1811-1820.

[28] H. Bei, Z.P. Lu, S. Shim, G. Chen, E.P. George, Metall Mater Trans A, 41a (2010) 1735-1742.

[29] L. Wang, H. Bei, Y.F. Gao, Z.P. Lu, T.G. Nieh, Acta Mater, 59 (2011) 2858-2864.

[30] T.L. Li, H. Bei, J.R. Morris, E.P. George, Y.F. Gao, Mater Sci Tech-Lond, 28 (2012) 1055-1059.

[31] W.D. Li, H. Bei, Y. Tong, W. Dmowski, Y.F. Gao, Appl Phys Lett, 103 (2013).

[32] E. Ma, Nat Mater, 14 (2015) 547-552.

[33] J.R. Morris, H. Bei, G.M. Pharr, E.P. George, Phys Rev Lett, 106 (2011).

[34] E. Ma, Z. Zhang, Nat Mater, 10 (2011) 10-11.

[35] H. Wagner, D. Bedorf, S. Kuchemann, M. Schwabe, B. Zhang, W. Arnold, K. Samwer, Nat Mater, 10 (2011) 439-442.

[36] H. Rosner, M. Peterlechner, C. Kubel, V. Schmidt, G. Wilde, Ultramicroscopy, 142 (2014) 1-9.

[37] A.J. Cao, Y.Q. Cheng, E. Ma, Acta Mater, 57 (2009) 5146-5155.

[38] Y. Lu, B. Sun, L. Zhao, W. Wang, M. Pan, C. Liu, Y. Yang, Sci Rep, 6 (2016) 28523.

[39] S. Wang, Y. Ye, S. Shi, Y. Yang, J Appl Phys, 119 (2016) 245113.

[40] Y. Shi, M.L. Falk, Acta Mater, 55 (2007) 4317-4324.

[41] W.L. Johnson, K. Samwer, Phys Rev Lett, 95 (2005) 195501.

[42] D. Pan, A. Inoue, T. Sakurai, M.W. Chen, P Natl Acad Sci USA, 105 (2008) 14769-14772.

Appendix 1

Table 1.1 Fitting parameters for the cumulative probability curves in the unified model.

Samples	V^* **(nm^3)**	A_0 **($\times 10^{-22}$)**	τ_{def} **(GPa)**	ρ_{defect} **($\times 10^{15} m^{-3}$)**	$1/\sqrt[3]{\rho_{defect}}$ **(μm)**
A-TOP	0.065	2.23	1.14	39.4	2.94
A-MID	0.073	3.31	1.14	5.1	5.89
A-BOTTOM	0.067	1.57	1.14	54.7	2.63
B-TOP	0.070	5.18	1.63	211	1.67
B-MID	0.072	1.08	1.14	6.3	5.41
B-BOTTOM	0.069	6.38	1.63	502	1.26

Table 1.2 The activation volume and the calculated STZ volume and atomic number.

Samples	V^* **(nm^3)**	Ω **(nm^3)**	N
A-TOP	0.065	1.82	72
A-MID	0.073	2.04	81
A-BOTTOM	0.067	1.87	74
B-TOP	0.070	2.01	78
B-MID	0.072	2.02	80
B-BOTTOM	0.069	1.96	77

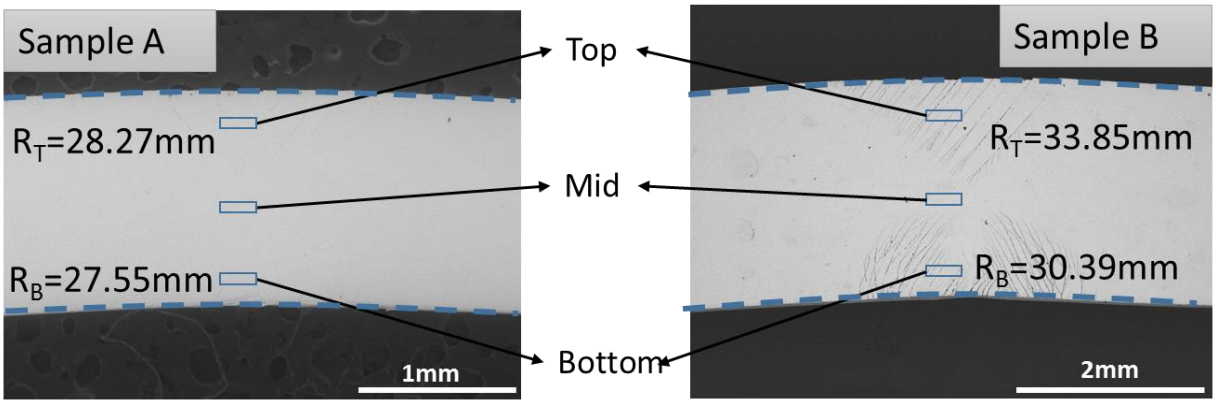

Fig. 1.1 SEM images show the surfaces of elastically bent Sample A and plastically bent Sample B, and the testing areas of nanoindentation. Prior to nanoindentation tests, both samples were electrochemically polished to eliminate surface damage. The curvatures and indentation test areas are also labeled.

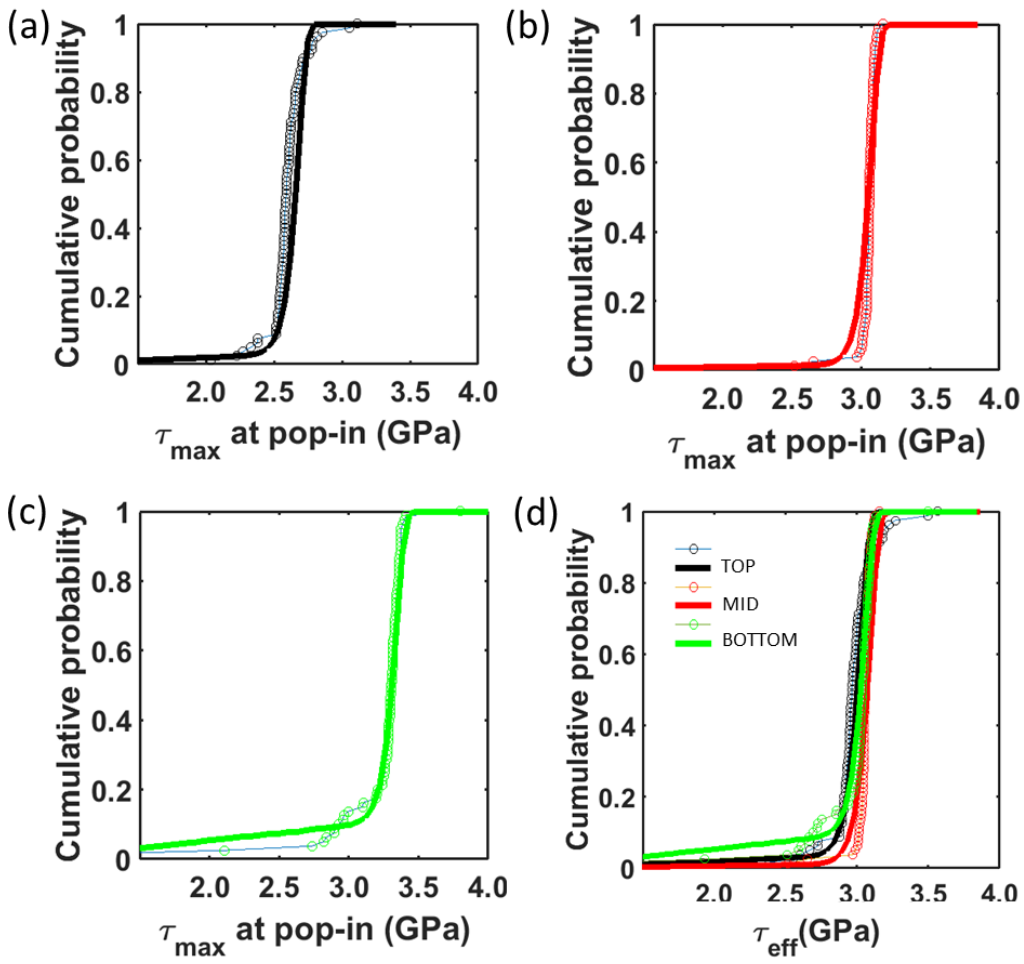

Fig. 1.2 The cumulative probability as a function of the maximum shear stress of Sample A at different areas, (a) Top, (b) Mid, (c) Bottom. (d) Cumulative probability as a function of the maximum effective shear stress of Sample A after correction by adding the elastic bending stress. Open cycles represent experimental data and solid line are the fitting curves using the unified model.

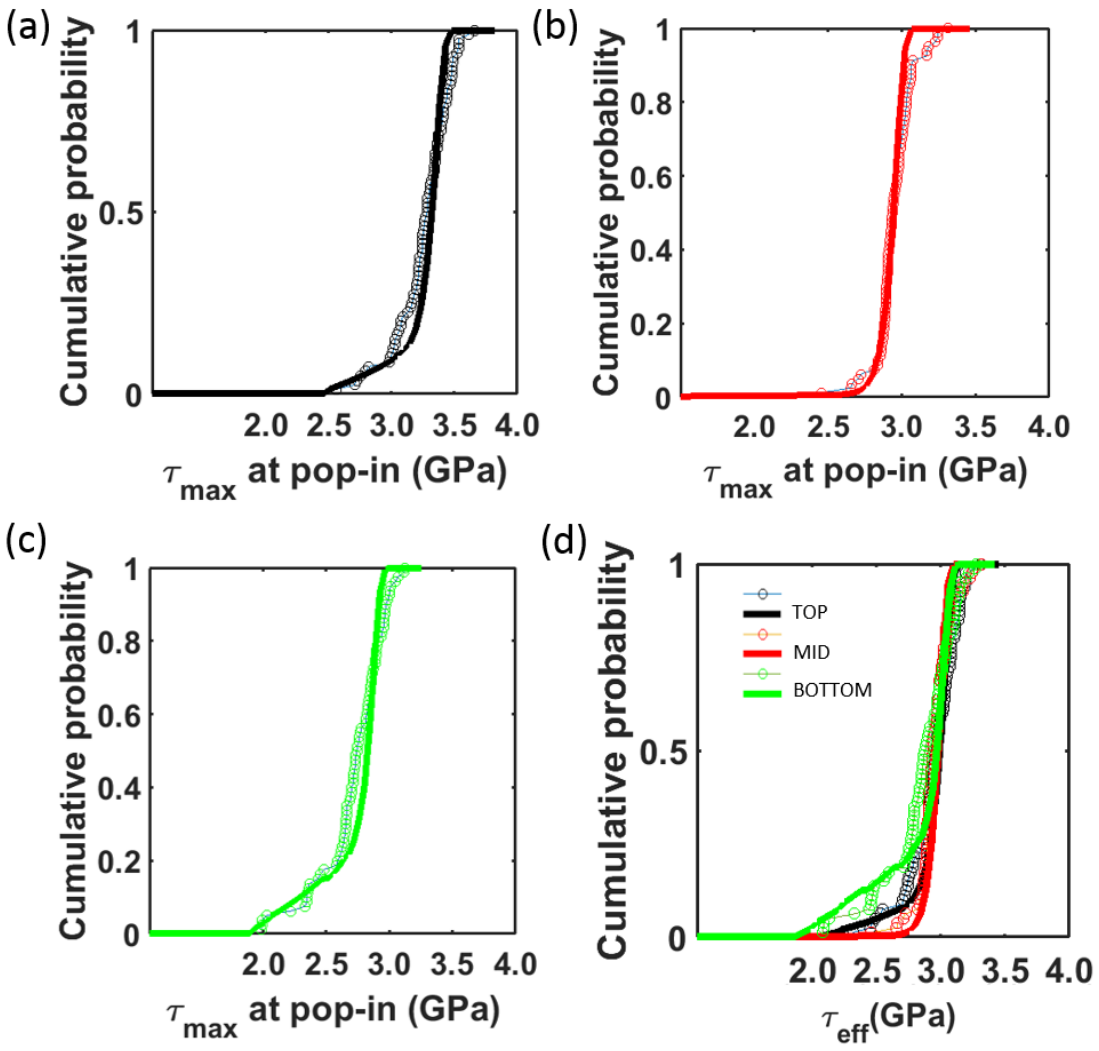

Fig. 1.3 The cumulative probability as a function of the maximum shear stress of Sample B at different areas, (a) Top, (b) Mid, (c) Bottom. (d) Cumulative probability as a function of the maximum effective shear stress of Sample B after correction by adding the residual stress. Open cycles represent experimental data and solid line are the fitting curves using the unified model.

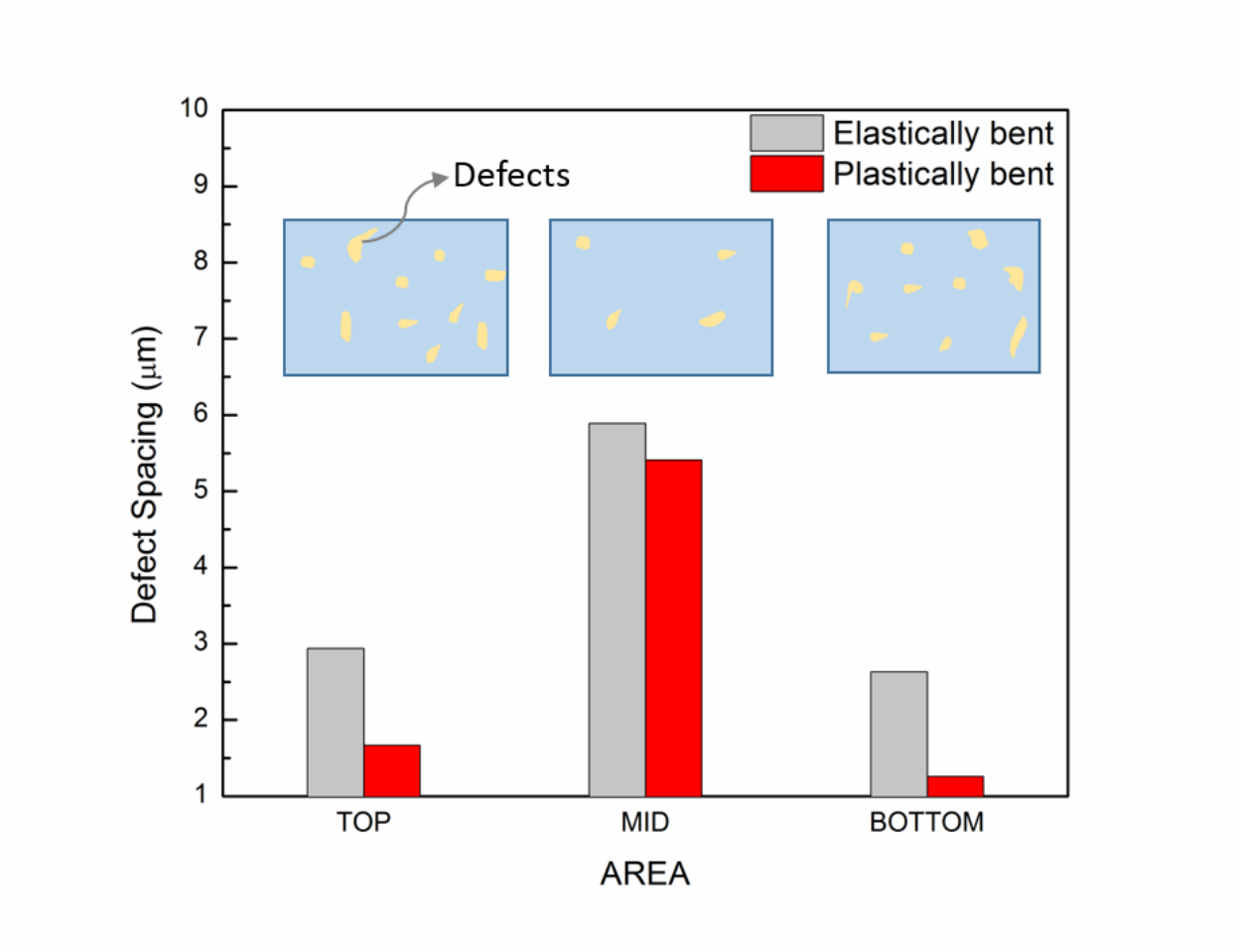

Fig. 1.4 Histogram of defect spacing in bent samples at different areas. The inset shows the schematic of distributions of structural heterogeneities in BMGs

CHAPTER II

EFFECT OF ION IRRADIATION ON STRUCTURAL AND MECHANICAL CHANGES IN A ZR-BASE METALLIC GLASS

This article in the same form will be submitted to Acta Materialia.

Authors:

Tingkun Liu, Miguel L. Crespillo

Department of Materials Science & Engineering, University of Tennessee, Knoxville, TN 37996, USA

Wei Guo, Ke Jin

Materials Science & Technology Division, Oak Ridge National Laboratory, Oak Ridge, TN 37831, USA

Yanwen Zhang, Hongbin Bei, Yanfei Gao

Department of Materials Science & Engineering, University of Tennessee, Knoxville, TN 37996, USA

Materials Science & Technology Division, Oak Ridge National Laboratory, Oak Ridge, TN 37831, USA

Abstract

Ion irradiation was applied to tailor the structural heterogeneities in Zr-base metallic glasses at room temperature. Experimental methods of X-ray diffraction, nanoindentation and micropillar compression were conducted to explore the irradiation effect on structural and mechanical changes in the studied material. The irradiated materials retained amorphous structure after room-temperature irradiation. The reduction of elastic modulus and hardness measured by nanoindentation indicated the ion irradiation induced mechanical softening. The transition of non-intersected shear bands to multiple intersected shear bands was observed on the irradiated micropillars after compression. The analysis of the displacement excursion of micropillar compression tests indicated a different deformation mode from the unirradiated state. A unified statistic model was proposed to quantitatively predict the density and strength of irradiation defects regardless of their specific structures. All the experimental and numerical findings suggested irradiation induced a different amorphous state from annealing and proves ion irradiation as an effective method to tune the structure and mechanical properties of metallic glasses.

1. Introduction

Metallic glasses (MGs) have gained significant interest due to their attractive properties since their discovery in 1960 [1]. Specifically, amorphous structures such as lacking the long-range order and absence of grain boundaries have produce their high strengths, high fracture toughness, good corrosion resistance and formability [2-7]. Despite these promising properties, the widespread application of MGs as structural materials is

challenged by their poor ductility at the temperature below glass transition temperature Tg [8-10]. A tendency towards catastrophic failure at room temperature is characterized by localized plastic shear bands, which has not been definitively linked to a specific well-defined structure, like dislocations in crystalline metals, or compositional features. However, such theories as free volume, shear transformation zone (STZ) and effective temperature Tf have been proposed to quantitatively predict deformation modes [8, 11, 12]. Generally, it is well accepted that the shear band trends to initiate at local structural heterogeneity which is described as high free volume zones, liquid-like zones [13] or soft spots [14], which can be defined as defects in MGs.

Such structural inhomogeneities or defects can be introduced by thermal processing and mechanical loading to improve ductility of MGs [15, 16]. The non-affine thermal strain has been reported to improve room-temperature plasticity because the pre-existing heterogeneities promote thermal cycling introducing more defects [17]. A mechanical relaxation-to-rejuvenation transition of Zr-base bulk metallic glass (BMG) was reported through elastostatic compression at ambient temperature due to stress-driven structural change of defects, such as loosely packed regions and densely packed regions [18]. The above observations conclude that the amorphous structure of MGs can be tailored by introducing structural defects, changing structural disordering state and free volume.

Alternatively, irradiation could be another approach to tailoring the amorphous structure in a similar way as thermal processing and mechanical loading, since the bombardment of MGs with energetic particles such as electron, neutron and ion induce structural defects [19-21]. Recently, in the experimental investigation of the mechanical

response of molded MG nanowires subjected to ion irradiation, a transition from originally brittle-like to ductile-like tensile behavior was found as a direct result of changes to the structural state of the glass [22]. The observed increase in ductility and reduction in yield strength were understood by changes in the fictive temperature caused by ion irradiation, and the mechanical softening was achieved as reduction in yield stress and hardness since the material was changed to a different structure state by ion irradiation [22]. The underling mechanism undergoes irradiation induced defects, which is similar to the thermally and mechanically induced structural heterogeneities assisting the formation of shear bands. Another study found that the structure can be changed by low-dosage irradiation increased the free volume, and by homogenizing the distribution of free volume, investigated by x-ray diffraction and transmission electron microscope, which is equivalent to the increase in the deformation temperature, thus resulting in the decrease in the yield strength [23]. On the contrary, irradiation induced hardening has also been observed in many MGs, among which the nano crystallization is responsible for the increase in hardness [24, 25]. Overall, few direct observations of irradiation-induced defects were reported experimentally; however, most were studied by molecular dynamics (MD) simulation. A resent MD research suggested that the plastic deformation mode of the MG nanopillars transits from localized shear banding to homogeneous shear flow due to irradiation-induced structural disordering [26]. A similar numerical study stated that ion-beam bombardment successively modifies the compositional and structural order toward a universal steady state and observed an increase in free volume and reduction of yield stress in irradiated MGs [27]. All these studies indicate that ion irradiation can be considered as a powerful

method to finely tune the structure and properties of MGs by carefully controlling particle energy, temperature and irradiation fluence.

As mentioned above, the macroscopic characteristics are related to the local structural changes due to irradiation caused by charged particles through nuclear and electronic interactions. The characterization and quantification of such structure variations has been a long-term challenge, especially for low-dose early stage ion irradiation damage, of which difficulties are mainly arisen from small defect size and the limited penetration depth. The subtle changes can be hardly detected by transmission electron diffraction constrained in tiny local region unless nano crystalline formed [22, 23] but it affects the mechanical properties significantly. Statistically analysis is essential to bridge the structure and properties in such situation. Additionally, high-energy X-ray diffraction (HEXRD) using intense synchrotron sources has been used to detect microscopic structural modifications in atomic scales, but it is ambitious to directly quantify or correlate to mechanical behaviors [28]. Overall, quantitative characterization of early stage irradiation defect is not sufficiently investigated, especially using direct experimental methods, remaining a vast filed of exploring the structure-property relationship. Therefore, a mechanically structure probing technique with high throughput is proposed to uncover the above scientific issues. As a nanoscale structure probing method, nanoindentation pop-in tests have been utilized to characterize structural heterogeneities quantitatively in MGs [29-31]. Pop-ins, or sudden displacement-bursts on load-displacement curve in a nanoindentation test, are typically attributed to triggering potent dislocation sources in the very small stressed volume in crystalline metals [32, 33], and they are corresponds to

structural heterogeneities associated with shear bands formation in MGs [34, 35]. It supposes that the irradiation particles change the amorphous structure inhomogeneously, thus performing statistical nanoindentation pop-in tests enables thorough evaluation of the atomistic structural features in irradiated MG samples.

In this study, a Zr-base MG is subjected to Ni+ ion irradiation to different dosages to study the structural and mechanical changes by the experimental methods of x-ray diffraction, nanoindentation and micropillar compression. A unified statistic model is proposed to predict the density and strength of irradiation induced defects in MGs. Irradiation caused mechanical softening is observed and the transition of amorphous state is controlled by irradiation induced defects. As a result, a new amorphous state is obtained by ion irradiation which is different from the annealed state. These observations prove ion irradiation as an effective method to tailoring the structure and property of MGs by introducing structural heterogeneities.

2. Experimental methods

Metallic glass with a nominal composition of $Zr_{52.5}Cu_{17.9}Ni_{14.6}Al_{10}Ti_5$ (BAM-11) was fabricated by arc-melting a mixture of pure base metal element in an argon atmosphere. The alloy was re-melted and formed the rod-like metallic glass with diameter of 7 mm by subsequent drop cast in a Zr-gettered helium atmosphere. The cast sample was annealed at 200 °C for 24 hours for further processing. Six samples were cut by electrical discharge machining (EDM) with the thickness of 1 mm. They were then ground and finally polished by colloidal silica suspension.

The ion irradiation experiments were conducted at the Ion Beam Materials Laboratory (IBML) at the University of Tennessee [36]. The annealed MG samples were irradiated at room temperature with 10 MeV Ni^{3+} ions at flux 1.04 $\times 10^{12}$ $cm^{-2}s^{-1}$ in the area of 6x6 mm^2. The displacement ion profiles of Ni irradiation were simulated using the Stopping and Range of Ions in Matter (SRIM-2013) as shown Fig. 2.1. Displacement per atom (dpa) is used to measure amount of radiation damage. The Kinchin-Pease Estimates, "quick calculation" modes were used under the condition of the threshold displacement energy as 40eV and the sample density as 6.7 g/cm^3 [37]. Based on the calculation result from SRIM, the irradiation fluences vary from 1.11×10^{13} to 1.11×10^{16} ions cm^{-2} to achieve the peak doses of 0.01, 0.05, 0.2, 1, and 10 dpa at the depth around 3 μm. The applied fluences and resultant doses are summarized in Table 2.1. The average dose beneath surface less than 1 μm is about 1/5 time of peak dose, where the nanoindentation was applied in the following.

Instrumented nanoindentation tests were performed at room temperature on annealed and irradiated samples using Nanoindenter® XP system equipped with a spherical indenter of radius R=1.78 μm. All the tests were carried out in the continuous stiffness mode (CSM) with a constant strain rate $\dot{P}/P$ 0.05 s^{-1} and holding at peak load for 10 seconds. The maximum load on sample is 4mN and the maximum depth is less than 1 μm. In total, 120 indents were conducted and placed far enough to avoid interference at each indent on each sample. The first pop-in load was recorded and further calculated t0 maximum shear stress. The nanoindentation modulus and hardness was estimated using a simple predictive model for spherical indentation [38].

The structure of annealed and irradiated samples was investigated by X-ray diffraction (XRD) using a PANalytical's X-ray diffractometer with Cu-Kα radiation. The XRD is used to identify the amorphous state of MGs after annealing and irradiations.

Micro pillars with initial diameter of ~ 2 μm with aspect ratio of >2 were fabricated using a dual beam focused ion beam (FIB) system (FEI Nova 200) operated at a constant accelerating voltage of 30kV. Using the top-down circular milling approach, the materials between two concentric circles can be retained. The selecting beam current was gradually decreased from 6.5 nA to 86 pA when decreasing the size of inner circle. A detailed description of top-down milling method can be found in previous works [39, 40]. The pillars were inside a 40 μm diameter crater, leaving enough space for 20 μm flat punch tip to avoid simultaneous contact with surrounding bulk and the pillar. The mechanical properties of the FIB-milled micropillars were measured in compression tests using a Nanoindenter® XP equipped with a flat punch diamond tip. The quality and dimensions of micropillars were examined using on a table scanning electron microscope (SEM) operated in the back-scattered electron (BSE) mode at an acceleration voltage of 15 kV. High resolution SEM was conducted to observe the morphology of shear bands after compression using a field emission gun (FEG) SEM JEOL 6500 at an acceleration voltage of 20 kV.

3. Results

The XRD patterns in Fig. 2.2 show that the annealed and irradiated samples are completely amorphous without visible Bragg's peaks. Even the highest dose of 10 dpa does not cause crystallization. The first diffuse peaks are fitted by pseudo-Voigt function and

the full width at half maximum (FWHM) is used to characterize the structure evolution plotted as a function of dosage in Fig. 2.3. The inserted figure is the illustration of fitting first diffuse peak of annealed sample, where the red line is fitted result, the black line is the experimental result and the arrow line indicates the FWHM. Evidently, the value of FWHM rapidly increases with increasing doses from 0 dpa to 1 dpa and slightly increases to 10 dpa. The evolution of FWHM suggests that amorphous state becomes more disordered after irradiation and it changes quickly at low dose level and then slowly increases with high dose. It can be deduced that the disorder will be saturated at higher dose and higher dose will probably produce disorder-to-order change.

Since the maximum depth of nanoindentation is less than 1 μm, the effective irradiation near surface is about 1/5 times as the peak dose. Thus, the nanoindentation results is discussed as a function of doses as 0 dpa, 0.002 dpa, 0.01 dpa, 0.04 dpa, 0.2 dpa, and 2 dpa. The representative load-displacement curves of nanoindentation at different irradiation doses are displayed in Fig. 2.4. The pop-in event is regarded as the sudden displacement excursion highlighted by the black circle on load-displacement curves, whereas the first pop-in represents the yield of sample, which is the initiation of plastic deformation and formation of first shear band. The pop-in events were observed in each nanoindentation test of the samples with the dose of 0 dpa, 0.002 dpa and 0.01 dpa. However, pop-in events were not observed in approximate half of 120 nanoindentation tests of the sample under irradiation dose of 0.04 dpa. Surprisingly, pop-ins vanished in all the nanoindentation tests for samples with doses of 0.2 dpa and 2 dpa. With the increase of irradiation doses, the pop-ins are more difficult to be detected because the irradiation

induced high-density defects assist the formation of shear band, so as the displacement burst is smaller than the instrument resolution. As a result, the pop-ins disappeared in the nanoindentation tests of highly irradiated samples. Even without direct microstructural evidence, one can presume that the deformation in such highly irradiated regions presents a different regime and is seemingly homogeneous, which is quite different from inhomogeneous shear banding.

The load of first pop-in is termed as P_{pop-in}, which is used to calculate the maximum shear stress $\tau_{\max}$ under the spherical nanoindentation by [41]

$$\tau_{\max} = 0.445\left(\frac{16P_{pop-in}E_r^2}{9\pi^3R^2}\right)^{1/3} \quad (1),$$

where E_r is the reduced modulus, and R=1.78 μm is the radius of a spherical indenter. The reduced modulus E_r is determined by $E_r = \left[\left(1-\nu_s^2\right)/E_s + \left(1-\nu_i^2\right)/E_i\right]^{-1}$, where E_s, ν_s, E_i and ν_i are the Young's moduli and Poisson ratios of samples and diamond indenter, respectively. The maximum shear stress $\tau_{\max}$ of first pop-in is statistically analyzed as shown in Fig. 2.5. The box displays the average, maximum, minimum and the standard deviation of $\tau_{\max}$ distribution. It is clearly seen that the annealed sample possesses the highest $\tau_{\max}$ average value about 3.26 GPa. The $\tau_{\max}$ average reduces to about 2.91 GPa with the increase of doses up to 0.04dpa. The annealed sample shows the largest distribution of $\tau_{\max}$, which indicates that plastic deformation of the unirradiated sample is the most inhomogeneous. The standard deviation of $\tau_{\max}$ in 0dpa sample reveals the

inhomogeneous deformation. After irradiation, the stresses required for the onset of plastic deformation decreased but the deformation becomes more homogeneous.

The hardness and modulus were estimated by a simple predictive model for spherical indentation[38]. The schematic illustration in Fig. 2.6 shows the relationship between the depth of loaded and unloaded indentations. The radius of the circle of contact is calculated from $a = \sqrt{2Rh_p - h_p^2}$, where h_p is the depth of penetration below the circle of contact. Meyer's hardness is defined as the mean pressure over the circle of contact. Hence, the hardness can be calculated from the load P and the radius of the contact circle a by $H = P/\pi a^2$. The modulus E can be determined directly from $E = 3P/4a\delta$, where δ is the depth of penetration. δ can be obtained from the depth below the original surface during both loading and unloading, which are termed as h_t and h_r, representatively. Assuming the elastic displacement is evenly divided above and below the circle of contact, the relationship of h_t, h_r, δ and h_p is given as $h_t = h_r + \delta = h_p + \delta/2$. The Fig. 2.6 displays the hardness and modulus as a function of irradiation doses. The hardness of 0 dpa sample is 5.9 GPa and the modulus is 116.9 GPa. The irradiation up to 0.01 dpa does not affect the hardness and modulus. The transition is found at the irradiation dose of 0.04 dpa. Further irradiation significantly reduces the hardness and modulus. At the peak dose level, the hardness decreases by 22% and the modulus decrease by 15%. Therefore, the high dose irradiation could induce mechanical softening in these samples, and the softening is significant above the dose of 0.04 dpa.

To further understand mechanism of irradiation induced softening by analyzing the pop-in tests, the cumulative probability of $\tau_{\max}$ is plotted and shown in Fig. 2.7 at different doses of 0 dpa, 0.001 dpa, 0.01 dpa and 0.4 dpa using dot plotting. Since only a few pop-ins are not observed on 0.04 dpa sample, cumulative probability is calculated by considering these pop-in stresses being infinitesimals to compare with the other samples. As shown in Fig. 2.7, the cumulative probability curves move leftward to low stress value. The slopes of cumulative probability curves of 0.002 dpa and 0.01 dpa samples are similar, but different from those of 0 dpa and 0.04 dpa sample. The curve profile of the unirradiated sample presents a larger tail at low stress level compared with 0.002 dpa and 0.01 dpa samples. The difference of the cumulative probability curves at varying doses derives from irradiation induced structural heterogeneities, which is investigated by a proposed model in the followings.

A stochastically statistic model is applied to quantitatively correlate the irradiation structural heterogeneities to the cumulative probability for both conventional alloys and metallic glasses, which declares a unified relation of the thermally activated homogeneous nucleation process and the pre-defect-assisted heterogeneous process. Specifically, the nucleation process is pointed out to be shear band localizing as a well-known deformation mechanism. Governed by homogeneous process, the shear bands nucleate until the applied stress τ exceeds the theoretical shear stress τ_{th}. The equation $\dot{n} = \dot{n}_0 \cdot \exp\left[\left(\tau v^* - \varepsilon\right)/kT\right]$ determines the nucleation rate, where $\dot{n}_0$ is a pre-factor, v^* is the activation volume, T is the absolute temperature, ε is the intrinsic nucleation energy barrier, and k is Boltzmann

constant. Homogeneous survivability q_{homo} that represents the probability of no homogeneous defect nucleation is given by

$$q_{homo} = \exp\left(A_0 \int_{-\infty}^{\tau_{eff}^{pop-in}} \exp\left(\frac{\tau_{eff} v^*}{kT} \right) \frac{1}{\tau_{eff}} d\tau_{eff} \right) \quad (2)$$

Where A_0 and v^* are fitting parameters. Thus, the cumulative probability for homogeneous shear band nucleation process is simply written as $f_{homo} = 1 - q_{homo}$. The heterogeneous shear band formation process is governed by pre-existing defects, i.e., the activated structural heterogeneities, in BMGs. It assumes that the first pop-in will occur if the applied stress is larger than the defect strength τ_{def} in a given volume V_{d}, within which a pre-existing defect is discovered. For simplicity, the value of defect strength τ_{def} is given by flow stress for initial prediction. The probability of no defects found in V_{d} distributes by Poisson function

$$q_{hetero} = \exp(-\rho_{defect} V_d). \quad (3)$$

The given volume V_{d} is determined by dimensionless analysis $V_d / \alpha^3 = \hat{V}_d \left(\tau_{def} / \tau_{\max} \right)$ [27]. The values of ρ_{defect} and τ_{def} are fitted and updated in the prediction. Hence, the cumulative probability for heterogeneous shear band formation process is determined by $f_{hetero} = 1 - q_{hetero} = 1 - \exp(-\rho_{defect} V_d)$. Considering homogeneous process and heterogeneous process as two independent events, the total survivability is $q_{total} = q_{hetero} \times q_{\mathrm{homo}}$. Consequently, the unified cumulative pop-in probability is given by $f_{total} = 1 - q_{total}$ and further simplified as

$$f_{total} = 1\text{-}\exp\left(-A_0 I\left(v^* \tau_{eff}^{pop-in} / kT\right) - \rho_{defect} V_d\right) \quad (4).$$

The exponential integral I is defined by $I(t)=\int_{-\infty}^{x} t^{-1} e^t dt$.

The fitting results by the above model is presented in Fig. 2.7 as solid lines, which reasonably predicts the experimental investigation, except for result of the sample irradiated to 0.04 dpa at the bottom of cumulative probability curve. The fitting parameters are given in Table 2. It is clearly seen that the irradiation increased the defect density. Specifically, the defect density is 2.2×10^{16} m^{-3} for the unirradiated sample. In this case, the pop-in event of this sample is governed by the thermally activated homogeneous nucleation and the pre-defect-assisted heterogeneous process at the same time. As a result, the cumulative probability curve shows an enhanced tail at lower stress level. However, the pop-in events are dominated by the defects after irradiation. The irradiation-induced defects are created with much higher strength than the intrinsic defects retained from thermal history. As more irradiation is applied, the defect density continues to increase, but the strength of irradiation induced defects reduced. Due to the extensive defects induced by irradiation, the defect spacing is decreased as illustrated in Table 2. Consequently, the pop-in evens are completely controlled by defect-assisted heterogeneous process since each indent encounters the irradiated induced defects in the stressed volume below the indenter.

Since most pop-ins of the 0.04 dpa sample and those irradiated to higher doses are not detectable due to the machine limitation, micropillars were fabricated to investigate the deformation mechanism thoroughly by compression tests. Representative micropillars before compression at each irradiation level are presented in Fig. 2.8. The micropillars were

carefully milled by FIB with the diameter in the range of 1.87~2.32 μm. The aspect ratio (height/diameter) is constrained within 2.62~3.67. The dimensional details of all the micropillars are given in Table 3.

The compressive engineering stress-strain curves are shown in Fig. 2.9 at the irradiation level of 0 dpa, 0.05 dpa, 0.2 dpa, 1 dpa and 1 dpa. The SEM images of each compressively deformed micropillars are presented simultaneously. The engineering stress σ and engineering strain ε were determined from the measured force on the micropillar F, and the displacement Δh of the micropillar by $\sigma = 4F/\pi d^2$ and $\varepsilon = \Delta h / h$, where d is the diameter of micropillar in position of 1/3 to the top and h is the height of the micropillar. As shown in Fig. 2.9, before the onset of displacement, the curves all exhibit predominantly elastic behavior on loading up to the transition of elastic to plastic deformation. Since the machine stiffness is not calibrated, the absolute value of elastic modulus is not discussed here. Shear band formation is the expected mode of deformation at high stresses, which gives rise a displacement excursion accordingly to the stress-strain curve. The largest displacement excursion is observed on the stress-strain curve of unirradiated sample in Fig. 2.9 (a), indicating the formation of a major shear band immediately leads to a catastrophic failure. Except for this sample, multiple small displacement excursions are detectable. However, micropillar compression tests on the sample irradiated to 0.2 dpa exhibits smooth stress-strain curves with hardly detectable displacement excursions, indicating a structural transition probably occurred at a certain irradiation level. After inspecting the geometry of shear bands in Fig. 2.11, it is found that multiple parallel shear bands formed in the same

direction in the samples irradiated below 0.2 dpa, whereas the shear band intersection is observed in the samples irradiated to higher dpa.

4. Discussion

It is well known in metallic crystalline that irradiation by a single atom displacement could induce Frenkel defects, or interstitial vacancy pairs based on the assumption of that every atom received an energy greater than a certain threshold displaces from its lattice site and remains a vacancy permanently [2, 42]. Such irradiation defect in MGs is often described as a pair of free volume defect and anti-free volume defect or interstitial-like and vacancy-like defects, resulting in density fluctuation [19, 43]. Crystallization is also observed in some MGs after irradiation, which usually results in mechanical hardening, such as the hardness is increased because the nanocrystalline blocks the formation of shear bands [44, 45]. In the current study, even the irradiation dose is applied up to 10 dpa, there is no crystal phase observed on XRD in Fig. 2.2. At the same time, the observed mechanical softening such as the decrease in hardness and modulus excludes the suspicions of nanocrystalline without high resolution transmission electron microscopy (TEM). Hence, it is proposed that a new amorphous state is induced by ion irradiation based upon the mechanical changes of nanoindentation pop-in tests and micropillar compressions.

Mechanical rejuvenation or softening can also be caused by thermal processing [15], plastic deformation [46], shear band [47] and residual stresses [48]. The hardness reduction of these research is less than 10%. Even the combination of shear band and residual stresses does not decrease the hardness more than 15% [48]. Compared with inhomogeneous

softening caused by the above approaches in the same materials and others, the irradiation in the current work provides higher decrease in hardness as much as 22%. It clearly turns out that the irradiation is a more effective method to rejuvenate MGs homogenously.

Fig. 2.11 schematically illustrates irradiation induced defects and the structural changes after irradiation. The intrinsic defects are directly retained from thermal history such as annealing. As a result from nanoindentation pop-in tests, the shear band formation at first pop-in is controlled by thermally activated nucleation and pre-existing defects assisted nucleation simultaneously, which is agreed with previous work [31, 49]. The micropillars behave brittle-like deformation as the formation of a main shear band causes immediate failure. After ion bombardment, irradiation induced defects are newly formed, which is assumed to distinguish from the intrinsic defect because the defect strength is larger according to the fitting results from the proposed unified model of cumulative probability as shown in Fig. 2.7. Because of the large defect density and corresponding small defect spacing, the heterogeneous nucleation of first pop-in is easily triggered by irradiation defect. Agreed with the results in Fig. 2.7, the shear band formation is dominated by irradiation-induced defects in the sample irradiated to low dose. These high-density defects promote the shear band formation and the intersection of multiple shear bands performs ductile-like deformation. As the irradiation dose increasing, more defects are generated. As a result, the first pop-in cannot be detected due to the machine limitation. The vanish of pop-in events was also found in a Ti base MG after ion irradiation [50]. Eventually, a different amorphous state without crystallization is obtained in irradiated samples after high level irradiation.

A new glassy state can be also verified from mechanical softening i.e. the decrease in elastic modulus and hardness. The elastic modulus of a material is determined by the atomic bonds depending upon interatomic distance. Therefore, the change in elastic modulus by irradiation is in fact the change in interatomic distance. Due to the irradiation induced defects with high free volume, the high-density defects eventually increase free volume in the material, thus increase the atomic distance. In turns, the elastic modulus decreases with the increasing irradiation free volume. The change of interatomic distance could be further investigated by pair distribution function using synchrotron x-ray [51, 52]. Meanwhile, the reduction of hardness is attributed to irradiation defects. In micropillar compression tests, the shear band trends to initiate in soft sites which are irradiation induced defects. Thus, high-density irradiation defects facilitate multiple shear band formation and their intersection in the sample irradiated to high dose as seen in SEM images of Fig 10. Poor ductility due to lacking microstructure as hindering propagation of shear bands, leads a dominant shear band becoming a shear crack rather readily, such as the shear band formed in unirradiated sample and low-dose irradiated sample in Fig. 2.10. Increasing the possibility of the intersections among shear bands is regarded to be an alternative way to enhance ductility [53]. Thus, the observations of mechanical softening by nanoindentation and shear band intersection after micropillar compression not only indicate irradiation induced increasing in defect density as well as free volume but also increasing in plasticity. Similar structural transition was interpreted by the research of deformation mode in the metallic glass nanowires using in-situ mechanical testing in a scanning electron microscope [22], where the deformation was characterized as shear band

mediated in the as-molded sample and characterized as ductile at high ion fluences. An intermediate regime was observed between the shear band and ductile regimes as the fracture surface was not clearly a shear band or ductile mode, which indicated the transition between the deformation modes.

The displacement excursion is an important indicator of deformation mode of shear banding associated with elastic energy release. Generally, a shear band can only propagate an incremental distance if the strain energy relief associated with the propagation is larger than the energy increment of the shear band [54]. In a simplest analysis, the shear band propagates along the micropillar of an angle of 45˚ relieving applied stress or strain. The elastic strain energy is decreased by an amount $F * \Delta x$ and the shear band energy is increased by an amount $\sqrt{2}\pi d^2 / 4\Gamma$, where Γ is the energy per unit area of shear band. A value for Γ can be estimated by disordering of the structure [54]. Although larger plastic strains do not result in further disordering of the structure, irradiation induced defects will increase the disordering, which can be seen from the FWHM in Fig. 2.3 largely increased at the dose higher than 1 dpa. Since each displacement excursion Δx corresponds to energy release by shear banding, analyzing the magnitude of excursion displacements is beneficial to understanding irradiation effect on deformation behaviors. All the visible displacement excursions are summarized as histograms in Fig. 2.12 and schematically fitted by Gauss function and Exponential function. Even though the data is not sufficient to perfectly fit by the Gauss function and Exponential function, the profiles could indeed show differentiated distributions indicated by those to function. As seen from Fig. 2.10, the excursion displacements were approximately described by a Gauss function in unirradiated sample

with the peak displacement near 25~50 nm. After irradiation, the distribution of excursion displacements is changed. In the sample irradiated to 0.05 dpa, the histogram is illustrated by an Exponential function fitting where the most excursion displacements concentrate in small magnitude. As the irradiation is increased to 1 dpa, the histogram consists of a combination of Gauss like distribution and Exponential like distribution, suggesting the irradiation induced structural transition. When the sample is irradiated to 10 dpa, the excursion displacement distribution follows Gauss distribution again, but with different peak position and width from unirradiated sample, indicating a new glassy state is induced by irradiation.

5. Conclusion

In the current study, we investigated the ion irradiation effect on structural and mechanical changes in Zr-base MGs under different irradiation doses. Mechanical softening and a transition to new amorphous state were observed. The irradiation induced defect was quantitatively predicted by a statistic model unifying the thermal activated homogeneous nucleation of shear band and defect assisted heterogeneous nucleation of shear band. The results and conclusions of the study are shown as follows:

(1) The XRD patterns indicate that no crystallization occurred after ion irradiation, while the structural discording was increased by irradiation as an evidence of increasing in FWHM.

(2) The reduction in modulus and hardness was observed after ion irradiation in nanoindentations tests estimated by a simple model of spherical indenter and the reduction was not significant until the irradiation dose exceeded 0.04 dpa.

(3) In the nanoindentation pop-in tests, the pop-in events vanished in the samples irradiated to high doses. The cumulative probability curves of τ_{max} for the first pop-in indicated that the irradiated samples deformed more homogeneously than the unirradiated sample. By analyzing the cumulative probability curves by a unified statistic model, we proposed that the deformation of unirradiated sample was governed by thermal activated homogeneous nucleation and pre-existing intrinsic detects simultaneously whereas the deformation of irradiated samples was completely dominated by increasing irradiation defects. Different from intrinsic defects in the annealed state, these irradiation-induced defects exhibited the tendency of reduction in strength as increasing irradiation doses.

(4) The shear band patters after micropillar compression showed a transition of deformation modes from parallel non-intersected shear bands to multiple intersected shear bands as increasing the irradiation doses. The analysis of displacement excursion in micropillar compression clearly presented the transition of structure state to a new amorphous state.

References

[1] W.K. Jun, R. Willens, P. Duwez, Non-crystalline structure in solidified gold–silicon alloys, Nature 187(4740) (1960) 869.

[2] J.A. Brinkman, On the nature of radiation damage in metals, Journal of Applied Physics 25(8) (1954) 961-970.

[3] M. Ashby, A. Greer, Metallic glasses as structural materials, Scripta Materialia 54(3) (2006) 321-326.

[4] C.A. Schuh, T.C. Hufnagel, U. Ramamurty, Mechanical behavior of amorphous alloys, Acta Materialia 55(12) (2007) 4067-4109.

[5] G. Kumar, H.X. Tang, J. Schroers, Nanomoulding with amorphous metals, Nature 457(7231) (2009) 868.

[6] A. Inoue, A. Takeuchi, Recent development and application products of bulk glassy alloys, Acta Materialia 59(6) (2011) 2243-2267.

[7] M.D. Demetriou, M.E. Launey, G. Garrett, J.P. Schramm, D.C. Hofmann, W.L. Johnson, R.O. Ritchie, A damage-tolerant glass, Nature materials 10(2) (2011) 123.

[8] F. Spaepen, A microscopic mechanism for steady state inhomogeneous flow in metallic glasses, HARVARD UNIV CAMBRIDGE MASS DIV OF ENGINEERING AND APPLIED PHYSICS, 1976.

[9] J. Schroers, W.L. Johnson, Ductile bulk metallic glass, Physical Review Letters 93(25) (2004) 255506.

[10] J. Das, M.B. Tang, K.B. Kim, R. Theissmann, F. Baier, W.H. Wang, J. Eckert, "Work-hardenable" ductile bulk metallic glass, Physical Review Letters 94(20) (2005) 205501.

[11] A. Argon, Plastic deformation in metallic glasses, Acta metallurgica 27(1) (1979) 47-58.

[12] J. Langer, Dynamics of shear-transformation zones in amorphous plasticity: Formulation in terms of an effective disorder temperature, Physical Review E 70(4) (2004) 041502.

[13] E. Ma, Tuning order in disorder, Nature materials 14(6) (2015) 547-552.

[14] N. Wang, J. Ding, F. Yan, M. Asta, R.O. Ritchie, L. Li, Spatial correlation of elastic heterogeneity tunes the deformation behavior of metallic glasses, npj Computational Materials 4(1) (2018) 19.

[15] J. Saida, R. Yamada, M. Wakeda, S. Ogata, Thermal rejuvenation in metallic glasses, Science and Technology of advanced MaTerialS 18(1) (2017) 152-162.

[16] Y. Tong, W. Dmowski, H. Bei, Y. Yokoyama, T. Egami, Mechanical rejuvenation in bulk metallic glass induced by thermo-mechanical creep, Acta Materialia 148 (2018) 384-390.

[17] S. Ketov, Y. Sun, S. Nachum, Z. Lu, A. Checchi, A. Beraldin, H. Bai, W. Wang, D. Louzguine-Luzgin, M.A. Carpenter, Rejuvenation of metallic glasses by non-affine thermal strain, Nature 524(7564) (2015) 200.

[18] M. Zhang, Y. Wang, F. Li, S. Jiang, M. Li, L. Liu, Mechanical relaxation-to-rejuvenation transition in a Zr-based bulk metallic glass, Scientific Reports 7(1) (2017) 625.

[19] T. Nagase, T. Sanda, A. Nino, W. Qin, H. Yasuda, H. Mori, Y. Umakoshi, J.A. Szpunar, MeV electron irradiation induced crystallization in metallic glasses: Atomic structure, crystallization mechanism and stability of an amorphous phase under the irradiation, Journal of Non-Crystalline Solids 358(3) (2012) 502-518.

[20] R. Gerling, F.-P. Schimansky, R. Wagner, Restoration of the ductility of thermally embrittled amorphous alloys under neutron-irradiation, Acta Metallurgica 35(5) (1987) 1001-1006.

[21] A.G. Perez-Bergquist, H. Bei, K.J. Leonard, Y. Zhang, S.J. Zinkle, Effects of ion irradiation on Zr52. 5Cu17. 9Ni14. 6Al10Ti5 (BAM-11) bulk metallic glass, Intermetallics 53 (2014) 62-66.

[22] D. Magagnosc, G. Kumar, J. Schroers, P. Felfer, J. Cairney, D. Gianola, Effect of ion irradiation on tensile ductility, strength and fictive temperature in metallic glass nanowires, Acta Materialia 74 (2014) 165-182.

[23] X.L. Bian, G. Wang, H.C. Chen, L. Yan, J.G. Wang, Q. Wang, P.F. Hu, J.L. Ren, K.C. Chan, N. Zheng, A. Teresiak, Y.L. Gao, Q.J. Zhai, J. Eckert, J. Beadsworth, K.A. Dahmen, P.K. Liaw, Manipulation of free volumes in a metallic glass through Xe-ion irradiation, Acta Materialia 106 (2016) 66-77.

[24] Y. Huang, H. Fan, X. Zhou, P. Xue, Z. Ning, D. Daisenberger, J. Sun, J. Shen, Structure and mechanical property modification of a Ti-based metallic glass by ion irradiation, Scripta Materialia 103 (2015) 41-44.
[25] E. Menéndez, A. Hynowska, J. Fornell, S. Suriñach, J. Montserrat, K. Temst, A. Vantomme, M. Baró, E. García-Lecina, E. Pellicer, Influence of the irradiation temperature on the surface structure and physical/chemical properties of Ar ion-irradiated bulk metallic glasses, Journal of Alloys and Compounds 610 (2014) 118-125.
[26] Q. Xiao, L. Huang, Y. Shi, Suppression of shear banding in amorphous ZrCuAl nanopillars by irradiation, Journal of Applied Physics 113(8) (2013) 083514.
[27] S. Mayr, Impact of ion irradiation on the thermal, structural, and mechanical properties of metallic glasses, Physical Review B 71(14) (2005) 144109.
[28] S. Michalik, J. Michalikova, M. Pavlovic, P. Sovak, H.P. Liermann, M. Miglierini, Structural modifications of swift-ion-bombarded metallic glasses studied by high-energy X-ray synchrotron radiation, Acta Materialia 80 (2014) 309-316.
[29] T.K. Liu, Y.F. Gao, H.B. Bei, Probing elastically or plastically induced structural heterogeneities in bulk metallic glasses by nanoindentation pop-in tests, Aip Adv 7(8) (2017).
[30] W.D. Li, Y.F. Gao, H.B. Bei, On the correlation between microscopic structural heterogeneity and embrittlement behavior in metallic glasses, Scientific reports 5 (2015).
[31] W. Li, Y. Gao, H. Bei, On the correlation between microscopic structural heterogeneity and embrittlement behavior in metallic glasses, Scientific reports 5 (2015) 14786.

[32] S. Pathak, J.L. Riesterer, S.R. Kalidindi, J. Michler, Understanding pop-ins in spherical nanoindentation, Appl Phys Lett 105(16) (2014).

[33] J.R. Morris, H. Bei, G.M. Pharr, E.P. George, Size Effects and Stochastic Behavior of Nanoindentation Pop In, Physical Review Letters 106(16) (2011).

[34] C. Deng, C.A. Schuh, Atomistic mechanisms of cyclic hardening in metallic glass, Applied Physics Letters 100(25) (2012) 251909.

[35] C.E. Packard, L.M. Witmer, C.A. Schuh, Hardening of a metallic glass during cyclic loading in the elastic range, Applied Physics Letters 92(17) (2008) 171911.

[36] Y. Zhang, M.L. Crespillo, H. Xue, K. Jin, C.H. Chen, C.L. Fontana, J.T. Graham, W.J. Weber, New ion beam materials laboratory for materials modification and irradiation effects research, Nucl Instrum Meth B 338 (2014) 19-30.

[37] H. Wiedersich, Effects of the Primary Recoil Spectrum on Microstructural Evolution, J Nucl Mater 179 (1991) 70-75.

[38] J.S. Field, M.V. Swain, A Simple Predictive Model for Spherical Indentation, J Mater Res 8(2) (1993) 297-306.

[39] S. Shim, H. Bei, M.K. Miller, G.M. Pharr, E.P. George, Effects of focused ion beam milling on the compressive behavior of directionally solidified micropillars and the nanoindentation response of an electropolished surface, Acta Materialia 57(2) (2009) 503-510.

[40] W. Guo, E. Jagle, J.H. Yao, V. Maier, S. Korte-Kerzel, J.M. Schneider, D. Raabe, Intrinsic and extrinsic size effects in the deformation of amorphous CuZr/nanocrystalline Cu nanolaminates, Acta Materialia 80 (2014) 94-106.

[41] H. Bei, Z.P. Lu, S. Shim, G. Chen, E.P. George, Specimen Size Effects on Zr-Based Bulk Metallic Glasses Investigated by Uniaxial Compression and Spherical Nanoindentation, Metall Mater Trans A 41a(7) (2010) 1735-1742.

[42] M.W. Thompson, Defects and radiation damage in metals, Defects and Radiation Damage in Metals, by MW Thompson, Cambridge, UK: Cambridge University Press, 1974 (1974).

[43] T. Egami, K. Maeda, V. Vitek, Structural defects in amorphous solids A computer simulation study, Philosophical Magazine A 41(6) (1980) 883-901.

[44] W. Luo, B. Yang, G. Chen, Effect of Ar+ ion irradiation on the microstructure and properties of Zr–Cu–Fe–Al bulk metallic glass, Scripta Materialia 64(7) (2011) 625-628.

[45] Y. Huang, B. Zhou, H. Fan, Y. Wang, D. Wang, J. Sun, J. Shen, Effect of ion irradiation in an Al90Fe2Ce8 metallic glass, Materials & Design (1980-2015) 62 (2014) 133-136.

[46] S. Xie, E.P. George, Hardness and shear band evolution in bulk metallic glasses after plastic deformation and annealing, Acta Materialia 56(18) (2008) 5202-5213.

[47] H. Bei, S. Xie, E.P. George, Softening caused by profuse shear banding in a bulk metallic glass, Physical Review Letters 96(10) (2006).

[48] L. Wang, H. Bei, Y.F. Gao, Z.P. Lu, T.G. Nieh, Effect of residual stresses on the hardness of bulk metallic glasses, Acta Materialia 59(7) (2011) 2858-2864.

[49] T. Liu, Y. Gao, H. Bei, Probing elastically or plastically induced structural heterogeneities in bulk metallic glasses by nanoindentation pop-in tests, AIP Advances 7(8) (2017) 085216.

[50] A. Zare, Q. Su, J. Gigax, S. Shojaee, M. Nastasi, L. Shao, D. Lucca, Effects of ion irradiation on structural and mechanical properties of crystalline Fe/amorphous SiOC nanolaminates, Acta Materialia 140 (2017) 10-19.

[51] Y. Tong, T. Iwashita, W. Dmowski, H. Bei, Y. Yokoyama, T. Egami, Structural rejuvenation in bulk metallic glasses, Acta Materialia 86 (2015) 240-246.

[52] W. Dmowski, Y. Yokoyama, A. Chuang, Y. Ren, M. Umemoto, K. Tsuchiya, A. Inoue, T. Egami, Structural rejuvenation in a bulk metallic glass induced by severe plastic deformation, Acta Materialia 58(2) (2010) 429-438.

[53] R. Raghavan, K. Boopathy, R. Ghisleni, M.A. Pouchon, U. Ramamurty, J. Michler, Ion irradiation enhances the mechanical performance of metallic glasses, Scripta Materialia 62(7) (2010) 462-465.

[54] C. Volkert, A. Donohue, F. Spaepen, Effect of sample size on deformation in amorphous metals, Journal of applied physics 103(8) (2008) 083539.

Appendix 2

Table 2.1Applied flounce and doses calculated by damage profile of Ni ion irradiation in Fig. 2.1

# Sample	Fluence (cm^{-2})	Peak dose (dpa)	Dose near surface (dpa)
1(annealed)	0	0	0
2	1.11×10^{13}	0.01	0.002
3	5.56×10^{13}	0.05	0.01
4	2.22×10^{14}	0.2	0.04
5	1.11×10^{15}	1	0.2
6	1.11×10^{16}	10	2

Table 2.2 Fitting parameters of the unified structural model corresponding to the plots in Fig. 2.7. The defect spacing is calculated by $1/\sqrt[3]{\rho_{defect}}$

Samples	**V*(nm^3)**	**A_0 ($\times 10^{-22}$)**	**τ_{def} (GPa)**	**ρ_{def} (m^{-3})**	**Defect spacing (um)**
0 dpa	0.0685	5.96	1.14	2.2e16	3.57
0.002 dpa	0.0726	3.32	2.58	5e17	1.26
0.01 dpa	0.0707	4.40	2.51	1e18	1.00
0.04 dpa	0.0758	4.38	1.56	5e18	0.585

Table 2.3 Dimension of the FIB milled micropillars at different irradiation doses. The micropillars were carefully milled with the diameter in the range of 1.87~2.32 μm and the aspect ratio (height/diameter) constrained within 2.62~3.67.

Peak Dose	Pillar #.	Diameter(mm)	Height(mm)	Aspect ratio
0dpa	p1	2.29	6.70	2.93
	p2	2.31	6.38	2.76
	p3	2.07	7.20	3.48
0.05dpa	p1	2.15	6.64	3.09
	p2	2.27	6.94	3.23
	p3	1.98	6.69	3.38
0.2dpa	p1	1.87	5.73	3.07
	p2	2.02	5.97	2.96
	p3	2.17	5.17	2.38
1dpa	p1	2.35	5.84	2.49
	p2	2.42	6.72	2.78
	p3	1.99	5.37	2.69
10dpa	p1	2.17	5.69	2.62
	p2	2.18	6.16	2.83
	p3	2.00	7.33	3.67

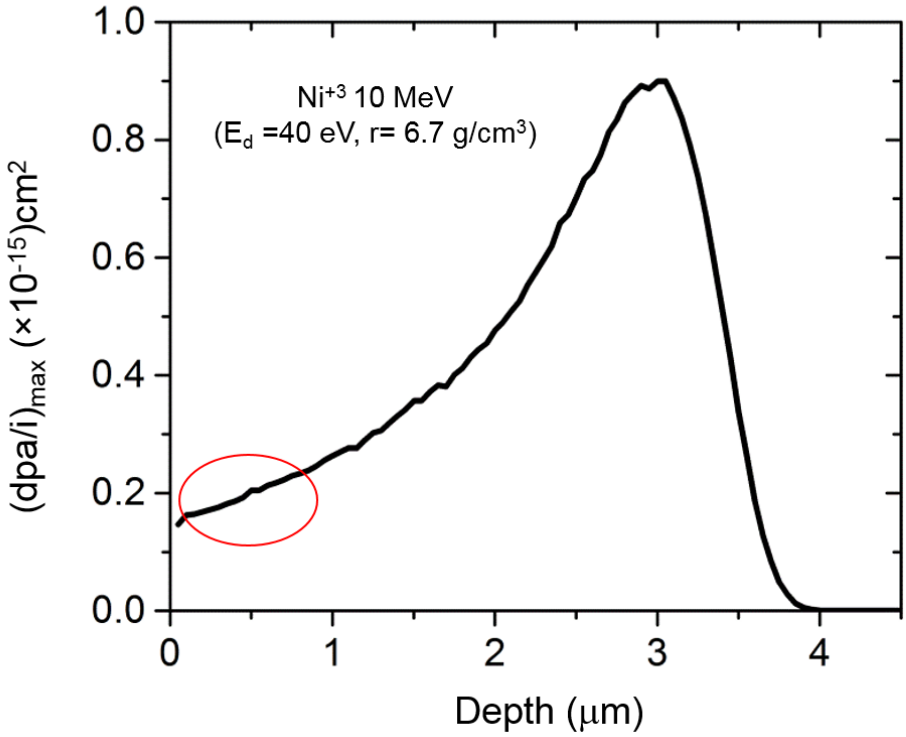

Fig. 2.1 Damage and ion profile calculated by SRIM after 10 MeV Ni ion irradiation at the influence of 10^{15} cm^{-2} under the condition of the threshold displacement energy as 40eV and the sample density as 6.7 g/cm^3, the red circle indicating the depth region for nanoindentation pop-in tests where the dpa is 5 time less than the peak value

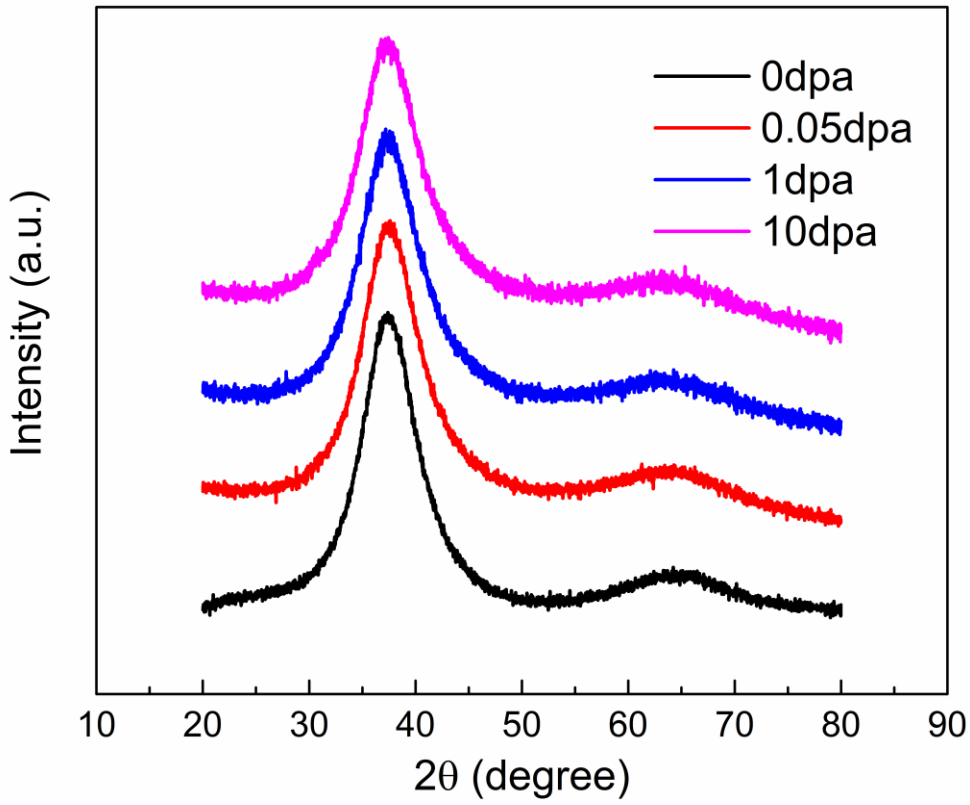

Fig. 2.2 XRD patterns of annealed and irradiated samples under different dosages show the first and second diffuse peaks without sharp Brag diffraction peaks, verifying the amorphous features of the samples and no crystallization occurred after irradiation.

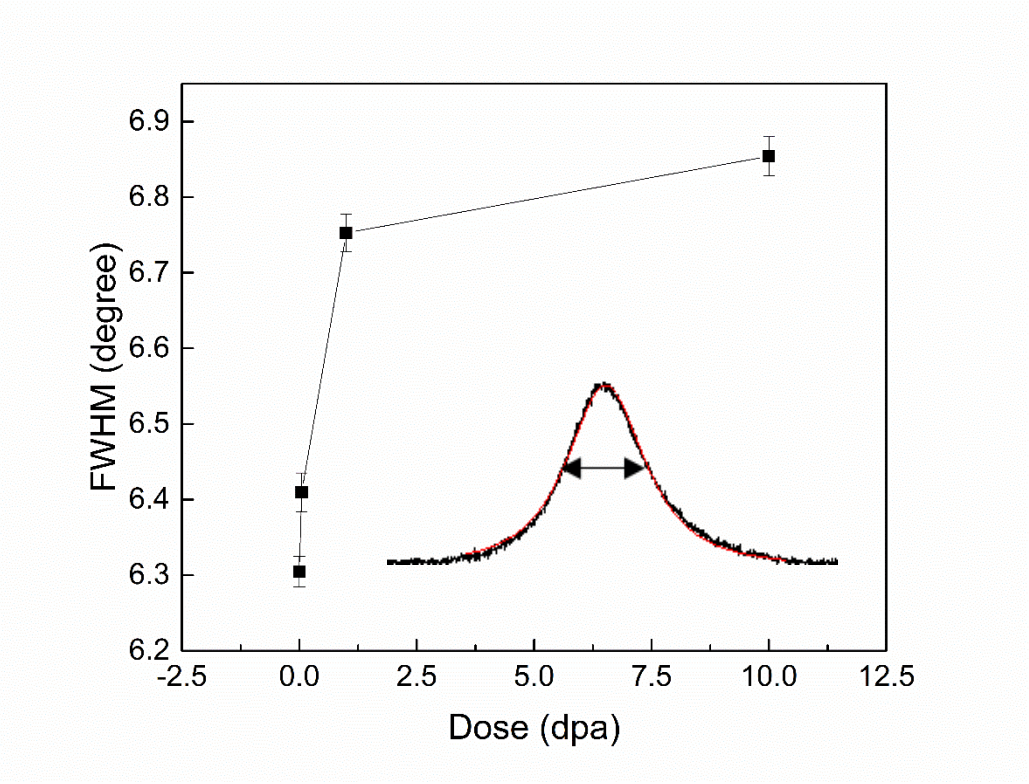

Fig. 2.3 Full width at half maximum (FWHM) of annealed and irradiated samples as a function of irradiation doses. The inset is the illustration of peak fitting by pseudo-Voigt function and FWHM of the first diffused peak.

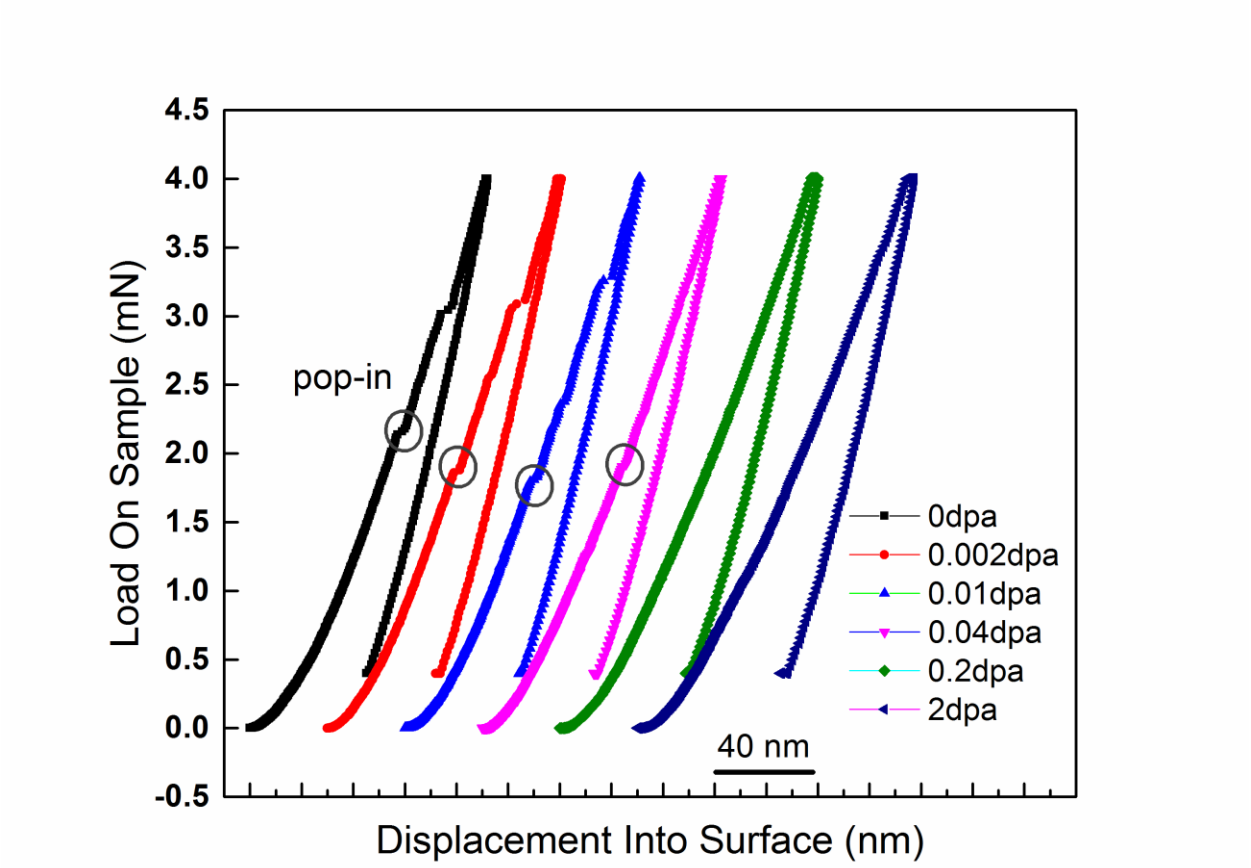

Fig. 2.4 Representative displacement-load curves of nanoindentation pop-in tests at different irradiation dosages. The black circles indicate the first pop-ins and they are disappeared at the dosages of 0.2 dpa and 2 dpa due to high density defects and limitation of instrument resolution.

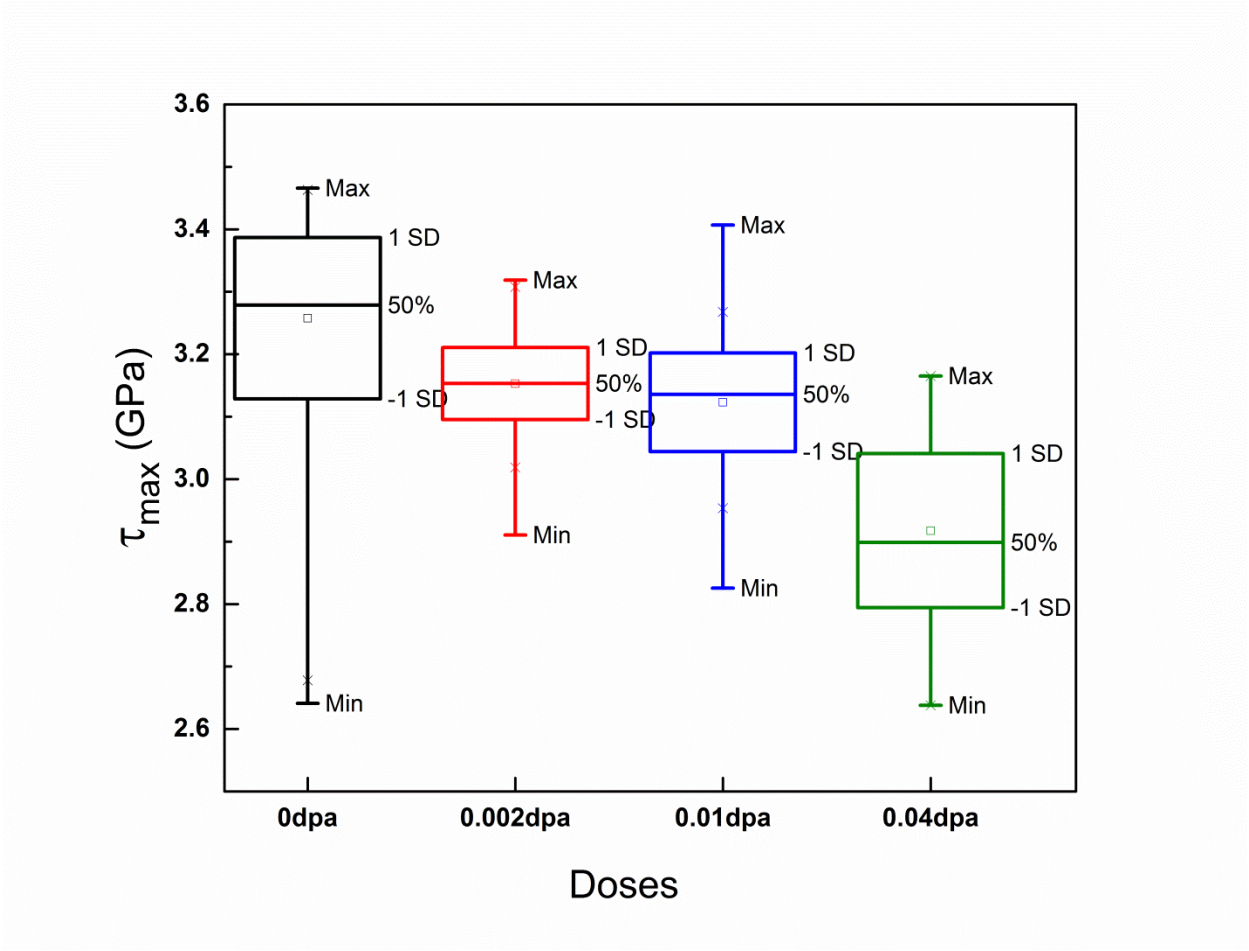

Fig. 2.5 Box plots of the maximum shear stresses (τ_{max}) of first pop-ins at different doses with mean value, median, minimum, maximum and standard deviation (SD) shows the tendency of τ_{max} and deformation inhomogeneity as a function of doses.

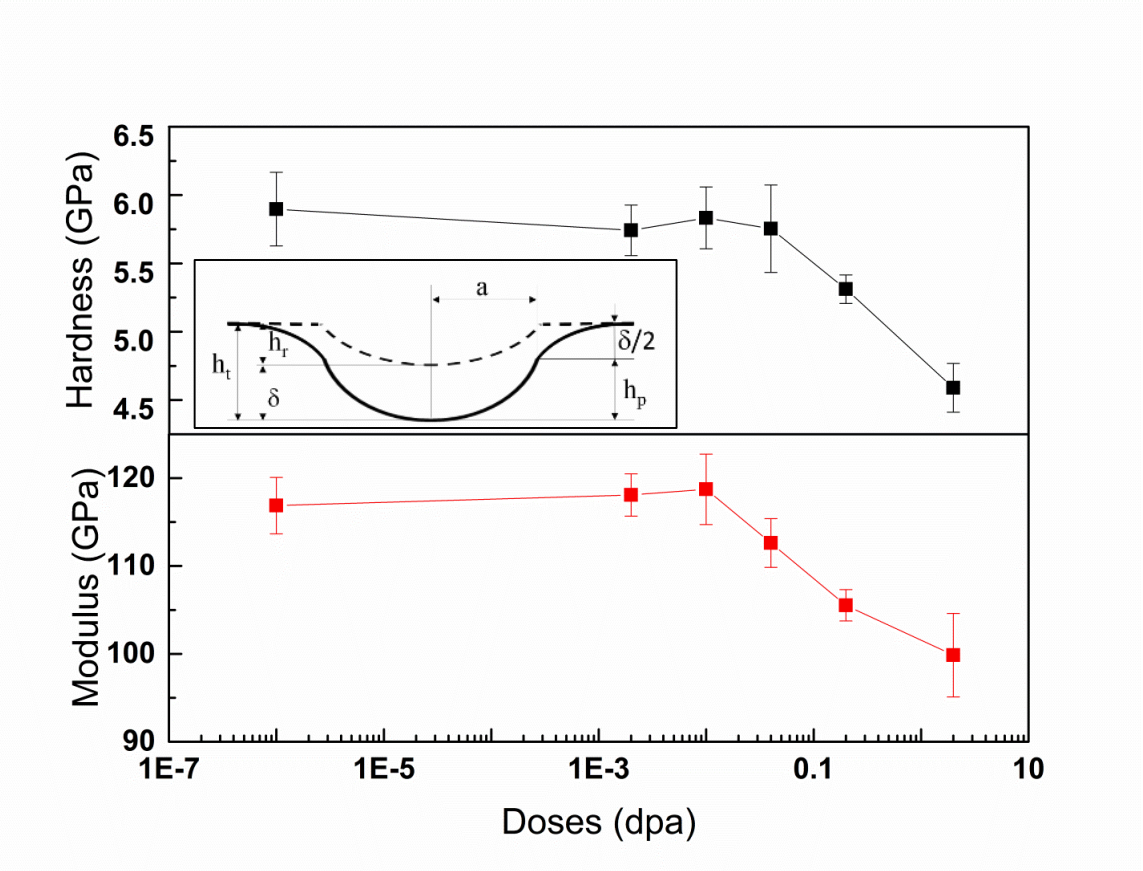

Fig. 2.6 Hardness and modulus as a function of doses estimated by nanoindentation tests using a simple model of spherical indentation. the inset is illustration of the relationship between the depth of loaded and unloaded indentations.

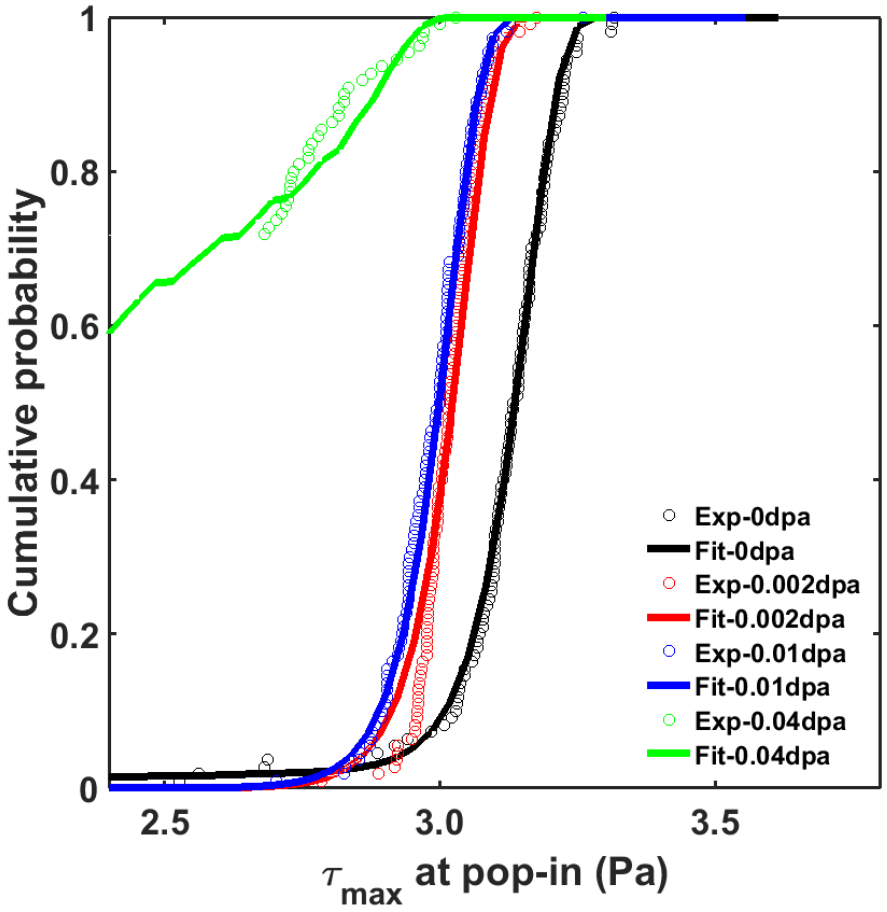

Fig. 2.7 Plots of cumulative probability and fitting curves of τ_{max} at first pop-in at different irradiation doses, where the dots represent experimental data and the solid lines are fitting results by the unified structural model. Since only a few pop-ins are not observed on 0.04 dpa sample, cumulative probability is calculated by considering these pop-in stresses being infinitesimals to compare with the other samples

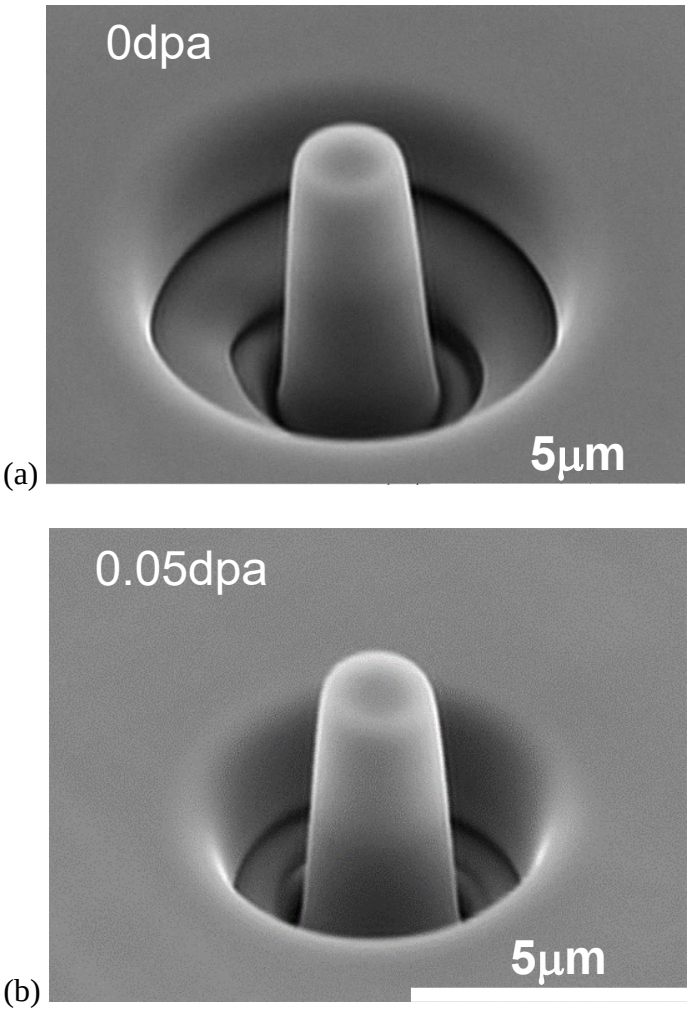

Fig. 2.8 Representative micropillars at different doses (a) 0 dpa to (b) 0.05 dpa, (c) 0.2 dpa, (d) 1 dpa and (e) 10 dpa before compression showing high-quality cylinders milled by FIB. One of three micropillars of each irradiation doses are illustrated for examples

(c)

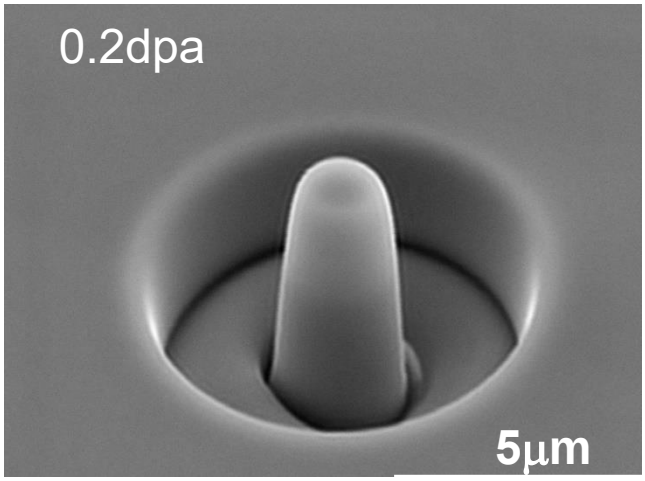

(d)

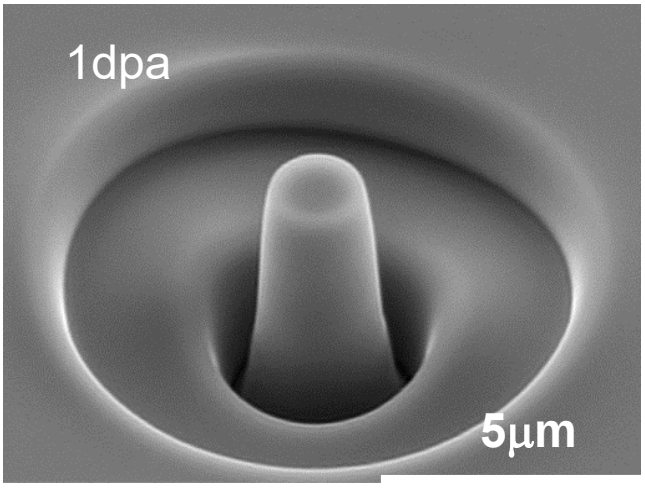

(e)

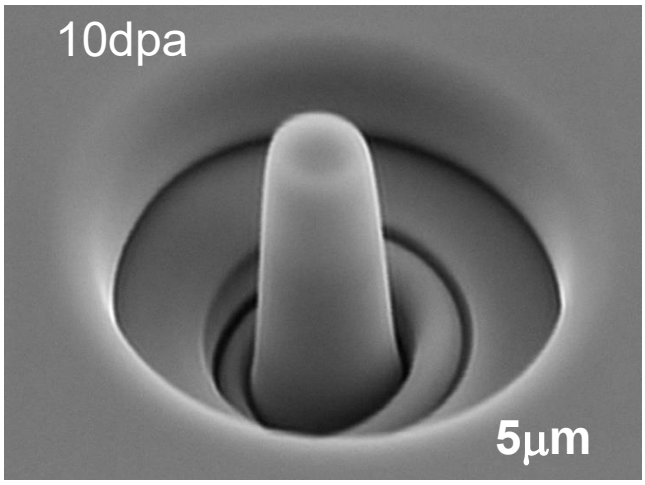

Fig 2.8 (continued)

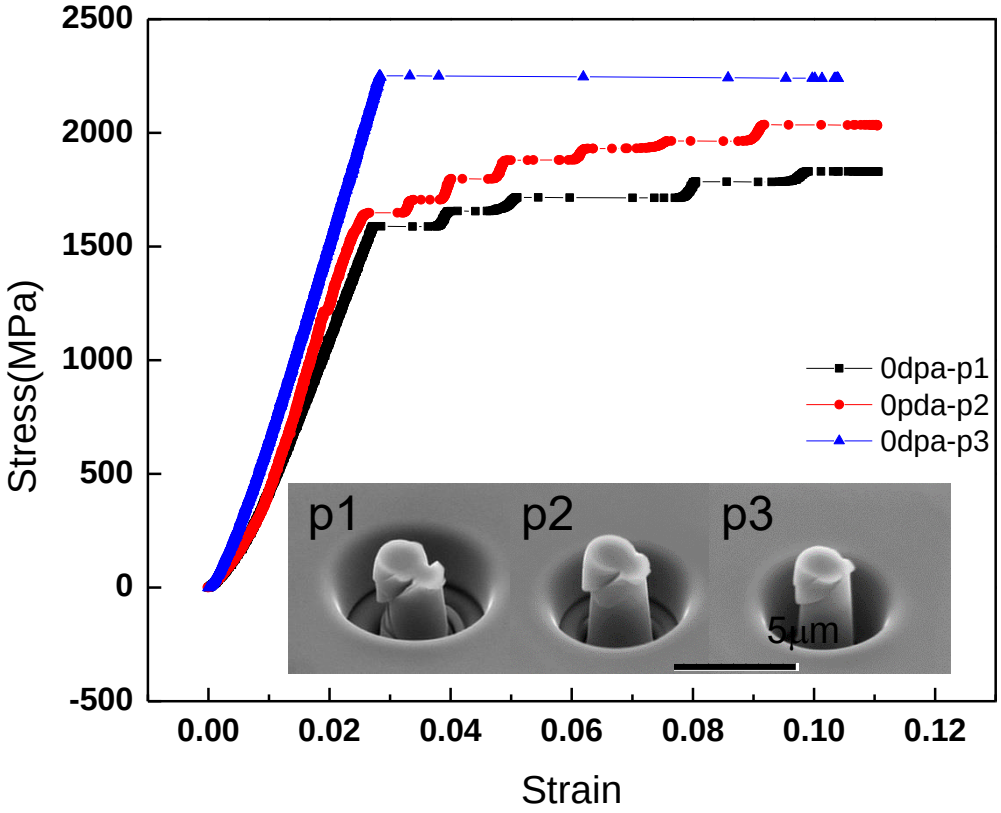

(a)

Fig. 2.9 Compressive engineering stress-stain curves of (a) the unirradiated sample and the samples irradiated to (b) 0.05 dpa, (c) 0.2 dpa, (d) 1 dpa and (e) 10 dpa. The SEM images of each deformed micropillar are inserted. The inserted black circle indicates the excursion responding to shear band formation.

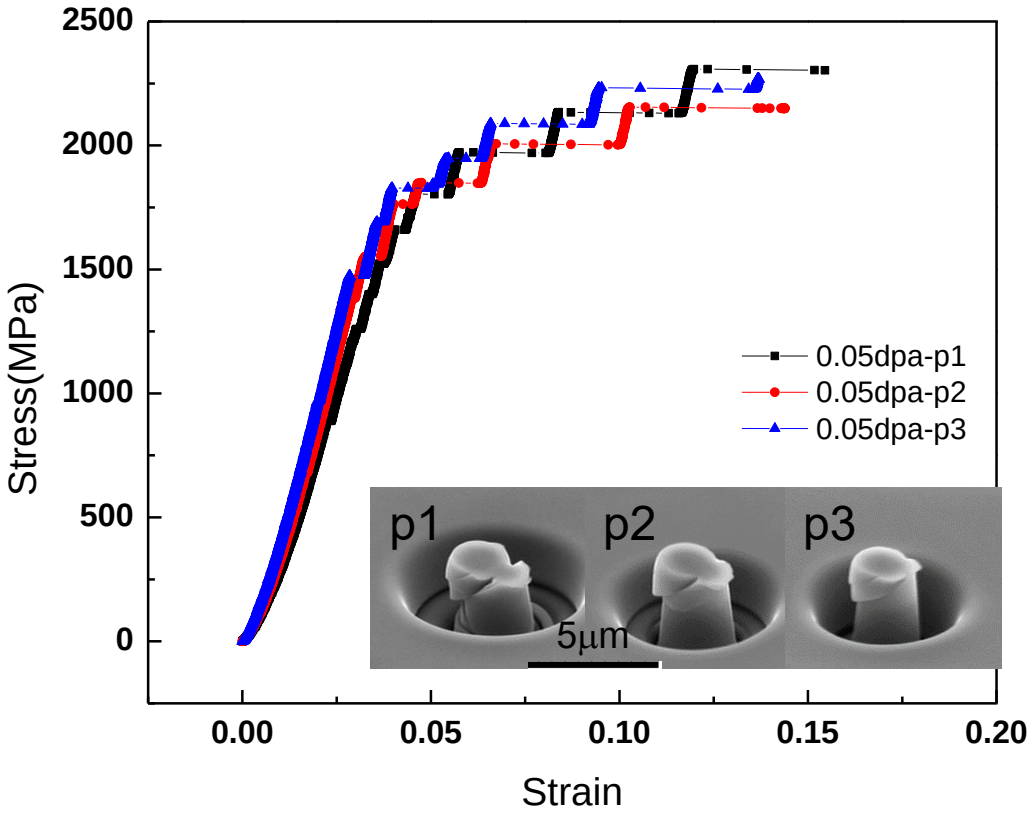

(b)

Fig 2.9 (continued)

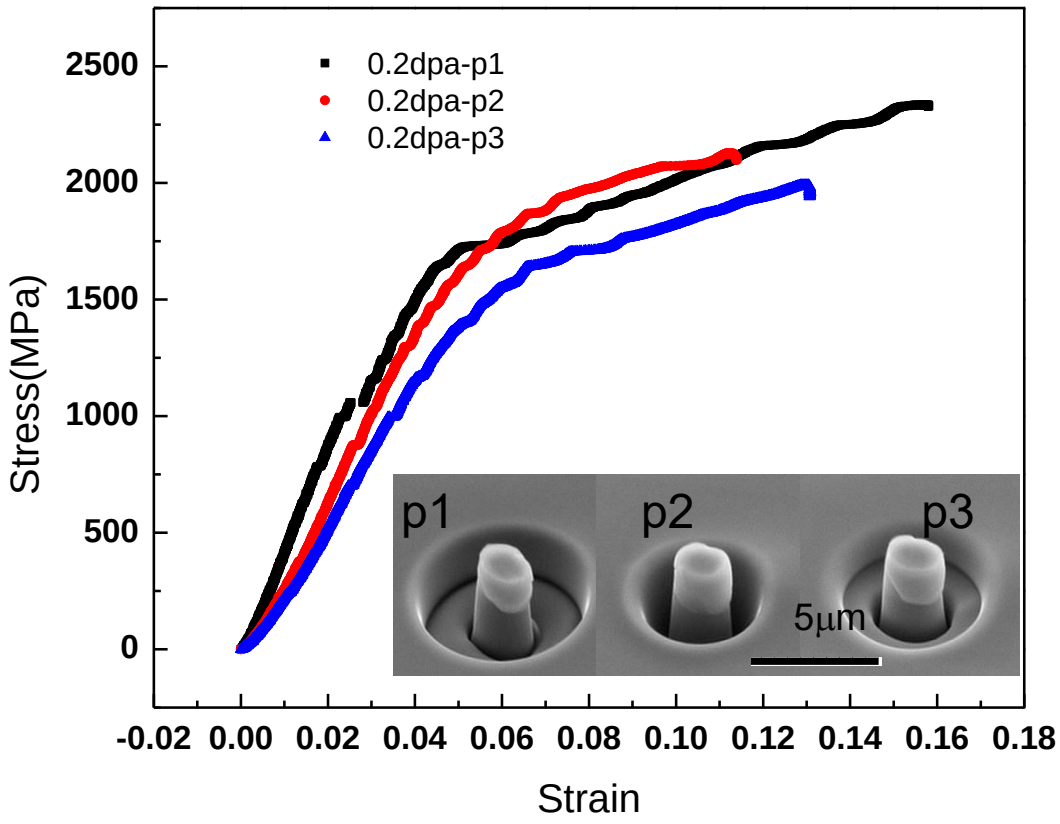

(c)

Fig 2.9 (continued)

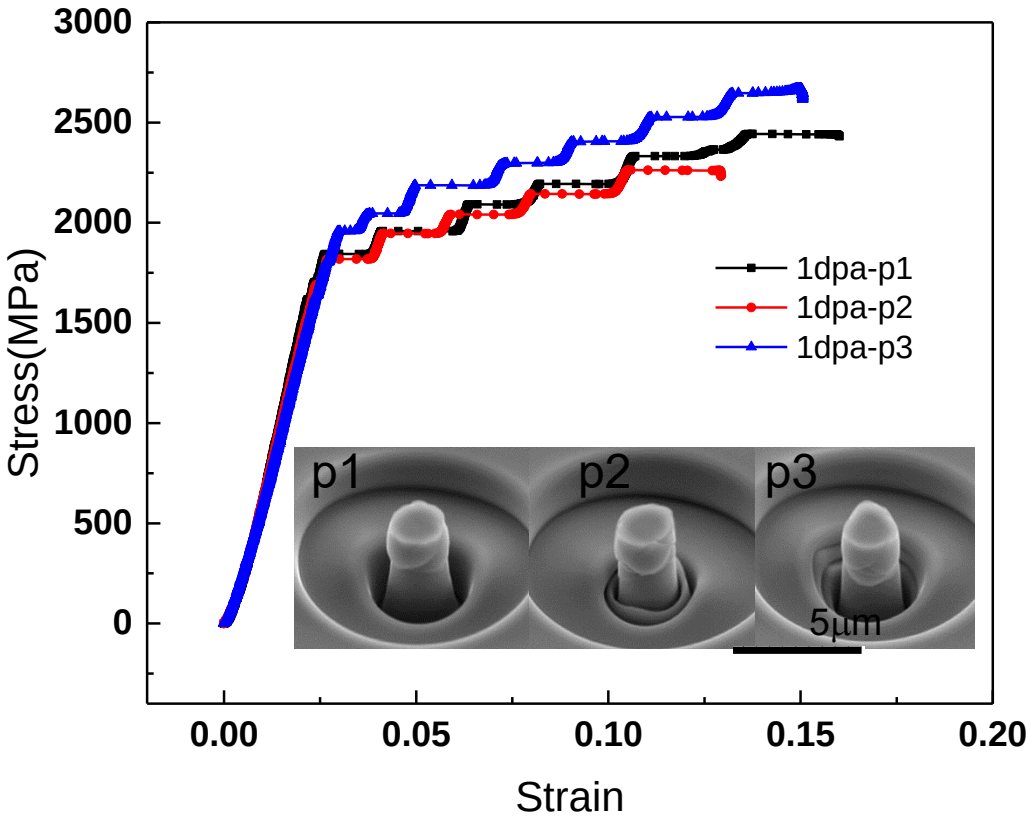

(d)

Fig 2.9 (continued)

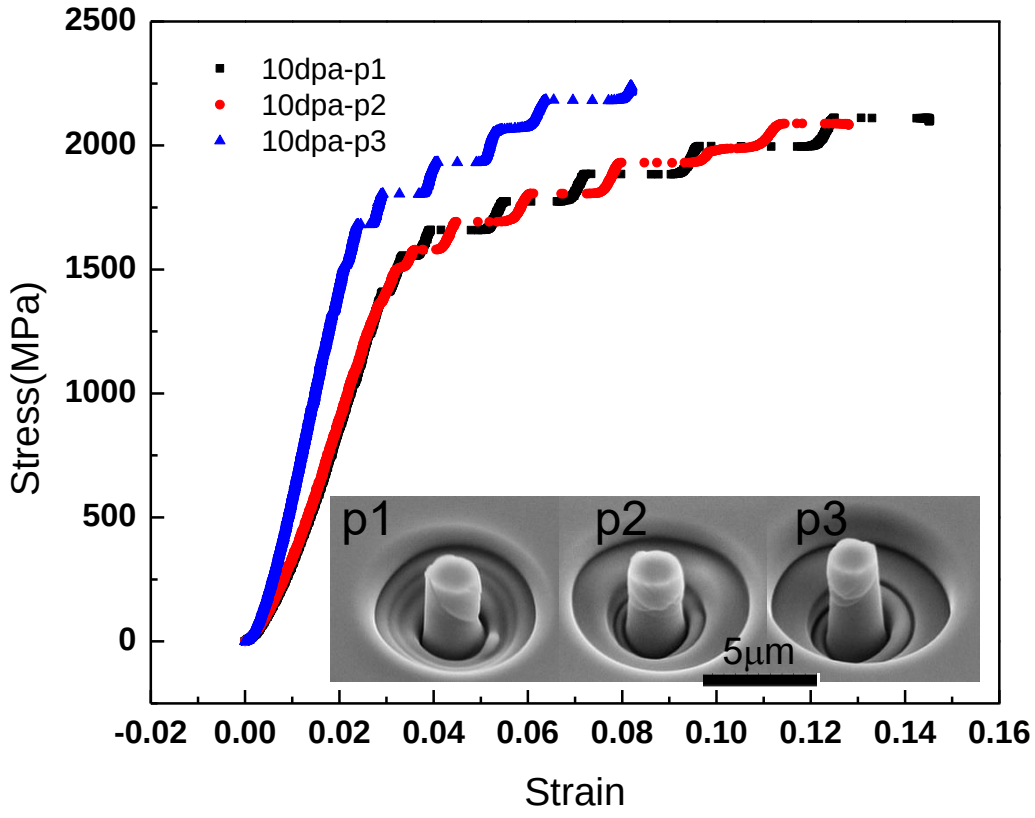

(e)

Fig 2.9 (continued)

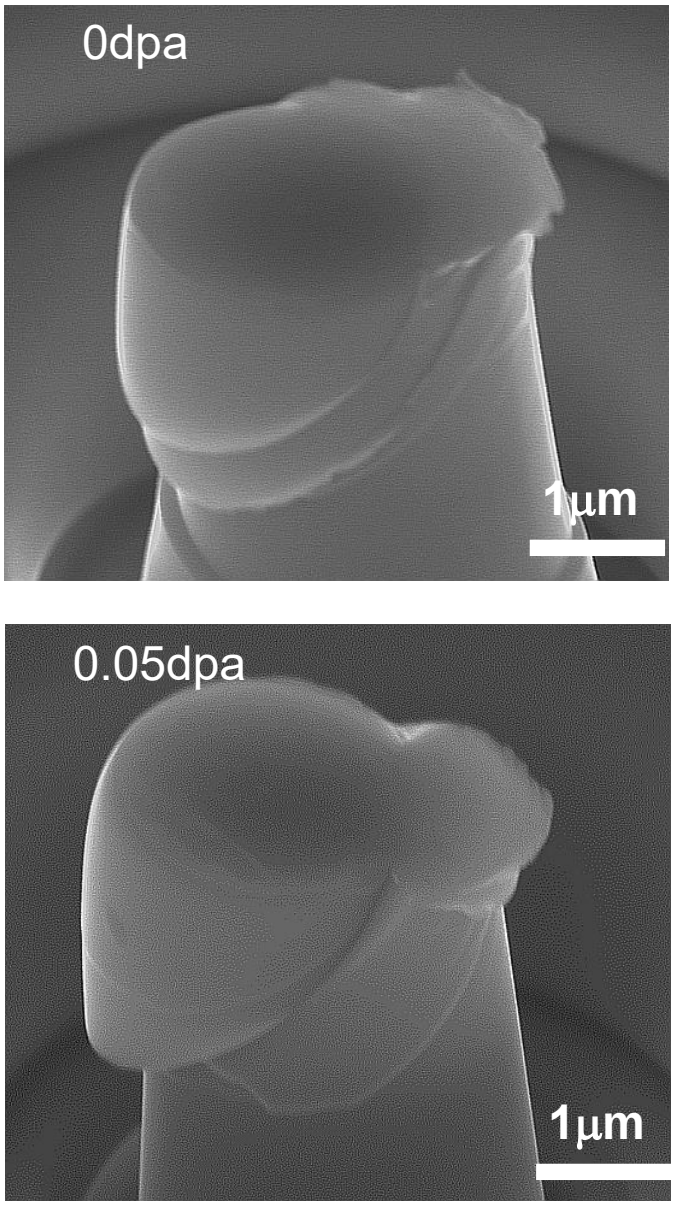

Fig. 2.10 Representative SEM images of the micropillar at irradiation doses of (a) 0 dpa, (b) 0.05 dpa, (c) 0.2 dpa, (d) 1 dpa and (e) 10 dpa in high resolution showing the shear band morphology after compression under a flat indenter. One of three micropillars of each irradiation doses are illustrated for examples.

(c)

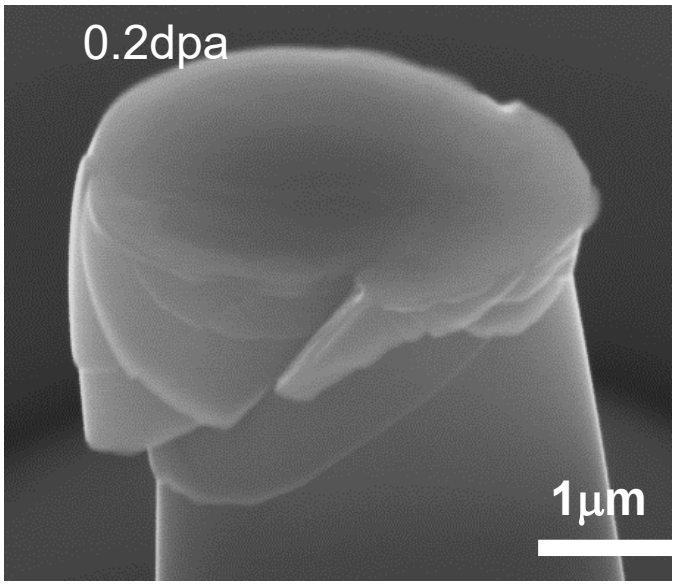

(d)

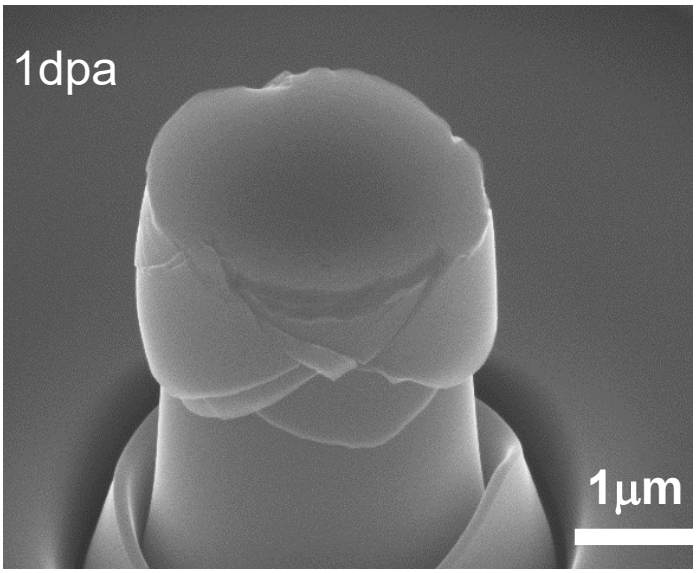

Fig 2.10 (continued)

(e) 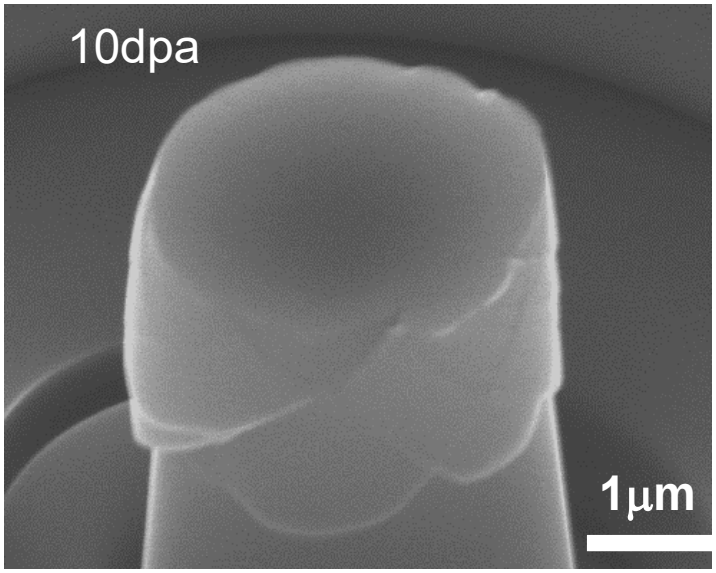

Fig 2.10 (continued)

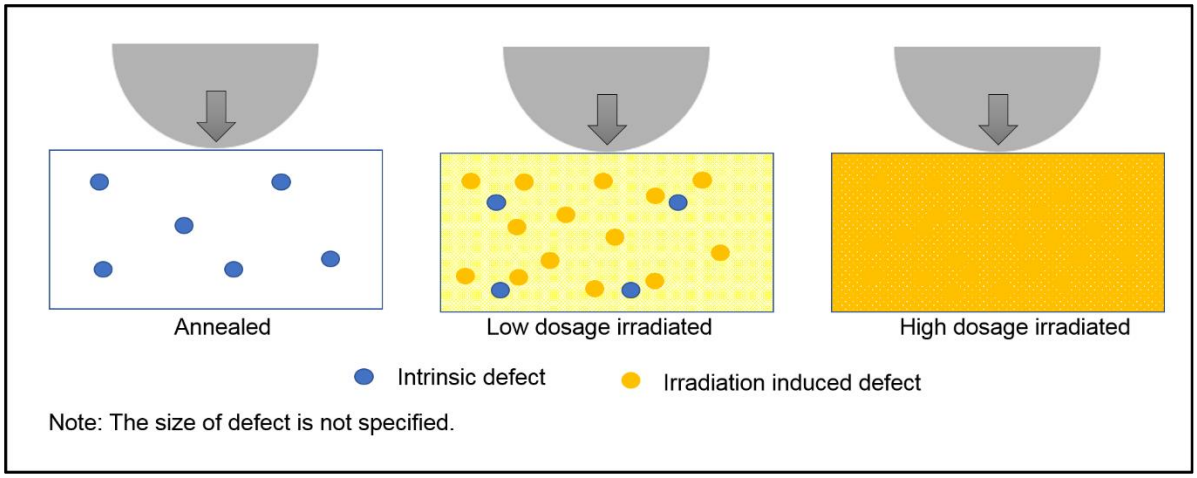

Fig. 2.11 Schematic illustration of irradiation induced defect and the structural changes indicating a transition the annealed state to intermediate state and finally to a different structural state obtained in irradiated samples after relatively high-level irradiation.

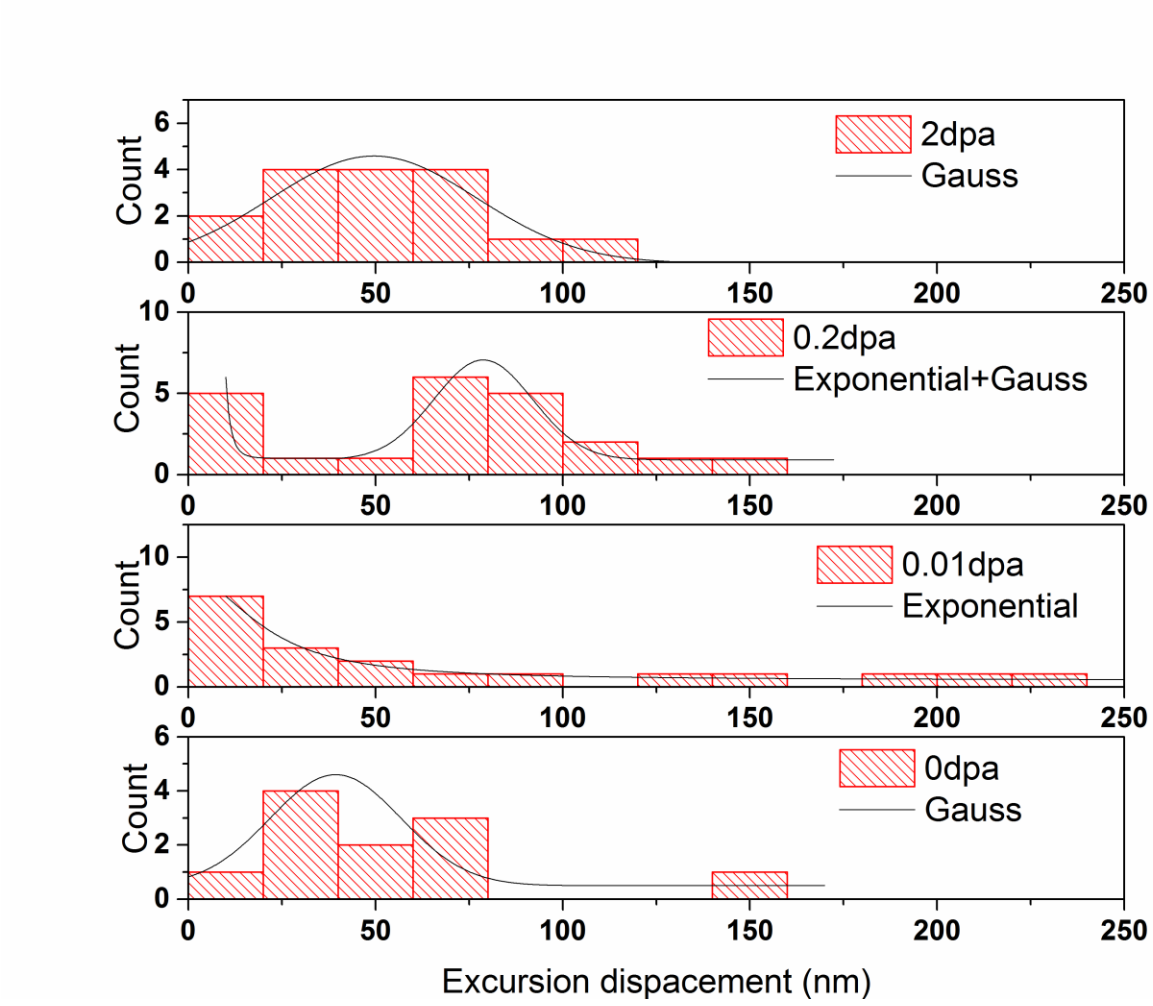

Fig. 2.12 Histograms of excursion displacement of micropillar compression tests in the sample irradiated to 0 dpa, 0.05 dpa 1 dpa and 10 dpa. The histogram is schematically fitted by Gauss function and Exponential function to distinguish the structural signature related the energy release of shear banding of different structural states.

CHAPTER III

TWINNING-MEDIATED WORK HARDENING AND TEXTURE EVOLUTION IN CRCOFEMNNI HIGH ENTROPY ALLOYS AT CRYOGENIC TEMPERATURE

A version of this chapter was originally published by in 2017:

T.K. Liu, Z. Wu, A.D. Stoica, Q. Xie, W. Wu, Y.F. Gao, H. Bei and K. An: Twinning-mediated work hardening and texture evolution in CrCoFeMnNi high entropy alloys at cryogenic temperature Mater Design. 131, 419 (2017).

Authors:

T.K. Liu

Department of Materials Science and Engineering, University of Tennessee, Knoxville, TN 37996, United States

Materials Science and Technology Division, Oak Ridge National Laboratory, Oak Ridge, TN 37831, United States

Chemical and Engineering Materials Division, Oak Ridge National Laboratory, Oak Ridge, TN 37831, United States

Z. Wu, H. Bei

Materials Science and Technology Division, Oak Ridge National Laboratory, Oak Ridge, TN 37831, United States

A.D. Stoica, Q. Xie, W. Wu, K. An

Chemical and Engineering Materials Division, Oak Ridge National Laboratory, Oak Ridge, TN 37831, United States

Y.F. Gao

Department of Materials Science and Engineering, University of Tennessee, Knoxville, TN 37996, United States

Materials Science and Technology Division, Oak Ridge National Laboratory, Oak Ridge, TN 37831, United States

T.K. Liu's involvement in this article: designed and conducted experiments, analyzed the experimental data, discussed with other authors, wrote and revised the article.

Co-authors' contributions are listed as follows: Z. Wu helped T.K. Liu with experiments of microstructure characterization and sample preservation. A.D. Stoica contributed to data analysis and texture calculation. Q. Xie discussed the results of texture evolution and helped with the calculation of orientation. W. Wu conducted neutron experiments of texture measurement. Y.F. Gao discussed the results and revised the article. H. Bei fricated the alloys, conducted the following heat treatment and the discussion of results. K. An provided research guidelines, discussed the data and revised the article.

Abstract

The cryogenic plastic deformation of CrCoFeMnNi high entropy alloy is characterized by three distinct stages based on the change of the work hardening rate. Microstructure and bulk texture at different strain levels were studied by electron backscatter diffraction (EBSD) and neutron diffraction. Our findings indicate that the deformation twins led to the constant work hardening rate at Stage II and resulted in the appearance of <115>//TA texture component, while the dislocation slip was involved all though the entire plastic deformation. The twinning-mediated tensile plastic deformation at cryogenic temperature finally induced the strong {111}-<112> texture component and minor {001}<110> texture component accompanied with twinning-induced {115}<552> texture component.

1. Introduction

High entropy alloys (HEAs) are multi-component metallic materials containing at least five principle elements with equimolar ratios, and are solid solutions of simple face-centered cubic (FCC), body-centered cubic (BCC), or hexagonal close-packed (HCP) structures [1-5]. Due to their promising properties, such as high strength, ductility, toughness and good resistance to corrosion and fatigue, HEAs have attracted considerable research interest, including studies on the alloying effect, formation, phase stability, microstructure and mechanical behaviors [6-11]. The vast research of mechanical properties has been summarized in the review paper of HEAs [12]. Particularly, the crystal structure, alloying elements, heat treatment and processing play dominant roles in

microstructural development of grains, e.g., grain size and grain orientation dramatically affect the strength and ductility of HEAs [13-15]. FCC HEAs have shown increasing of the yield strength, ultimate tensile strength and ductility at low temperature and even high retained strength at high temperature [16, 17]. Furthermore, FCC HEAs have a good combination of tension elongation and strength and the exceptional facture toughness exceeding 200 $MPa \cdot m^{1/2}$ down to 77K [18]. Two deformation mechanisms have been found at 77K, that are dislocation slipping and deformation twinning, which contribute to the increase in ductility and high fracture toughness at the cryogenic temperature [18, 19]. The occurrence of twinning is attributed to the low stacking fault energy of this HEA, which was reported to be about 20-25mJ/m^2 [20]. Moreover initiation and evaluation of deformation twins is strongly affected by the grain orientation [21], which has not been fully understood.

Like other metals with a good balance of high strength and ductility, FCC HEAs show high work hardening. Various deformation mechanisms such as slip, twinning, grain reorientation or phase transformation could induce the change of work hardening rate as a function of the strain [22, 23]. Usually, upon further deformation, the work hardening rate continuously decreases due to the reduction of dislocation density increase rate. It is well accepted that this continuous decreasing work hardening rate is associated with dynamic recovery process governed by the glide of dislocations under the action of the applied stress, despite the specific details of underlying dislocation mechanisms [24, 25]. On the other hand, discontinuous change of work hardening rate could indicate the onset or suppression of some microstructural phenomena during deformation [26]. For example, some materials

with a low stacking fault energy (SFE) like nickel alloys, brass, and steels etc. show decreasing work hardening interrupted by a steady work hardening which is attributable to deformation twins [27, 28].

Among the extensively investigating mechanical behaviors of the model simple-structure CrCoFeMnNi FCC HEA, it is interesting to note three distinguishable stages of work hardening at cryogenic temperature [29]. Referring to Fig. 3.1 as an example, three-stages work hardening is proposed: Stage I (<13%) being the early rapid decrease of work hardening rate; Stage II (13%~36%) being a steady state of work hardening at medium plastic strain range; and lastly Stage III (>36%) being a continuous decreasing of work hardening rate. It is hypothesized that the constant work hardening rate is a result of deformation twins, which provide barriers to dislocation glide, thus increasing dislocation storage and decreasing their mean free path [22, 23]. Deformation twin is also hypothesized to be responsible for texture changes during plastic deformation [30, 31]. The overall texture evolution of HEA, as a result of severe slipping and twinning, has not been reported or investigated in the above scenario, which is convoluted with deformation mechanism by affecting Schmid factor and resolve shear stress associated with crystallographic orientation [32, 33].

Being an important material property, crystallographic texture is recognized as an unneglectable factor that can control the deformation behaviors of materials including HEAs. The techniques such as X-ray diffraction (XRD) and electron backscatter diffraction (EBSD) measurements have been used in the research of local crystal orientation distributions of HEAs and related behaviors [34-36]. Considering the bulk texture being

important to the overall bulk property of materials, it is necessary to obtain statistically sufficient information from a large enough volume. Neutron diffraction measurement with more than a few mm^3 scattering gauge volume serves this need well because of neutron's deep penetration and it has been successful in understanding materials deformation behaviors in engineering materials [37-42], in comparison to the XRD and EBSD that only probe the localized portion of the material. Thus, here we utilized neutron diffraction to measure the bulk texture to understand its role on the work hardening behavior of HEAs.

In the current study of the CrCoFeMnNi HEA, we report the evolution of slips, twins and grain reorientations after interrupted mechanical testing by electron backscatter diffraction (EBSD) and neutron-diffraction measurements of pole figures (PFs), and illustrate the microstructure-texture relationship and its correlation to the discontinuous work hardening behavior. This study provides a profound and complete understanding of the relationship connecting the property, microstructure and bulk texture in the CrCoFeMnNi HEA.

2. Materials and methods

The CrCoFeMnNi HEA was prepared as the same methods described in Ref [43]. Flat dog-bone specimens with a gage length of 10 mm were cut from the cold-rolled sheet with their longitudinal direction (LD) along the rolling direction (RD) followed by annealing at 1173K for 1 hour with subsequent air cooling. The initial microstructure of annealed specimen was examined by scanning electron microscopy. Tensile tests were carried out at a nominal engineering rate of 10^{-3} s^{-1} at 77K by submerging in a liquid nitrogen environment, where the tension axis (TA) is parallel to LD. Five specimens were

tested and interrupted at different strain levels (true strains of 7%, 13%, 27%, 41% and 51%), which were cut in half to study microstructure and texture evolution after plastic deformation. The JEOL 6500F FEG-SEM equipped with a TSL OIM EBSD system was used to examine the microstructure at different strain levels. The twin fraction was estimated by OIM software. Two criteria were applied for characterizing twins: 1) the orientation of the twin is related to the parent through a specific misorientation. The primary recrystallization twin in a face-centered-cubic material is related to the parent by a rotation of 60° around the <111> crystal direction; 2) the twinning plane must be aligned with the boundary plane separating the twin from the parent. The annealing twin faction was estimated at the strain levels of 0%, 7%, 13% and 27% by calculating inverse pole figure (IPF) maps including hundreds of grains. Due to the distinguishable microstructure morphology of annealing and deformation twins, four individual grains containing deformation twins were chosen to calculate the deformation twin fraction after its initiation. It should be noted that the spatial resolution of current EBSD experiment is 0.2 μm, EBSD could only detect twin bundles rather than individual deformation twin. The twin band spacing and twin band width were estimated by averaging four misorientation line profiles identified by 60° misorientation within the individual grain containing deformation twins on IPF maps. The IPFs were calculated from EBSD results to compare with texture measurement obtained by neutron diffraction.

The pole figures (PFs) were measured by neutron diffraction at the VULCAN Diffractometer [44]. To obtain complete pole figures at VULCAN [45], the specimen was rotated around the normal direction from 0° to 90° denoted by Ψ, and loading direction

from 0° to 360° denoted by Φ. The diffraction data was collected by rotating Ψ angles every 5° and Φ angles every 30°, respectively. Neutron diffraction set-up and measurement is schematically illustrated in Fig. 3.2. The neutron diffraction data were fitted by single-peak-fitting method using the VRDIVE program [46]. The integral intensity of (111), (220), (220), (311) and (420) diffraction peaks was used to generate the complete pole figures. The full orientation distribution function (ODF) was calculated by all (111), (200), (220), (311), (331) and (420) pole figures using the Matlab toolbox MTEX [47], and then the IPFs were calculated from ODF by MTEX.

3. Results

The microstructure of the CrCoFeMnNi alloy after annealing is shown in Fig. 3.3. The homogeneous equiaxed grains were obtained by annealing. The grain size varies from 10 μm to 50 μm with the mean value of 35 μm. The profuse annealing twins are clearly visible after annealing. The tiny black spots scattered in Fig. 3.3 are probably Mn-Cr oxides which were found in the same material [48]. The neutron diffraction plot of annealed alloy is presented in Fig. 3.4. It is should be noted that many high *hkl* indices diffraction peaks were detected by neutron, while only six low-*hkl*-index peaks are illustrated. The neutron diffraction pattern indicates that the annealed HEA still possesses a single phase of face-centered-cubic structure. Even though the dispersed black spots are the Mn-Cr oxides, it does not reflect on the diffraction pattern because of its low volume faction.

The EBSD inverse pole figure (IPF) maps in Fig. 3.5 present the microstructure evolution of the CrCoFeMnNi deformed to the different strain levels. The initial microstructure of the undeformed specimen is the same as shown before. Large annealing

twins were found with the estimated volume fraction of 25%. The identification of annealing twins is shown in Fig. 3.6, where the blue represents parent grains, red represents annealing twins and grey represents undefined region. The twin faction evolution during plastic deformation is illustrated in Fig. 3.7. The annealing twin fraction retained a constant around 25% as the initial state. When the specimen was strained to 7%, the microstructure in Fig. 3.5(b) did not change significantly; no obvious deformation twins were found, whereas the observed grain interior orientation fluctuation was caused by dislocation motion induced local lattice rotation. Marked in the black square in Fig. 3.5(c), the deformation twin was found in the enlarged area as shown in Fig. 3.5(g) at the strain of 13% around the beginning of Stage II. According to the Schmid factor contours calculation [49], an initial parent <111>//TA orientation would convert to a final <115>//TA orientation through the twinning process. Accordantly, the twin-parent orientation analysis in Fig. 3.5(g) indicates an orientation transition from <111> to <511> as illustrated in the inverse pole figure, and 60° rotation around the <111> axis as shown in the (111) pole figure. Both the morphology features and the twin-parent orientation verify the newly formed deformation twins at the beginning of Stage II. The deformation twin fraction increased with plastic strain starting from Stage II as shown in Fig. 3.7. Because of the limited spatial resolution of EBSD, the deformation twin fraction is likely overestimated compared with the high-resolution transmission electron microscopy. Nevertheless, the EBSD can show the general trend of deformation twin evolution. The deformation twin band spacing (D_{twin}) and twin band width (W_{twin}) were summarized in Table 1, showing D_{twin} in the decreasing trend and W_{twin} in the increasing as the deformation twins developed. When plastic strain

increases to 27% in Stage II, more deformation twins were found and most of them were formed and propagated inside the grains with <111>//TA orientation, which agreed with the deformation twinning activated on FCC {111} system [50]. In Fig. 3.5(e) and (f) at plastic deformation to 41% and 51% strains in Stage III, extensive deformation twins were further generated with the maximum deformation twin fraction of 12%. Disappearance of the greenish color grains indicates that the <110> oriented grain was unstable at the large strain greater than 41% during the tensile deformation. More heavily distorted grains were elongated along the TA direction and exhibited orientation preference mainly along <100>//TA and <111>//TA, showing in blue and red colors.

To correlate the microstructure-bulk texture relationship due to the interaction of dislocation slip and twinning, the bulk texture evolution was carefully studied at the same strain levels as microstructure investigation. First of all, the initial texture is measured and shown in Fig. 3.8. Both {111} and {200} pole figures indicate that the specimen still presents weak preferred orientation even through high temperature annealing, which did not thoroughly eliminate the heavy rolling texture. The texture evolution will be discussed by the means of IPFs and ODF.

The IPFs along loading direction are shown in Fig. 3.9 illustration texture evolution during tensile plastic deformation. IPFs of Fig. 3.9 (a)-(f) were calculated from EBSD results, which represent the surface information because of the low electron incident depth. Both the intensity at <100> //TA and <111>//TA increased with plastic strains except for the 7% strain, which may be caused by insufficient statistic information, i.e. lacking grain number. Compared with EBSD IPFs, neutron diffraction provides more persuasive and

complete texture information due to its high penetration and large diffraction volume. As the same trend of increasing <100> //TA and <111>//TA intensity, the orientation distribution is more concentrated to <111> orientation in Fig. 3.9 (g)-(l). Both EBSD and neutron IPFs indicate the final tensile texture consist of <100> //TA and <111>//TA rather than <110> //TA texture components. However, IPFs do not provide any evidence of deformation twin activity during tension since <115>//TA twinning texture component overlap with tensile texture component near the <100> orientation on IPFs. Therefore, ODF plots are presented as follows.

By averaging over the whole bulk section, the ODF plot completely provides a global material behavior. ODF φ_2=45° sections are chosen to present. Fig. 3.10(a) shows that the weak initial texture consisted of a (111)[-1-12] main texture component combined with a (112)[1-31] minor texture component. At the first 7% true strain, the results of slight increase in intensity and the unchanged orientation distribution profile reveal that small rotation of grains was induced by dislocation slipping at the low strain level. In further deformation as in Stage II, it can be clearly seen in Fig. 3.10(b)-(d), the (111)[-1-12] component increased greatly. It is obviously found that the texture components evolved towards <111>//LD and less <001>//LD. This could be expected as the typical tensile texture in FCC as aforementioned; however, in this HEA, the texture is mainly a result of twinning as well. Due to the small volume of the twins at the beginning of Stage II as seen in Fig. 3.5(c), the orientation transition due to twinning is difficult to be extracted from the ODF section in Fig. 3.10(c), reflecting the negligible twinning contribution on the overall texture. However, with the increasing deformation twins fraction, the {115}<552> texture

components were developed as a result of twinning activities as shown in Fig. 3.10(e) and (f) in corresponding to EBSD analysis, but less intense than the main {111}<112> component. Note that the slipping induced intensity increasing nearby <001>//TA could overlap twinning induced <115>//TA, hence the {115}<552> texture components on the ODF section are supposed to be contributed by twinning and slipping simultaneously [51]. The decreasing intensities of <110>//TA component trending to zero on the ODF sections agree with the observation of disappearance of greenish grain in EBSD IPF maps.

4. Discussion

The cryogenic plastic deformation of these HEAs is governed by dislocation slipping at small strain level, and then mediated by deformation twin at high strain levels. Hence the dislocation development and deformation twin activities will be discussed. The dislocation density evolution during plastic deformation was calculated from the neutron diffraction peak breadth. Peak profile analysis has become a popular method to determine the dislocation density and grain size [52-54]. The contribution of dislocation density ρ to peak breadth β can be estimated as [55]:

$$\beta = \frac{b\sqrt{C\rho}}{F\left(R_e\sqrt{\rho}\right)} \quad (1)$$

where b is the magnitude of the Burgers vector, C is the contrast factor of dislocation, F is an integral factor in Wilkens's approach [56], Re is the outer cut-off radius of dislocation strain field. According to the assumption in Ref [52] the value of Re is proposed as $\ln(R_e/b) = 2\pi$. Here, $F\left(R_e\sqrt{\rho}\right)$ is assumed to be approximately equal to 2π.

For specific *hkl* diffraction, b and C can be regarded as constants. Hence, the square of peak breadth is proportional to dislocation density respect to the same *hkl* diffraction:

$$\left(\frac{\beta}{\beta_0}\right)^2 = \frac{\rho}{\rho_0} \tag{2}$$

where β_0 and ρ_0 are the peak breadth and dislocation density of reference state, respectively.

The derived dislocation densities from peak broadening for (111) and (200) diffractions are shown in Fig. 3.11. The different slopes result from different contrast factors in (111) and (200) diffraction. The calculated dislocation densities showed monotonic increase versus the plastic strain. This reveals that dislocation motions and propagations were involved in the overall plastic deformation, which agrees well with the increasing contrast in the image quality (IQ) maps of Fig. 3.12 presented in the following part.

The dislocation slip started at beginning and was active through the whole plastic deformation. The image quality (IQ) maps in Fig. 3.12(a)-(f) clearly demonstrate the increasing uneven contrast arising from the grain boundaries (red lines), the twin boundaries (green lines) and the local strain related to the development of dislocations. The IQ images in Fig. 3.12(a)-(c) and the calculated dislocation density in Fig. 3.11 show that the early plastic deformation was mainly predominated by dislocation slip when the twinning was not activated. The dislocation of the type 1/2<110> were identified by the transmission electron microscopy to believe that the early plastic deformation is governed by the planar slip of 1/2<110> type dislocations on {111} planes [19]. The local structure disorder rising from different elements in HEA is hypothesized to hinder dislocation

motion, likely resulting in high work hardening rate. When the increasing stress by work hardening reached a certain value larger than an identical critical resolve shear stress, deformation twinning was initiated at Stage II by the glide of Shockley dislocation of the same sign on the successive {111} planes, which has been experimentally proved in the FCC austenitic stainless steel [57]. Even though the material initially contains high volume fraction annealing twins which hardly become effective barriers for dislocation movement due to their equivalent length of grain size, whereas they may increase the strength based on classic Hall-Petch effect. But beyond all that, extensive thin deformation twins are able to interact with dislocations effectively, giving rise to them acting as obstacles to dislocation motion. The interaction enables to accumulate dislocations within twin lamellae [58] and to generate high local stresses especially at twin tips which exceed the critical stress of twin nucleation thereby producing more twins. Thin deformation twins creating excessive high angel boundaries with strong effect on dislocation glide leads to dynamic Hall-Petch effect [59]. Therefore, the decrease of work hardening rate was compensated by dynamic Hall-Petch effect, showing steady rate in Stage II. On the other hand, the interaction of twins and dislocations could also result in shear induced twin boundary migration due to an acting Peach-Koehler force on the twin boundary from local stress field, thereby increasing the twin width and twin volume fraction. As the strain increased, the dislocation density continued increasing as shown in Fig. 3.11, while the twin initiation activities reduced and tended to saturate as shown in Fig. 3.5 at the strain levels of 41% and 51%. Thus, the work hardening rate decreased again due to the less activities of deformation twin nucleation. At large strain level, severe plastic deformation

is usually accommodated by grain reorientation related to the slip activities. Hence, the <111> and <100> fiber texture components are expected via large tensile strain induced specific grain rotation in FCC metals [60], which agrees with the orientation preference demonstrated in EBSD images and IPFs.

5. Conclusion

In summary, we showed the twinning-mediated work hardening, microstructure and texture evolution during interrupted plastic deformations of the CrCoFeMnNi high entropy alloy at cryogenic temperature. The cryogenic plastic deformation of CrCoFeMnNi HEA is characterized by three distinct stages based on the change of work hardening. It is found that the annealed CrCoFeMnNi HEA contains high fraction (25%) annealing twins. Deformation twins were observed to initiate at the 13% strain at the beginning of Stage II. The formation of deformation twins leads to the constant work hardening rate. The texture investigations indicate strong <111>//TA and weak <001>//TA tensile texture components after severe plastic deformation as the conventional FCC materials. The presence of {115}<552> texture component mainly came from twinning activities, which does not significantly contribute to overall texture at the end, comparing with the strong <111>//TA fiber texture and relative weak <001>//TA fiber texture due to slip after severe tensile deformation.

References

[1] J.W. Yeh, S.K. Chen, S.J. Lin, J.Y. Gan, T.S. Chin, T.T. Shun, C.H. Tsau, S.Y. Chang, Adv Eng Mater, 6 (2004) 299-303.

[2] C.J. Tong, M.R. Chen, S.K. Chen, J.W. Yeh, T.T. Shun, S.J. Lin, S.Y. Chang, Metall Mater Trans A, 36a (2005) 1263-1271.

[3] M.A. Hemphill, T. Yuan, G.Y. Wang, J.W. Yeh, C.W. Tsai, A. Chuang, P.K. Liaw, Acta Mater, 60 (2012) 5723-5734.

[4] M.C. Gao, B. Zhang, S.M. Guo, J.W. Qiao, J.A. Hawk, Metall Mater Trans A, 47a (2016) 3322-3332.

[5] Y.J. Zhao, J.W. Qiao, S.G. Ma, M.C. Gao, H.J. Yang, M.W. Chen, Y. Zhang, Mater Design, 96 (2016) 10-15.

[6] Y. Zhang, X. Yang, P.K. Liaw, Jom-Us, 64 (2012) 830-838.

[7] C.P. Lee, Y.Y. Chen, C.Y. Hsu, J.W. Yeh, H.C. Shih, Thin Solid Films, 517 (2008) 1301-1305.

[8] Z. Wu, H. Bei, Mat Sci Eng a-Struct, 640 (2015) 217-224.

[9] Y.Z. Shi, B. Yang, P.K. Liaw, Metals-Basel, 7 (2017).

[10] L.Y. Tian, G.S. Wang, J.S. Harris, D.L. Irving, J.J. Zhao, L. Vitos, Mater Design, 114 (2017) 243-252.

[11] C. Zhang, F. Zhang, H.Y. Diao, M.C. Gao, Z. Tang, J.D. Poplawsky, P.K. Liaw, Mater Design, 109 (2016) 425-433.

[12] E.J. Pickering, N.G. Jones, Int Mater Rev, 61 (2016) 183-202.

[13] Y. Zhang, T.T. Zuo, Z. Tang, M.C. Gao, K.A. Dahmen, P.K. Liaw, Z.P. Lu, Prog Mater Sci, 61 (2014) 1-93.

[14] Y.J. Zhou, Y. Zhang, Y.L. Wang, G.L. Chen, Appl Phys Lett, 90 (2007) 181904.

[15] Z.G. Wu, Y.F. Gao, H.B. Bei, Acta Mater, 120 (2016) 108-119.

[16] A. Gali, E.P. George, Intermetallics, 39 (2013) 74-78.

[17] Z. Wu, H. Bei, G.M. Pharr, E.P. George, Acta Mater, 81 (2014) 428-441.

[18] B. Gludovatz, A. Hohenwarter, D. Catoor, E.H. Chang, E.P. George, R.O. Ritchie, Science, 345 (2014) 1153-1158.

[19] F. Otto, A. Dlouhy, C. Somsen, H. Bei, G. Eggeler, E.P. George, Acta Mater, 61 (2013) 5743-5755.

[20] S. Huang, W. Li, S. Lu, F.Y. Tian, J. Shen, E. Holmstrom, L. Vitos, Scripta Mater, 108 (2015) 44-47.

[21] Z. Wu, C.M. Parish, H. Bei, J Alloy Compd, 647 (2015) 815-822.

[22] B. Devincre, T. Hoc, L. Kubin, Science, 320 (2008) 1745-1748.

[23] J.P. Bressanelli, A. Moskowitz, Asm Trans Q, 59 (1966) 223-239.

[24] U.F. Kocks, H. Mecking, Prog Mater Sci, 48 (2003) 171-273.

[25] Y. Estrin, L.S. Toth, A. Molinari, Y. Brechet, Acta Mater, 46 (1998) 5509-5522.

[26] S. Asgari, E. ElDanaf, S.R. Kalidindi, R.D. Doherty, Metall Mater Trans A, 28 (1997) 1781-1795.

[27] A.W. Thompson, M.I. Baskes, W.F. Flanagan, Acta Metall Mater, 21 (1973) 1017-1028.

[28] L. Remy, Acta Metall Mater, 26 (1978) 443-451.

[29] G. Laplanche, A. Kostka, O.M. Horst, G. Eggeler, E.P. George, Acta Mater, 118 (2016) 152-163.

[30] L. Bracke, K. Verbeken, L.A.I. Kestens, Scripta Mater, 66 (2012) 1007-1011.

[31] T. Leffers, J.B. Bildesorensen, Acta Metallurgica Et Materialia, 38 (1990) 1917-1926.

[32] W.D. Callister, Materials Science and Engineering: An Introduction, 7th ed., John Wiley & Sons, Inc., New York, PA, 1997.

[33] E. Schmid, Kristallplastizitat. Mit Beosnderer Berucksichtigung der Metalle (in German), 1st ed., J. Springer, Berlin, 1935.

[34] G.D. Sathiaraj, C.W. Tsai, J.W. Yeh, M. Jahazi, P.P. Bhattacharjee, J Alloy Compd, 688 (2016) 752-761.

[35] G.D. Sathiaraj, P.P. Bhattacharjee, C.W. Tsai, J.W. Yeh, Intermetallics, 69 (2016) 1-9.

[36] Tazuddin, K. Biswas, N.P. Gurao, Mat Sci Eng a-Struct, 657 (2016) 224-233.

[37] D.M. Wang, J. Mu, Y. Chen, Y.M. Qi, W. Wu, Y.D. Wang, H.J. Xu, H.F. Zhang, K. An, J Alloy Compd, 696 (2017) 1096-1104.

[38] H. Yang, D. Yu, Y. Chen, J. Mu, Y.D. Wang, K. An, Mat Sci Eng a-Struct, 680 (2017) 324-328.

[39] W. Wu, P.K. Liaw, K. An, Acta Mater, 85 (2015) 343-353.

[40] E.W. Huang, D.J. Yu, J.W. Yeh, C. Lee, K. An, S.Y. Tu, Scripta Mater, 101 (2015) 32-35.

[41] S.Y. Huang, Y.F. Gao, K. An, L.L. Zheng, W. Wu, Z.K. Teng, P.K. Liaw, Acta Mater, 83 (2015) 137-148.

[42] O. Benafan, R.D. Noebe, S.A. Padula, D.J. Gaydosh, B.A. Lerch, A. Garg, G.S. Bigelow, K. An, R. Vaidyanathan, Scripta Mater, 68 (2013) 571-574.

[43] Z. Wu, H. Bei, F. Otto, G.M. Pharr, E.P. George, Intermetallics, 46 (2014) 131-140.

[44] K. An, H.D. Skorpenske, A.D. Stoica, D. Ma, X.L. Wang, E. Cakmak, Metall Mater Trans A, 42a (2011) 95-99.

[45] G.M. Stoica, A.D. Stoica, K. An, D. Ma, S.C. Vogel, J.S. Carpenter, X.L. Wang, Journal of Applied Crystallography, 47 (2014) 2019-2029.

[46] K. An, VDRIVE-Data reduction and interactive visualization software for event mode neutron diffraction, ORNL Report ORNL-TM-2012-621, Oak Ridge National Laboratory, 2012.

[47] R. Hielscher, H. Schaeben, Journal of Applied Crystallography, 41 (2008) 1024-1037.

[48] B.R. Chen, A.C. Yeh, J.W. Yeh, Sci Rep-Uk, 6 (2016).

[49] P. Yang, Q. Xie, L. Meng, H. Ding, Z. Tang, Scripta Mater, 55 (2006) 629-631.

[50] J.W. Christian, S. Mahajan, Prog Mater Sci, 39 (1995) 1-157.

[51] Q. Xie, J. Liang, A.D. Stoica, R. Li, P. Yang, Z. Zhao, J. Wang, H. Lan, R. Li, K. An, Scripta Mater, 137 (2017) 83-87.

[52] T. Ungar, A. Borbely, Appl Phys Lett, 69 (1996) 3173-3175.

[53] T. Ungar, J. Gubicza, G. Ribarik, A. Borbely, Journal of Applied Crystallography, 34 (2001) 298-310.

[54] W. Woo, Z. Feng, X.L. Wang, K. An, B. Clausen, T.A. Sisneros, J.S. Jeong, Mater Lett, 85 (2012) 29-32.

[55] X.L. Wang, Y.D. Wang, A.D. Stoica, D.J. Horton, H. Tian, P.K. Liaw, H. Choo, J.W. Richardson, E. Maxey, Mat Sci Eng a-Struct, 399 (2005) 114-119.

[56] M. Wilkens, Fundamental Aspects of Dislocation Theory, Vol II, in: J. Simmons, R. De Wit, R. Bullough (Eds.) Natl. Bur. Std.(US) Spe, Washington DC 1970, pp. 1195-1221, Publication No. 1317.

[57] E.H. Lee, T.S. Byun, J.D. Hunn, M.H. Yoo, K. Farrell, L.K. Mansur, Acta Mater, 49 (2001) 3269-3276.

[58] O. Bouaziz, S. Allain, C. Scott, Scripta Mater, 58 (2008) 484-487.

[59] I. Gutierrez-Urrutia, D. Raabe, Acta Mater, 59 (2011) 6449-6462.

[60] U.F. Kocks, C.N. Tomé, H.-R. Wenk, Texture and anisotropy: preferred orientations in polycrystals and their effect on materials properties, Cambridge University Press, Cambridge, 1998.

Appendix 3

Table 3.1 the parameters describing annealing twins and deformation twins

Strain	**0%**	**7%**	**13%**	**27%**	**41%**	**51%**
Annealing twin fraction	25.4%	25.6%	25.1%	26.3%	-	-
Deformation twin fraction	-	-	~0%	5.3%	8.3%	12%
Deformation twin band spacing (μm)	-	-	3.6	2.75	2.38	2.93
Deformation twin band width (μm)	-	-	0.35	0.75	0.78	1.08

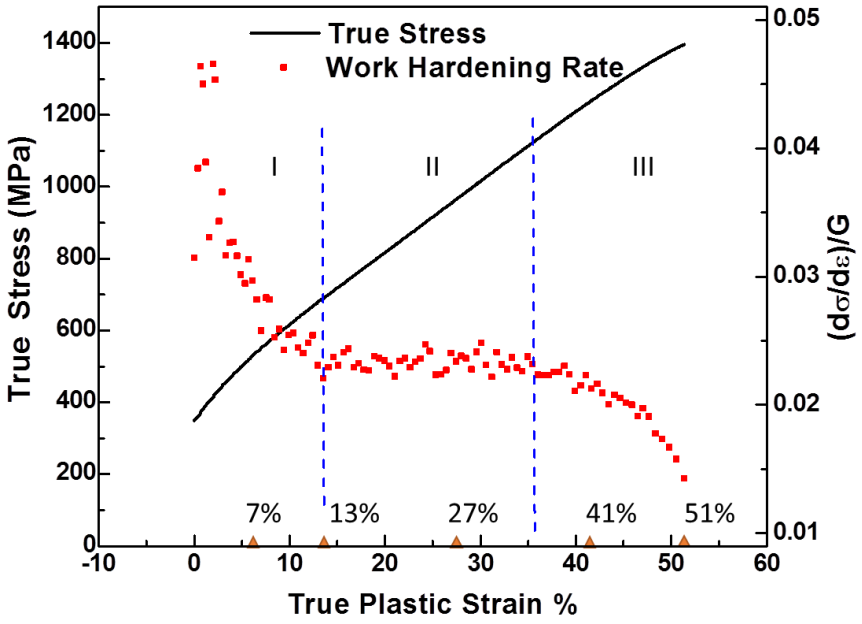

Fig. 3.1 True stress-true plastic strain curve was calculated from engineering stress-strain curve and the normalized work hardening rate, $(d\sigma/d\varepsilon)/G$, as the ratio of derivative of true stress-strain curve over shear modulus G (85GPa). Triangles on the abscissa indicate five interruptions (marked by the corresponding true strain) for microstructural characterization.

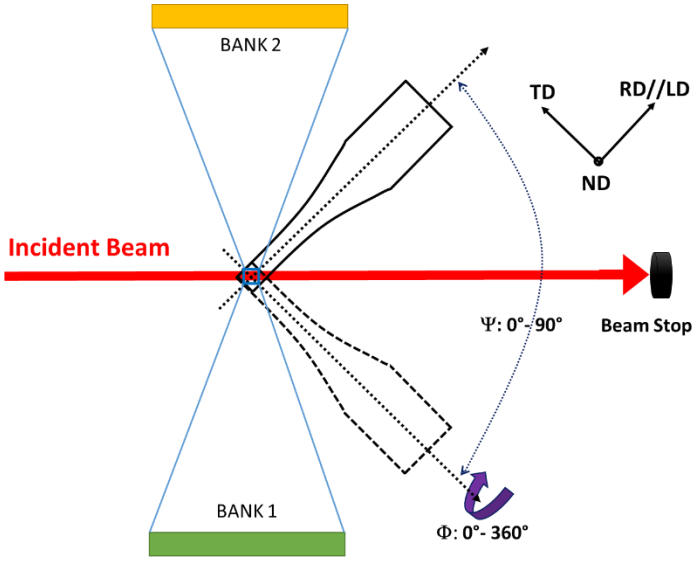

Fig. 3.2 The schematic illustration of the neutron diffraction experiment showing the texture measurement set-up and the definition of Ψ and Φ angles.

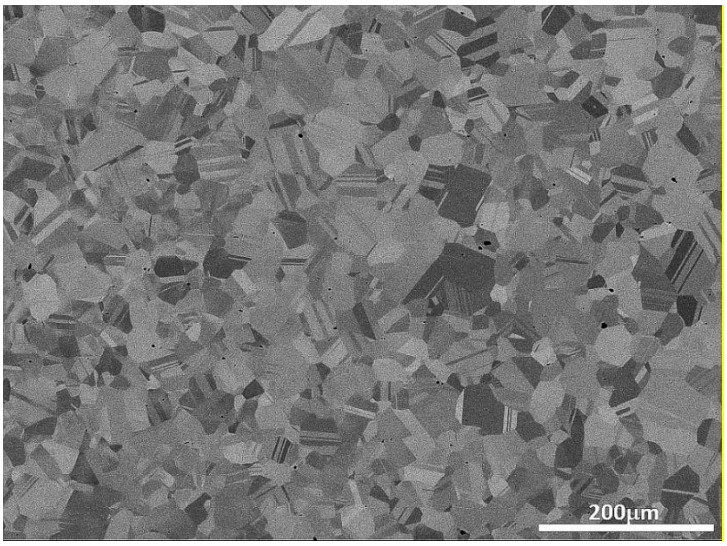

Fig. 3.3 Microstructure of the CrCoFeMnNi alloy after annealing.

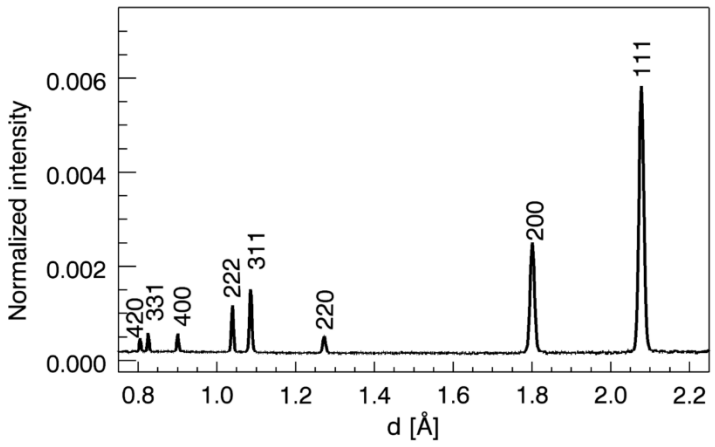

Fig. 3.4 The normalized neutron diffraction pattern of the annealed CrCoFeMnNi alloy.

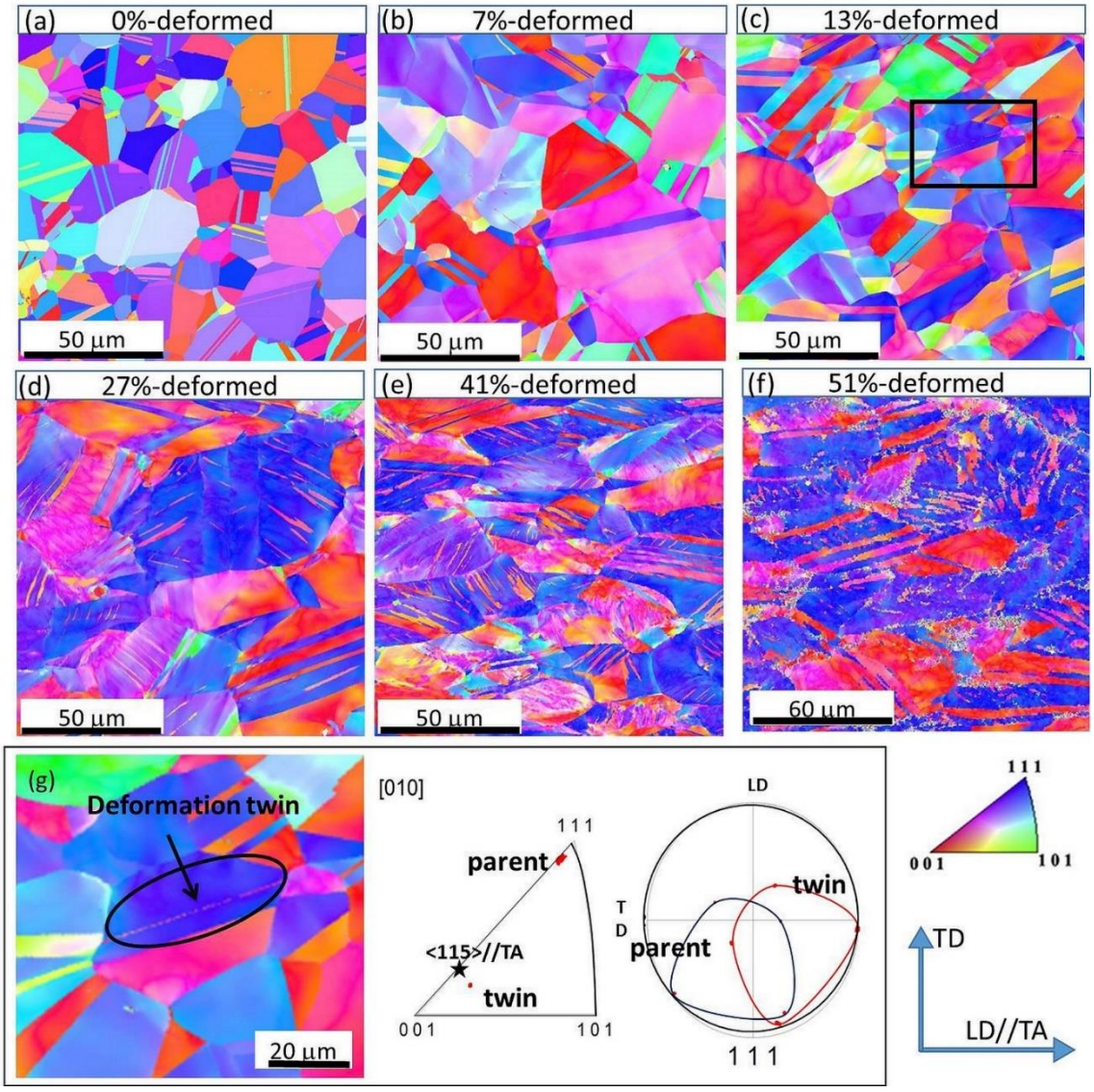

Fig. 3.5 EBSD IPF maps showing the microstructure of CrCoFeMnNi alloys at different true strain levels: (a) 0%, (b) 7%, (c) 13%, (d) 27%, (e) 41%, (f) 51%, and (g) the enlarged area of the black square at the 13% strain showing the newly formed deformation twin at the onset of Stage II. The observed surface normal is perpendicular to tensile axis. The inverse pole figure and pole figure showing the orientation relation of parent and twin, the black star indicating the orientation of <115>//TA. Coloring is the inverse pole figure map projected on loading direction.

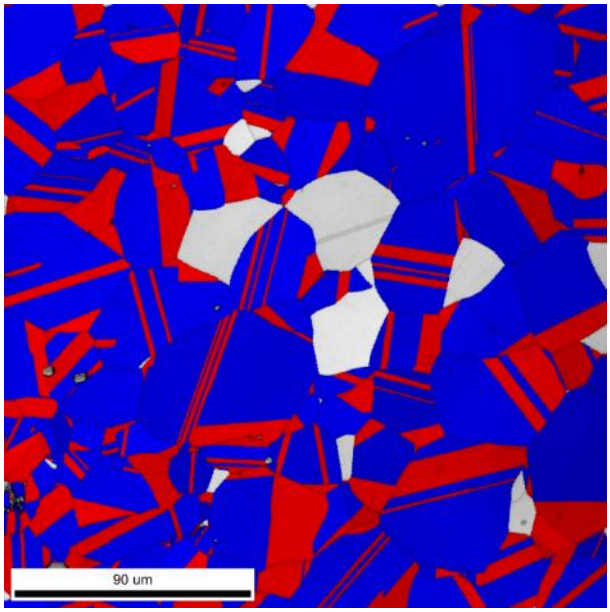

Fig. 3.6 The estimation of annealing twin on the IPF map of undeformed specimen: blue representing parent grains, red representing annealing twins and grey representing undefined region.

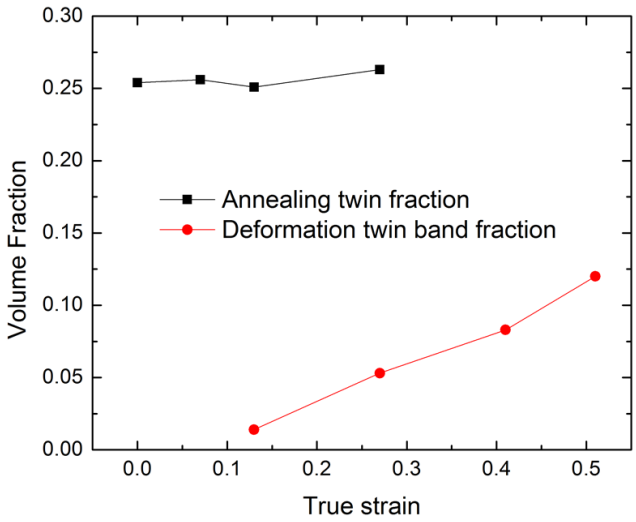

Fig. 3.7 The estimated twin fractions for annealing twins and deformation twins.

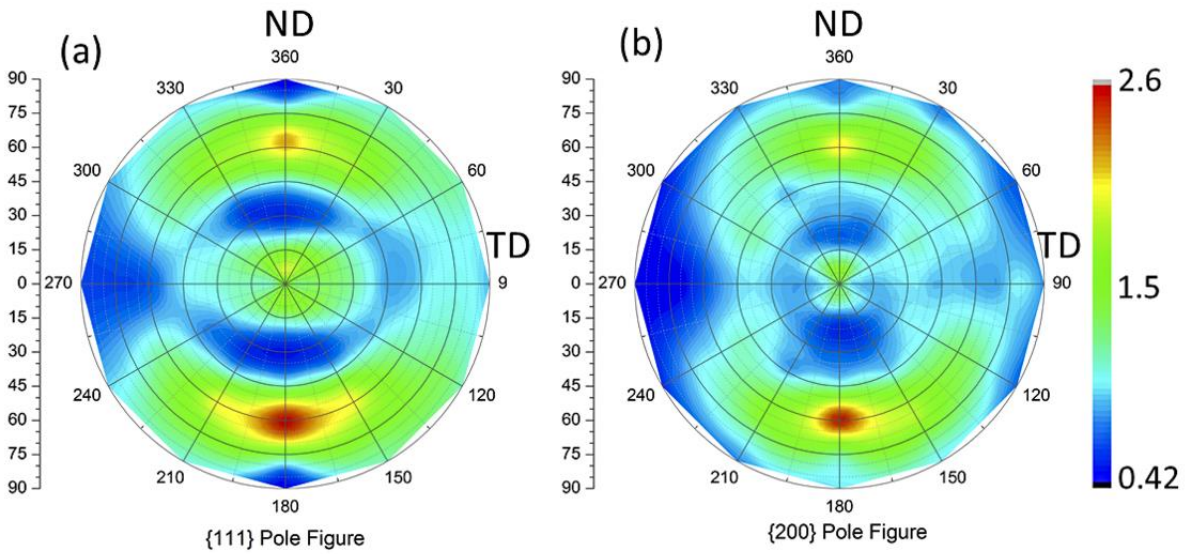

Fig. 3.8 The initial texture represented by (a){111} and (b) {200} pole figures. ND represents the normal direction and TD represents the transverse direction and the z axis if pole figure is along LD.

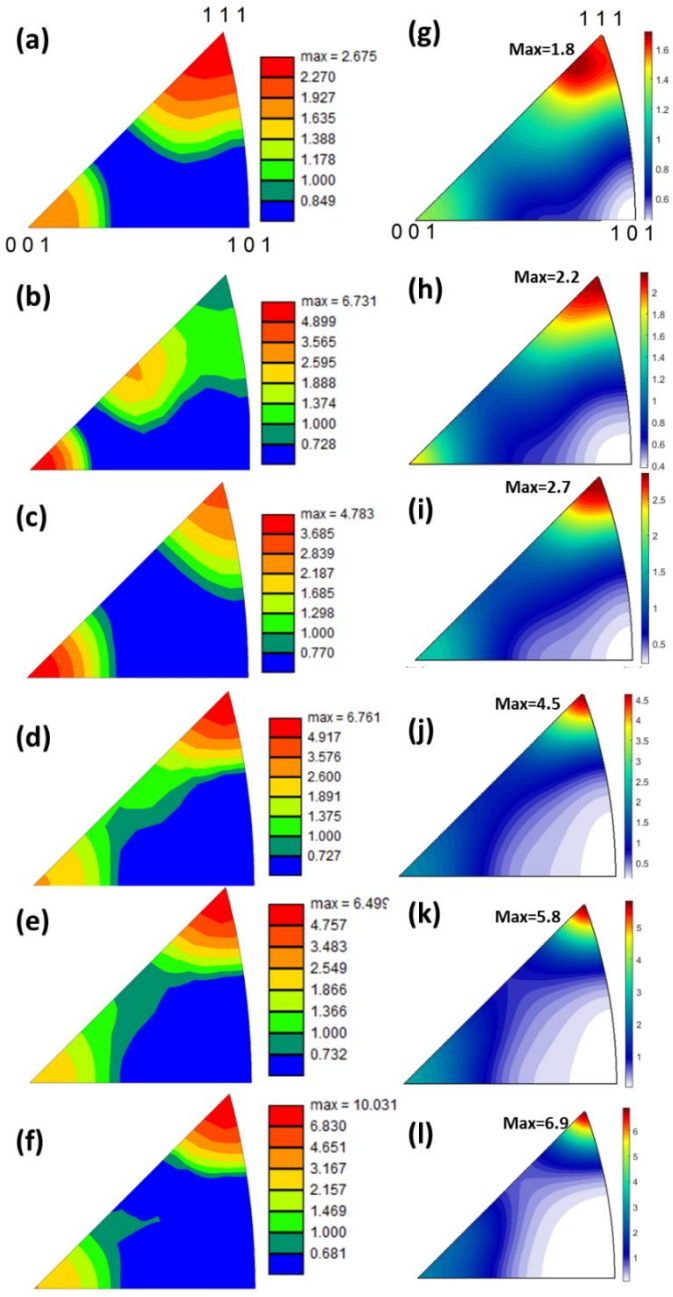

Fig. 3.9 IPFs calculated from EBSD of different strain levels: (a) 0%, (b) 7%, (c) 13%, (d) 27%, (e) 41%, (f) 51%; IPF maps obtained from neutron diffraction: (g) 0%, (h) 7%, (i) 13%, (j) 27%, (k) 41%, (l) 51%.

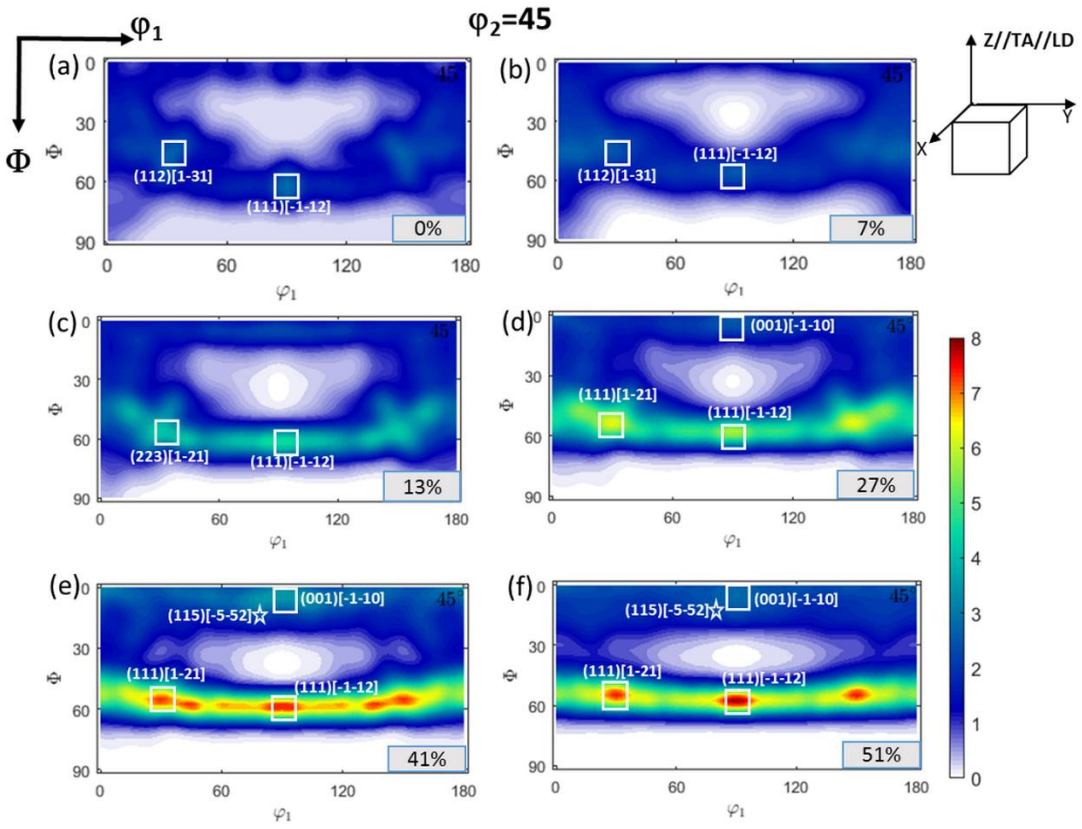

Fig. 3.10 ODF sections of φ_2=45° at different true strain levels, (a) 0%, (b) 7%, (c) 13%, (d) 27%, (e) 41%, (f) 51%. The colored legend bar represents normalized texture index. The coordinate reference accords to Z direction parallel to LD.

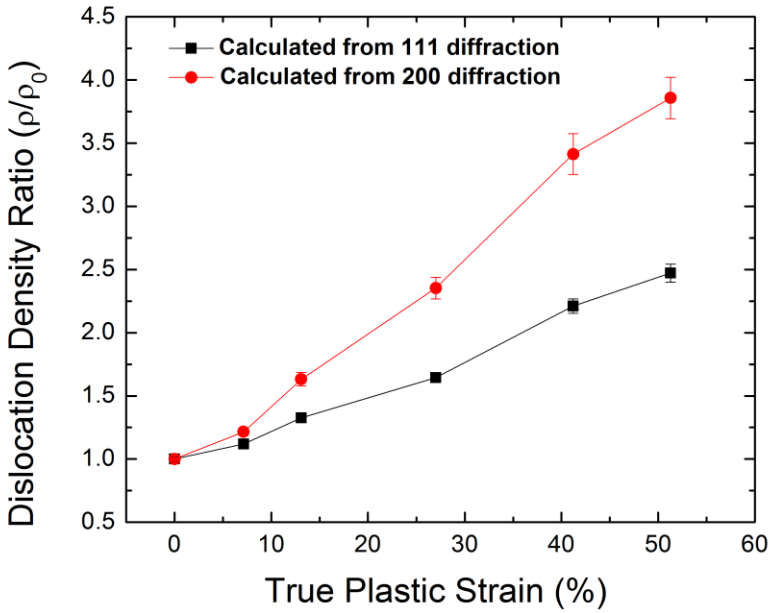

Fig. 3.11 The dislocation density ratio as a function of true strain calculated from {111} and {200} diffraction peak broadening.

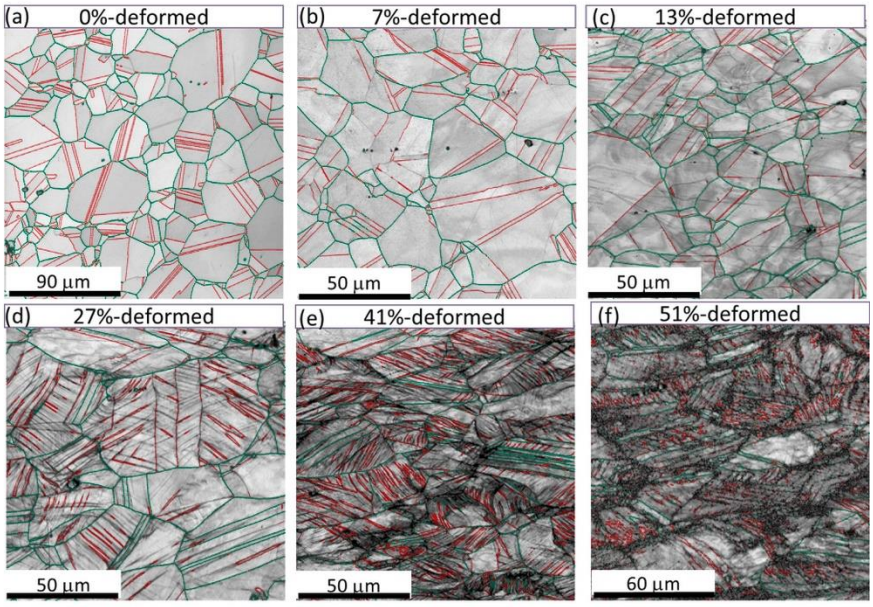

Fig. 3.12 EBSD IQ maps at different true strain levels: (a) 0%, (b) 7%, (c) 13%, (d) 27%, (e) 41%, (f) 51%.

The green lines and red lines indicate grain boundaries and twin boundaries.

CHAPTER IV

IN SITU NEUTRON DIFFRACTION STUDY ON TENSILE DEFORMATION BEHAVIOR OF CARBON STRENGTHENED COCRFEMNNI HIGH ENTROPY ALLOYS AT ROOM AND ELEVATED TEMPERATURES

A version of this chapter was originally published by T. Liu, Y. Gao, H. Bei, and K. An, in 2018:

T. Liu, Y. Gao, H. Bei, K. An, In situ neutron diffraction study on tensile deformation behavior of carbon-strengthened CoCrFeMnNi high-entropy alloys at room and elevated temperatures, J.Mater. Res. (2018) 1–12.

Authors:

T. Liu

Department of Materials Science and Engineering, University of Tennessee, Knoxville, TN 37996, United States, and Materials Science and Technology Division, Oak Ridge National Laboratory, Oak Ridge, TN 37831, United States, and Neutron Scattering Division, Oak Ridge National Laboratory, Oak Ridge, TN 37831, United States

Y. Gao

Department of Materials Science and Engineering, University of Tennessee, Knoxville, TN 37996, United States, and Materials Science and Technology Division, Oak Ridge National Laboratory, Oak Ridge, TN 37831, United States

H. Bei

Materials Science and Technology Division, Oak Ridge National Laboratory, Oak Ridge, TN 37831, United States

K. An

Neutron Scattering Division, Oak Ridge National Laboratory, Oak Ridge, TN 37831, United States

Tingkun Liu’s contributions in the article: designed and conducted experiments, analyzed the experimental data, wrote and revised the article.

Co-authors’ contributions are listed as follows: Hongbin Bei, Yanfei Gao and Ke An assisted with the direction of this work, and the discussion of results.

Abstract

Carbon is doped to CrCoFeMnNi HEA as an interstitial atom, improving the single-phase solid solution alloy with a good combination of strength and ductility at room temperature by introducing deformation twins. In-situ neutron diffraction is applied to investigate the carbon doped CrCoFeMnNi deformation mechanism and micromechanical behaviors during uniaxial tension at room temperature and elevated temperature. With in-situ results accompanied with microstructure and texture measurement, it is found that the plastic deformation is dominated by dislocation slip at an early stage at both temperatures. However, at high strain level, deformation is mediated simultaneously by deformation twins and microbands at room temperature, while it is governed solely by microbands at elevated temperature 573K. The evolution of lattice strain, peak intensity and peak width from in-situ neutron diffraction elucidates the micromechanical behaviors regarding to the role of slips and twins. The texture represented by orientation distribution function indicates that the annealed specimen possesses a relatively strong {112}<110> texture component, and the room-temperature tension deformed texture comprises of slip induced fiber texture and twinning induced {115}<552> texture component.

1. Introduction

Recently, a new alloy design concept called high entropy alloy (HEA) was proposed, which is defined as solid solution alloys with five or more principal elements which should have a concentration between 5 and 35 at. % [1, 2]. These relatively new alloys have attracted increasing interest due to the possibility of producing a combination

of high strength, high ductility and good fracture toughness [3-8]. Despite of multi-phase HEAs, the majority of the studied HEAs are composed of elements which form single phase substitutional solid solutions, of which the substitutional strengthening arises from the lattice distortions.

By the alloy strengthening concept, interstitial strengthening would be another route to improve mechanical properties in HEAs [9-13]. The addition of carbon alloyed into HEAs has been proved to be a successful way to enhance the mechanical properties. The CoCrFeMnNi HEAs doped with 0.5 at.% carbon was firstly reported that addition of carbon in the increased strength and hardening rate in comparison with C-free CoCrFeMnNi alloy due to pronounced activation of mechanical nano-twinning [9]. Further, the effect of carbon content on structure and hardness was investigated in the same alloys [14]. The study of thermomechanical processing on microstructure and mechanical showed that the high strength of the annealed alloy can be attributed to strong grain boundary strengthening and solid solution strengthening by carbon [15]. However, further understanding is still needed to elucidate deformation mechanisms such as twinning induced plasticity (TWIP) in the carbon containing HEAs.

As a powerful method to study the micromechanical behaviors, in-situ neutron diffraction has been widely used to investigate the mesoscopic characteristics such as lattice strain evolution of individual hkl diffraction, peak intensity changed by grain reorientation and peak broadening resulted from local strain during alloy deformations [16-23]. Only a few researches have been reported on HEAs studied by in-situ neutron diffraction [24-27]. The deformation mechanism of CoCrFeMnNi HEAs has been

investigated by in-situ neutron diffraction at room temperature and high temperatures, which is found that the dominant deformation mode is the dislocation glide at 800 K and diffusion-controlled dislocation creep at 1000 K, and deformation at room temperature is likely caused by the motion of mixed dislocations [25, 26]. An in situ neutron diffraction study was done on Mo alloyed FeCoCrNi high entropy alloy, which demonstrated the twinning induced plasticity and microbands induced plasticity [27]. Similar deformation mechanism is expected in the carbon containing CoCrFeMnNi HEAs from interrupted microscopic observations; however, how the dominating deformation mechanism evolves up on different level of straining is not clear, thus an in-situ neutron diffraction work is presented here to take the powerfulness of neutrons to reveal this.

The deformation even dominated by deformation twinning often evolves with dislocation slip, which dramatically causes the complexity and difficulty in the analysis of in-situ neutron diffraction. However, it is well known that the formation of deformation twins will be suppressed when temperature is increased. For example, nano-twinning dominates the deformation of CoCrFeMnNi HEAs at cryogenic condition while only dislocation slip happens when temperature is up to room temperature [9, 28]. Based on the same strategy, the shift of temperature from room temperature to intermediate elevated temperature is expected to hinder deformation twinning in carbon containing HEAs. Thus, the contribution of nano-twinning and slip could be compared in such scenario.

In current work, carbon containing CoCrFeMnNi HEAs deformation mechanism is investigated by in situ neutron diffraction under uniaxial tension at room and elevated temperatures. The micromechanical behavior is analyzed by examining the changes of

lattice strain, peak intensity and width. The comparison at different temperatures is designed to understand the contribution of twinning and dislocation slip at each condition. Texture measurement is conducted by neutron diffraction before and after deformation to determine the slipping and twinning induced texture components. This study is attempting to elucidate the microstructure-texture-mechanical behavior relationship of carbon containing HEAs.

2. Experimental methods

2.1 Materials and processing

Equiatomic single-phase CoCrFeMnNi alloy was produced with the addition of 0.5 at. % carbon by arc melting in argon atmosphere. The rectangular ingot of CoCrFeMnNi-0.5C was fabricated by drop-casting into a copper mold then homogenized at 1,473K for 24 hours, followed by air cooling. The homogenized ingot was cold rolled along the longitudinal direction to a total thickness reduction of ~86%. The dog-bone specimens for tensile tests with a gage length of 14 mm were cut from the cold rolled sheets, followed by recrystallization at 1,373K for 1 h. Before the tensile tests, all faces of sample gage sections were ground through 400-grit SiC papers.

2.2 In-situ neutron diffraction

Neutron diffraction (ND) measurements were performed in situ during tensile loading at the VULCAN Diffractometer [29], Spallation Neutron Source at Oak Ridge National Laboratory. The tensile tests were carried out at two different temperatures, 293K and 573K, with the engineering strain rate lower than 10^{-3} s^{-1}. The specimens were amounted at the load frame with the loading direction (LD) along 45° to the neutron

incident angle so that the two neutron collection banks received the diffracted signals from the longitudinal and the transverse directions of the specimen, respectively. The neutron diffraction data were fitted by single-peak-fitting method using the VRDIVE program, which was used to determine interplanar lattice spacing (d), diffraction peak intensity (I) and full width at half maximum (FWHM). Lattice strain ε_{hkl} was calculated by

$$\varepsilon_{hkl} = \frac{d_{hkl} - d^0_{hkl}}{d^0_{hkl}} \quad (1)$$

where d_{hkl} is the is the interplanar lattice spacing of *hkl* plane at different load steps whereas d^0_{hkl} is the interplanar spacing at the beginning of deformation.

2.3 Microstructure characterization

The microstructure was examined after tensions in the regions of the center (deformed) and grip (undeformed) regions of dog-bone shaped specimen. Both the samples were mounted in in the epoxy resin, then ground though 1200-grit SiC paper and polished though 60nm colloidal silica suspension in the VibroMet vibratory polishing machine to remove minor deformation remaining after mechanical preparation. Their initial microstructures were examined in a tabletop scanning electron microscope (SEM) operated in the back-scattered electron (BSE) mode at an acceleration voltage of 15 kV. Electron backscatter diffraction (EBSD) technique was used to investigate both samples in a field emission gun (FEG) SEM equipped with a TSL OIM EBSD system. The EBSD measurements were performed at an acceleration voltage of 20 kV with step size of 0.01 μm for high fine scanning and 0.2 μm for coarse scanning.

2.3 Texture measurement

Texture measurement was conducted before and after room-temperature tensile tests by neutron diffraction at VULCAN [29]. The initial texture was measured from the grip of dog-bone specimen and the deformation texture was measured near fracture surface. The specimen was rotated from 0° to 360° around loading axis with 30° per step and from 0° to 90° around transverse axis with 15° per step. The diffraction peak intensities of single-peak-fitting were used to generate the pole figures (PF), by which the orientation distribution function (ODF) and loading direction inverse pole figures (LDIPF) were calculated using matlab toolbox MTEX.

3. Results

3.1 Mechanical properties

The engineering stress-strain curves of the CoCrFeMnNi-0.5C specimens tested at both temperatures are shown in Fig. 4.1 (a). The yield stress of the specimen deformed at 293K is about 201MPa, while the yield stress at 573K is about 168MPa. The ultimate tensile stresses (UTSs) are 596MPa and 495MPa for 293K and 573K, respectively. They both have uniform excellent elongation and the elongation slightly increases by 7% when the temperature is increased to 573K. Fig. 4.1 (b) shows the true stress-strain curves and the work hardening rate as a function of true plastic strain. Similar hardening behaviors are observed at both temperatures. During the tension at 293K, work hardening rate rapidly drops initially till to 5% true strain and then keeps constant values of 1.55GPa. By increasing the temperature to 573K, the steady work hardening rate starts at slightly larger

strain and its value reduces to 1.22GPa. After a steady stage, the work hardening rate at both temperatures decreases again tills to fracture.

3.2 Microstructure

The microstructure of CoCrFeMnNi-0.5C specimens of undeformed and deformed states is shown in Fig. 4.2. by the means of EBSD inverse pole figure (IPF) and image quality (IQ) maps. Equiaxial recrystallized gains are observed after annealing at 1,373K for 1 hour as shown in Fig. 4.2 (a). Visible annealing twins exist in most grain and the average grain size without counting twin boundaries is ~128 μm. Only FCC solid solution phase is found without visible precipitates, which is also confirmed by neutron diffraction. Fig. 4.2 (b) is the IPF image showing deformed microstructure after fracture at room temperature, where extensive parallel deformation twin bands are observed. The twin bands are nearly equal spacing with a width of about 20 μm in the observed grains. Some twin bands cross through the grain with the orientation of <111>//LD. A few spots with uniform color observed at grain boundary and inside the grain distort the twin bands, which are expected to be carbide precipitates (the amount is not enough for being detected by neutrons) even through EBSD failed to identify them. The scanning along the back line in Fig. 4.2 (b) shows 60° misorientation in Fig. 4.2 (c), indicating these boundaries are Σ3 twins with surroundings. High resolution IPF image in Fig. 4.2 (d) indicates that the individual twins are less than 20 nm and the twin bundle can exceed 3μm. By converting the IPF image to loading direction inverse pole figure, it is clearly found the twinning orientation as <115>//LD and parent orientation as <111>//LD, which agrees with calculation of twinning. The uneven color indicates the orientation fluctuation inside the

deformation twins. More interestingly, microbands are observed in the grain oriented close <100>//LD (red color). When the tensile testing temperature is increased to 573K, the deformation twin is significantly postponed. Annealing twins still exist, but no deformation twin bands are seen in Fig. 4.2 (e) even after fracture. Sever orientation fluctuation is found in the grain close to <100>//LD orientation. However, <111>//LD oriented grains exhibit less orientation fluctuation. Different from deformation twin formed at 293K, narrow microbands are observed at 573K and the IQ map provides a clearer view of microbands in Fig. 4.2 (f). Similar microbands were also found in a different carbon contained HEA [10] and steels [30]. It is also found that some black spots suspected to be carbides are distributed inside grains in Fig. 4.2 (e).

3.3 Neutron diffraction

A representative neutron diffraction pattern of annealed CoCrFeMnNi-0.5C specimen at 1,373K is illustrated in Fig. 4.3. The diffraction pattern indicates a single-phase FCC solid solution was obtained after annealing without detecting any intermetallic or the small carbide precipitates. There is also no secondary phase found during and after tensile deformation at both temperatures.

Fig. 4.4 (a)-(f) present the *in-situ* neutron diffraction results of tension at 293K and 573K. The lattice strain evolution as a function of applied stresses is shown in Fig. 4.4 (a) and (b), where the solid square lines indicate the lattice strain along loading direction while the open square lines indicate the lattice strain along transverse direction. Firstly, the lattice strain at 293K increases linearly below 200 MPa, and it increases linearly below 160 MPa at 573K during the macroscopic elastic deformation. Then after yield, clear transition

points can be found indicating the stress-lattice strain relationship becomes nonlinear, i.e., the lattice strains deviate from the original elastic linearity significantly. The slopes of each orientation are linearly fitted to provide the diffraction elastic moduli (E_{hkl}), which is summarized in Table 4.1. The (111) grains exhibit the highest diffraction elastic modulus while (100) grains possess lowest diffraction elastic modulus. The Young's modulus anisotropy (E_{111}/E_{200}) increases from 1.72 to 1.83 with temperature elevated to 573K. In the plastic deformation the load is redistributed according to different crystallography orientation. In detail, the load transfers from 'softer' oriented grains, e.g. (220), to 'harder' oriented grain, e.g. (200). As a result, the (200) lattice strain increases the most greatly to bear more load as the applied stress increases, while the (311) and (111) lattice strain evolution is more linear. Note that high fluctuation of the (220) lattice strain derives from the uncertainty of fitting low-intensity peaks where texture evolution plays an important role. The slope of lattice strain for the (200) grains drops after yield also indicates that the (200) grains possess a high directional strength-to-stiffness [31], which will accommodate more load when the specimen is further tensioned. Compared two different temperatures, the lattice strain evolution is similar but claims different load distributions. For example, when the stress is applied to 500MPa, the (311) lattice strain at 293K is 2490 microstrain (10^{-6}) while that value at 573K is much higher as 3190 microstrain. Considering the diffraction elastic modulus, however, the (311) grains accommodates less load ($\varepsilon_{hkl} \times E_{hkl}$) when the specimen deformed at higher temperature. Furthermore, the lattice strain distribution of (111), (220) and (311) diffraction is further away from each other at 573K, indicating temperature increase the plastic anisotropy. But the (200) lattice strain does not

increase so greatly as (111), (220) and (311) lattice strain by increasing temperature, showing that the (200) lattice strain deviates further from the others at 293K. It supposes that the formation of deformation twins at 293K moderates the load in (111) grains compared with that where there are no deformation twins at 573K, but the lattice strain does not show a significant difference. Poisson's effect can be found in the transvers direction initially. After macroscopic yield, load redistribution leads the lattice strains differently increasing. (220), (111), (311) transvers lattice strain almost overlap at 293K but they split significantly at 573K.

Fig. 4.4 (c) and (d) display the evolution of normalized intensity as a function of plastic strain during tensile deformation at 293K and 573K respectively. The change of peak intensity gives rise to the grain reorientation during the tensile deformation, which could be due to slip and/or formation of deformation twins. As seen in Fig .4 (c) and (d), the intensity of (111) diffraction increases while that of (110) diffraction decreases with the increasing strain, implying the (111) grains are gradually reoriented along LD and (110) grains rotate away from LD, which is similar to dislocation slipping induced fiber texture during tension in other FCC alloys [32, 33]. A significant difference between two temperatures is that intensity of (111) diffraction at 293K increases by a factor of 2.2 and that at 573K increases by a much larger factor of 4.5. Furthermore, the increasing intensity of (111) diffraction slows down at higher strain at 293K while it keeps increasing linearly at 573K. The drop of slope results from deformation twinning as the IPF indicates that the <115> twinning orientation in (111) grains causes the decreasing intensity of (111) diffraction [19, 34]. Slip included intensity increase is larger than twinning induced

intensity decrease, so the overall effect leads to the drop of intensity slope at 293K. On the other hand, the intensity keeps increasing with same rate because only dislocation slip dominates the deformation at 573K.The intensities of (200) and (311) diffraction increase at 573K which is typical behavior in FCC materials but they slightly decrease at 293K. Strangely, the decreasing intensity of (200) upon plastic deformation at 293K, is different from a common FCC, even with twinning activities [19]. The underlining reason is not clear.

The peak width of (111) and (200) diffraction is deduced from full width at half maximum by subtracting the instrument broadening. The evolution of peak width ($\Delta d / d$) as a function of plastic strain is displayed in Fig. 4.4 (e) and (f). Fig .4.4 (e) shows that the peak width increases with strain initially, then transits to a constant evolution and drops at the end of deformation at 293K. Whereas, the peak width at elevated temperature increases monotonically during the entire plastic deformation as shown in Fig. 4.4 (f). The change of peak width can be used to investigate the deformation heterogeneities (such as dislocation, stacking fault) which contribute to peak broadening [25, 35, 36]. The slope transition of the peak width can be regarded as a sign of deformation twinning based on the above EBSD observation of deformation twins and the slope change of intensity evolution, which also agrees with the finding of deformation twinning onset at the strain level around 32.5% [9].

3.4 Texture

The crystallographic texture of undeformed and deformed states is characterized by ODF and LDIPF at room temperatures. Fig. 4.5 presents the neutron diffraction determined texture in loading direction. The ODF at sections of ϕ_2=45° are illustrated to investigate the main texture components. As seen in Fig. 4.5 (a), the initial texture of annealed specimen consists of strong (112)[-110] texture with the highest intensity of 4, followed by (001)[-1-10] and (111)[0-11] texture components. Even the annealing process completely recrystallizes the deformed grains after rolling, but the rolling texture is not fully eliminated. Accordingly, the LDIFP of undeformed specimen in Fig. 4.5 (b) illustrates <112>//LD texture component. After deformation at 293K to fracture, the texture reflects a combination of twinning and slip. Dislocation slip induced fiber texture is specified as (111)[2-31], (111)[1-21] and (111)[-1-12] texture components in the ODF at section of ϕ_2=45° in Fig. 4.5 (c). The texture component is marked as a star is (115)[-5-52] orientation, which is a typical twinning texture component in FCC metals [37]. A strong fiber texture <111>//LD is induced by dislocation slip, as shown in Fig. 4.5 (d), with a noticeably strong texture component near <115>//LD attributed to the formation of deformation twins. Similar to twinning-induced plasticity steels [38], twinning occurs in {111}<112> twin system and transforms to {511}<255> orientation, which generates <115>//LD in LDIPF. The twinning texture component of ODF is in accordance with the result of EBSD in the local area in Fig. 4.2 (d).

4. Discussion

The purpose of the current work is to elucidate the deformation mechanism and micromechanical behaviors by fully utilizing in-situ neutron diffraction. Following investigation will be discussed on the elastic and plastic deformations.

To better understand elastic deformation of current alloy and the effect of carbon on elastic properties at different temperatures, the well-known Kroner model [39] is applied by analyzing diffraction elastic moduli (Table 4.1) obtained by in-situ neutron diffraction. The diffraction elastic behavior varies from differently oriented grains due to the crystallographic elastic anisotropy. The diffraction elastic modulus is plotted as a function of the cubic elastic anisotropy factor (A_{hkl}) in Fig. 4.6. The cubic elastic anisotropy factor (A_{hkl}) is defined as

$$A_{hkl} = \frac{h^2k^2 + k^2l^2 + h^2l^2}{\left(h^2 + k^2 + l^2\right)^2} \quad (2).$$

The relation of diffraction elastic modulus and A_{hkl} is correlated through single-crystal elastic constants in Kroner model. Deriving from Kroner model by self-consistent method [40], the single-crystal elastic constants of the current alloys at different temperature are obtained. The calculated curves by Kroner model are plotted in Fig. 4.6 as well as the experimental results, indicating the model can describe the elastic behaviors reasonably well in the current alloys. The corresponding elastic constants, shear anisotropy and bulk modulus are summarized in Table 4.2, which can be used for simulation methods like crystal plasticity finite element method and elasto-plastic self-consistent modeling. It is found that the elastic constants of the current alloys are c_{11}=227.1GPa, c_{12}=158.7GPa and

c_{44}=135.7 at 293K, while c_{11}=199.5GPa, c_{12}=138.2GPa, c_{44}=122.2GPa at 573K, respectively. The bulk modulus reduces with the increased temperature, but the shear anisotropy changes a little. Comparing with the elastic properties of CrCoFeMnNi HEA [26], the addition of carbon enhances the bulk modulus significantly from 158.5GPa to 209.1GPa at room temperature. The shear modulus also increases from 2.84 to 3.97 by adding 0.5 at. % carbon. High elastic anisotropy is considered to cause deformation complexity since different grain family experiences significantly different stresses. The (200) grains might be expected to yield relatively early based on the Schmidt factor and the applied stress, but experimentally grain family such as (220) and (331) would yield first showing the lattice strain curve upwards into compression. This upwards curving is not quite distinct in Fig. 4.4, which might indicate the elastic anisotropy is still low even with carbon added.

While the plots such as in Fig. 4.4 (a) and (b) show both the elastic and plastic contribution to total intergranular lattice strain of different grain families, it can be instructive to only investigate the plastic intergranular strain. An alternative investigation of micromechanical behavior is to derive the intergranular strain ε_r, which is the different between the total lattice strain ε_{hkl} and the extrapolated line along elastic modulus E_{hkl}, define as $\varepsilon_r = \varepsilon_{hkl} - \sigma/E_{hkl}$, where σ is the applied stress. The intergranular strains of (111), (200), (220) and (311) grain families are plotted as a function of plastic strain in Fig. 4.7. It is found in Fig. 4.7(a) that the (200) grains experience the largest intergranular strain with the highest slope, which elucidates such grains bear the largest share of the applied stresses and move into tension relative to elastic linearity. The (111) and (311) grains show

increasing intergranular strain with smaller slopes compared to the (200) grains. Interestingly the intergranular strain of the (220) grains fluctuates around a constant close to zero and the fluctuation increased when the specimen is further strained. The deformation twins form at a relative larger strain level; however, the twinning does not affect the stress redistribution significantly as evidenced in Fig. 4.7 (a). Behavior of intergranular strain evolution at 573K is shown in Fig. 4.7 (b). The trend of intergranular strain evolution is similar to that at 293K, but the magnitude is slightly smaller, especially for the (200) grains. Considering the abnormal change of (200) intensity in Fig. 4.4 (c), the fact that (200) grains rotates away from loading direction could probably lead them to take more stress at 293K. The total lattice strain at a given macroscopic strain experiences reduction in magnitude from 293K to 573K. Two competing effects may take place as the temperature is elevated. High temperature would reduce the stress required for a given macroscopic strain, which hence reduces the total lattice strain. On the other hand, high temperature reduces the elastic moduli, which evidently leads to a larger lattice strain for a given applied stress. It also should be noted that based on composite mechanics, some other oriented grains should share compressive stresses to balance the overall tensile intergranular strain showed in Fig. 4.7.

Due to high penetration of neutron, neutron diffraction is considered as a perfect method to determine the bulk texture in metals and alloys. Being the direct result from in-situ neutron diffraction, the change of peak intensity is account to grain re-orientation during deformation, which can be induced by dislocation slip, rotation of grain, and/or the formation of deformation twins [25]. Generally, the formation of twinning in the grains

oriented to satisfy the diffraction condition could lead reduction of original grain diffraction intensity of the twinned region; on the other hand, new grains orientation that fit the diffraction condition can increase the diffraction intensity of such oriented grains [41]. As mentioned before, dislocation slip will increase the (111) peak intensity during uniaxial tensile deformation in FCC metals, while the formation of deformation twins does also affect the (111) peak intensity, that is, twinning in {111} system to {511} direction will reduce the (111) peak intensity. In other words, the change of (111) peak intensity is the convoluted competition of slip and twinning, so it becomes difficult to separate the contributions of slip and twinning to the measured peak intensity change. However, in the current study the contribution of twinning to (111) peak intensity is qualitatively determined by comparing the peak intensity change rate with the grain with and without deformation twinning in Fig. 4.4 (c) and (d), which is supported by EBSD microstructure observation. This finding agrees with the ex-situ study of twinning formed in the same alloy by EBSD [9]. Deformation twinning does not take place during the deformation at 573K, so the (111) intensity change is solely due to the grain reorientation by dislocation slip, showing a higher rate than that of (111) intensity change moderated by twinning during 293K tension. As a result, the peak intensity change is much smaller at 293K by a factor of 2.2 in Fig.4.4 (c). The ODF of deformed specimens further confirm the twinning orientation of (115)[-5-52] in Fig. 4.5. By calculation the twinning orientation from <111>//LD to <115>//LD, it turns out that a detector positioned at 141° to LD is expected to detect the intensity increasing of twinning region, which needs further investigation.

The current study manifests the improvements in mechanical properties of the carbon containing HEA compared to its substitutional HEAs are due to the multiple strengthening mechanisms, i.e. solid solution strengthening, twinning/microband induced plasticity. In the current studied HEAs without precipitates, the yield strength (σ_y) for annealed specimen can be described by [42]

$$\sigma_y = \sigma_r + \Delta\sigma_g \tag{3}$$

where σ_r is the lattice friction stress and $\Delta\sigma_g$ is the strengthening contribution from grain boundaries. Since the grain sizes are as large as 128 μm, the grain boundary strengthening effect

could be negligible. Hence, the major contribution to the increase in yield strength comes from the increase in lattice friction stress due to the carbon interstitial strengthening, similar to the behavior in other interstitial HEAs [11]. The yield strength reduces at elevated temperature of 573K is mainly due to the temperature dependence of lattice friction stress [43].

At the early stage of plastic deformation after yielding, dislocation movement is hindered by the interstitial carbon to increase the work hardening to a steady rate. Although the tendency of work hardening rate vs. strain curve looks similar, value of the hardening rate is larger for the curves deformed in room temperature, the difference might be attributed to the additional hardening because of the deformation twinning, which prompts additional dislocation-twining boundaries interactions [44, 45]. The increasing dislocation density induced by plastic deformation will cause the peak broadening of neutron diffraction. Similar to another carbon doped HEA [10], the lattice friction stress increased

sharply by the addiction of carbon, along with the reduction of staking fault energy (SFE), producing the transition of dislocation slip mode from wavy slip to planar slip. The strong solid solution hardening of the carbon interstitial atom makes the dislocation mediated plasticity (slips) much more difficult; thus, the critical stress needed to activate twinning can be easily achieved due to the increase in work hardening rate. The Shockley partial dislocations are more separated since the cross slip is inhibited with the reduction of SPF; thus the formation of deformation twin easily occurs when separated Shockley partial dislocations pass on every {111} slip plane [46], which results in the peak intensity change of (111) diffraction. The nano-sized deformation twinning mediates the plastic deformation instead of dislocation slip, which slows down the increase of peak width. Simultaneously, microbands form in the grains those are not favored for twinning by the calculation of Schmid factor, when perfect dislocations become hard to move; hence they move into localized bands [47]. The simultaneous formation of twins and microbands has been reported in several other materials [48-50], which is attributed to the role of grain orientation on both deformation twinning and microband formation. When the temperature is elevated, higher SPF and relatively lower work hardening postpone the formation of deformation twin; whereas, the microbands forms to dominate further plastic deformation.

5. Summary and conclusions

In summary, the study in the current work elucidates that the plastic deformation of CoCrFeMnNi-0.5C at room temperature is governed by dislocation slip at small strain level and then mediated by deformation twinning and microbands simultaneously; while at elevated temperature of 573K, it is controlled by dislocation slip at early stage but then

mediated by microbands at high strain level. The deformation mechanism and micromechanical behavior of CoCrFeMnNi-0.5C is investigated by in-situ neutron diffraction under uniaxial tensile deformation at 293K and 573K. The crystallographic texture of undeformed and deformed specimens is measured by ND. The main conclusions are:

1. The addition of 0.5 at. % carbon to CoCrFeMnNi HEA increases the yield strength, ultimate tensile stress, as well as work hardening compared to substitutional CoCrFeMnNi HEA.
2. The plastic deformation is dominated by dislocation slip at early stage at both temperatures. At high strain level, deformation is mediated simultaneously by deformation twins and microbands at 293K while it is governed solely by microbands at 573K.
3. The lattice strain evolution is similar to that in others FCC materials and the deformation twin does not affect the lattice strain evolution significantly compared with the micromechanical behaviors at both temperatures. The investigation of peak intensity and FWHM provides the alternative evidence of twinning activities.
4. The texture measurement represented by orientation distribution function indicates that the annealed specimens possesses a strong texture component of {112} <110>, and the tension deformed texture consists of slip induced fiber texture and twinning induced {115}<552> texture component.

References

[1] B. Cantor, I. Chang, P. Knight and A. Vincent: Microstructural development in equiatomic multicomponent alloys Materials Science and Engineering: A. 375, 213 (2004).

[2] J.W. Yeh, S.K. Chen, S.J. Lin, J.Y. Gan, T.S. Chin, T.T. Shun, C.H. Tsau and S.Y. Chang: Nanostructured high‐entropy alloys with multiple principal elements: novel alloy design concepts and outcomes Advanced Engineering Materials. 6(5), 299 (2004).

[3] Y. Jien-Wei: Recent progress in high entropy alloys Ann. Chim. Sci. Mat. 31(6), 633 (2006).

[4] M.-H. Tsai and J.-W. Yeh: High-entropy alloys: a critical review Materials Research Letters. 2(3), 107 (2014).

[5] B. Gludovatz, A. Hohenwarter, D. Catoor, E.H. Chang, E.P. George and R.O. Ritchie: A fracture-resistant high-entropy alloy for cryogenic applications Science. 345(6201), 1153 (2014).

[6] Y. Zhang, T.T. Zuo, Z. Tang, M.C. Gao, K.A. Dahmen, P.K. Liaw and Z.P. Lu: Microstructures and properties of high-entropy alloys Prog Mater Sci. 61, 1 (2014).

[7] Z. Lu, H. Wang, M. Chen, I. Baker, J. Yeh, C.T. Liu and T. Nieh: An assessment on the future development of high-entropy alloys: summary from a recent workshop Intermetallics. 66, 67 (2015).

[8] W. Zhang, P.K. Liaw and Y. Zhang: Science and technology in high-entropy alloys Science China Materials. 1 (2018).

[9] Z. Wu, C.M. Parish and H. Bei: Nano-twin mediated plasticity in carbon-containing FeNiCoCrMn high entropy alloys J Alloy Compd. 647, 815 (2015).

[10] Z. Wang, I. Baker, Z. Cai, S. Chen, J.D. Poplawsky and W. Guo: The effect of interstitial carbon on the mechanical properties and dislocation substructure evolution in Fe40.4Ni11.3Mn34.8Al7.5Cr6 high entropy alloys Acta Mater. 120, 228 (2016).

[11] Z. Wang and I. Baker: Interstitial strengthening of a fcc FeNiMnAlCr high entropy alloy Materials Letters. 180, 153 (2016).

[12] Y.C. Xie, H. Cheng, Q.H. Tang, W. Chen, W.K. Chen and P.Q. Dai: Effects of N addition on microstructure and mechanical properties of CoCrFeNiMn high entropy alloy produced by mechanical alloying and vacuum hot pressing sintering Intermetallics. 93, 228 (2018).

[13] T.D. Huang, L. Jiang, C.L. Zhang, H. Jiang, Y.P. Lu and T.J. Li: Effect of carbon addition on the microstructure and mechanical properties of CoCrFeNi high entropy alloy Sci China Technol Sc. 61(1), 117 (2018).

[14] N. Stepanov, N.Y. Yurchenko, M. Tikhonovsky and G. Salishchev: Effect of carbon content and annealing on structure and hardness of the CoCrFeNiMn-based high entropy alloys J Alloy Compd. 687, 59 (2016).

[15] N.D. Stepanov, D.G. Shaysultanov, R.S. Chernichenko, N.Y. Yurchenko, S.V. Zherebtsov, M.A. Tikhonovsky and G.A. Salishchev: Effect of thermomechanical processing on microstructure and mechanical properties of the carbon-containing CoCrFeNiMn high entropy alloy J Alloy Compd. 693, 394 (2017).

[16] D. Yu, K. An, Y. Chen and X. Chen: Revealing the cyclic hardening mechanism of an austenitic stainless steel by real-time in situ neutron diffraction Scripta Mater. 89, 45 (2014).

[17] S. Agnew, A. Singh, C. Calhoun, R. Mulay, J. Bhattacharyya, H. Somekawa, T. Mukai, B. Clausen and P. Wu: In-situ neutron diffraction of a quasicrystal-containing Mg alloy interpreted using a new polycrystal plasticity model of hardening due to {10.2} tensile twinning International Journal of Plasticity. 100, 34 (2018).

[18] R. Voothaluru, V. Bedekar, Q. Xie, A.D. Stoica, R.S. Hyde and K. An: In-situ neutron diffraction and crystal plasticity finite element modeling to study the kinematic stability of retained austenite in bearing steels Materials Science and Engineering: A. 711, 579 (2018).

[19] Q. Xie, J. Liang, A.D. Stoica, R. Li, P. Yang, Z. Zhao, J. Wang, H. Lan and K. An: In-situ neutron diffraction study on the tension-compression fatigue behavior of a twinning induced plasticity steel Scripta Mater. 137, 83 (2017).

[20] Y. Wu, D. Ma, Q. Li, A. Stoica, W. Song, H. Wang, X. Liu, G. Stoica, G. Wang and K. An: Transformation-induced plasticity in bulk metallic glass composites evidenced by in-situ neutron diffraction Acta Mater. 124, 478 (2017).

[21] Q. Xie, Y. Chen, P. Yang, Z. Zhao, Y. Wang and K. An: In-situ neutron diffraction investigation on twinning/detwinning activities during tension-compression load reversal in a twinning induced plasticity steel Scripta Mater. 150, 168 (2018).

[22] W. Wu, K. An, L. Huang, S.Y. Lee and P.K. Liaw: Deformation dynamics study of a wrought magnesium alloy by real-time in situ neutron diffraction Scripta Mater. 69(5), 358 (2013).

[23] S. Van Petegem, J. Wagner, T. Panzner, M. Upadhyay, T. Trang and H. Van Swygenhoven: In-situ neutron diffraction during biaxial deformation Acta Mater. 105, 404 (2016).

[24] E.-W. Huang, D. Yu, J.-W. Yeh, C. Lee, K. An and S.-Y. Tu: A study of lattice elasticity from low entropy metals to medium and high entropy alloys Scripta Mater. 101, 32 (2015).

[25] W. Woo, E.W. Huang, J.W. Yeh, H. Choo, C. Lee and S.Y. Tu: In-situ neutron diffraction studies on high-temperature deformation behavior in a CoCrFeMnNi high entropy alloy Intermetallics. 62, 1 (2015).

[26] Y. Wu, W.H. Liu, X.L. Wang, D. Ma, A.D. Stoica, T.G. Nieh, Z.B. He and Z.P. Lu: In-situ neutron diffraction study of deformation behavior of a multi-component high-entropy alloy Appl Phys Lett. 104(5), (2014).

[27] B. Cai, B. Liu, S. Kabra, Y.Q. Wang, K. Yan, P.D. Lee and Y. Liu: Deformation mechanisms of Mo alloyed FeCoCrNi high entropy alloy: In situ neutron diffraction Acta Mater. 127, 471 (2017).

[28] G. Laplanche, A. Kostka, O. Horst, G. Eggeler and E. George: Microstructure evolution and critical stress for twinning in the CrMnFeCoNi high-entropy alloy Acta Mater. 118, 152 (2016).

[29] K. An, H.D. Skorpenske, A.D. Stoica, D. Ma, X.L. Wang and E. Cakmak: First In Situ Lattice Strains Measurements Under Load at VULCAN Metall Mater Trans A. 42A(1), 95 (2011).

[30] J.D. Yoo and K.T. Park: Microband-induced plasticity in a high Mn-Al-C light steel Mat Sci Eng a-Struct. 496(1-2), 417 (2008).

[31] A.A. Saleh, E.V. Pereloma, B. Clausen, D.W. Brown, C.N. Tome and A.A. Gazder: Self-consistent modelling of lattice strains during the in-situ tensile loading of twinning induced plasticity steel Mat Sci Eng a-Struct. 589, 66 (2014).

[32] E.W. Huang, R. Barabash, N. Jia, Y.D. Wang, G. Ice, B. Clausen, J. Horton and P.K. Liaw: Slip-System-Related Dislocation Study from In-Situ Neutron Measurements Metall Mater Trans A. 39a(13), 3079 (2008).

[33] S. Kabra, S. Danion, W. Kockelmann and S.Y. Zhang: A neutron diffraction study of texture evolution under deformation in a hot rolled TWIP steel Mater Today-Proc. 2, 261 (2015).

[34] T.K. Liu, Z. Wu, A.D. Stoica, Q. Xie, W. Wu, Y.F. Gao, H. Bei and K. An: Twinning-mediated work hardening and texture evolution in CrCoFeMnNi high entropy alloys at cryogenic temperature Mater Design. 131, 419 (2017).

[35] T. Ungar, J. Gubicza, G. Ribarik and A. Borbely: Crystallite size distribution and dislocation structure determined by diffraction profile analysis: principles and practical application to cubic and hexagonal crystals J Appl Crystallogr. 34, 298 (2001).

[36] T. Ungar, G. Ribarik, J. Gubicza and P. Hanak: Dislocation structure and crystallite size distribution in plastically deformed metals determined by diffraction peak profile analysis J Eng Mater-T Asme. 124(1), 2 (2002).

[37] J.W. Christian and S. Mahajan: Deformation Twinning Prog Mater Sci. 39(1-2), 1 (1995).

[38] K. Yan, D.G. Carr, M.D. Callaghan, K.D. Liss and H.J. Li: Deformation mechanisms of twinning-induced plasticity steels: In situ synchrotron characterization and modeling Scripta Mater. 62(5), 246 (2010).

[39] E. Kröner: Berechnung der elastischen Konstanten des Vielkristalls aus den Konstanten des Einkristalls Zeitschrift für Physik. 151(4), 504 (1958).

[40] Z. Wang, A.D. Stoica, D. Ma and A.M. Beese: Diffraction and single-crystal elastic constants of Inconel 625 at room and elevated temperatures determined by neutron diffraction Materials Science and Engineering: A. 674, 406 (2016).

[41] D. Brown, M. Bourke, M. Stout, P. Dunn, R. Field and D. Thoma: Uniaxial tensile deformation of uranium 6 wt pct niobium: a neutron diffraction study of deformation twinning Metallurgical and Materials Transactions A. 32(9), 2219 (2001).

[42] Z. Wu, Y. Gao and H. Bei: Thermal activation mechanisms and Labusch-type strengthening analysis for a family of high-entropy and equiatomic solid-solution alloys Acta Mater. 120, 108 (2016).

[43] C. Varvenne, A. Luque and W.A. Curtin: Theory of strengthening in fcc high entropy alloys Acta Mater. 118, 164 (2016).

[44] H. Idrissi, K. Renard, L. Ryelandt, D. Schryvers and P. Jacques: On the mechanism of twin formation in Fe–Mn–C TWIP steels Acta Mater. 58(7), 2464 (2010).

[45] K. Rahman, V. Vorontsov and D. Dye: The effect of grain size on the twin initiation stress in a TWIP steel Acta Mater. 89, 247 (2015).

[46] S. Mahajan and G. Chin: Formation of deformation twins in fcc crystals Acta metallurgica. 21(10), 1353 (1973).

[47] J.D. Yoo and K.-T. Park: Microband-induced plasticity in a high Mn–Al–C light steel Materials Science and Engineering: A. 496(1-2), 417 (2008).

[48] I. Gutierrez-Urrutia and D. Raabe: Multistage strain hardening through dislocation substructure and twinning in a high strength and ductile weight-reduced Fe–Mn–Al–C steel Acta Mater. 60(16), 5791 (2012).

[49] O. Bouaziz, S. Allain, C. Scott, P. Cugy and D. Barbier: High manganese austenitic twinning induced plasticity steels: A review of the microstructure properties relationships Current opinion in solid state and materials science. 15(4), 141 (2011).

[50] R.J. McCabe, I.J. Beyerlein, J.S. Carpenter and N.A. Mara: The critical role of grain orientation and applied stress in nanoscale twinning Nature communications. 5, 3806 (2014).

Appendix 4

Table 4.1 Diffraction elastic modulus of different grain families in the current CoCrFeMnNi0.5C HEA at test temperature (unit: GPa).

	E_{111}	E_{200}	E_{220}	E_{311}	Young's modulus anisotropy (E_{111} /E_{200})
293K	259.5	150.6	248.4	191.2	1.72
573K	248.9	136.2	237.2	149.7	1.83

Table 4.2 Single-crystal elastic constants and anisotropy of the CoCrFeMnNi0.5C alloys in comparison with those of CoCrFeMnNi without carbon

	C_{11} (GPa)	C_{12} (GPa)	C_{44} (GPa)	Shear Anisotropy 2 C_{44}/(C_{11}-C_{12})	Bulk modulus (GPa)
CoCrFeMnNi0.5C (293K)	227.1	158.7	135.7	3.97	209.1
CoCrFeMnNi0.5C (573K)	199.5	138.2	122.2	3.99	187.3
CoCrFeMnNi [26]	172.1	107.5	92	2.84	158.5

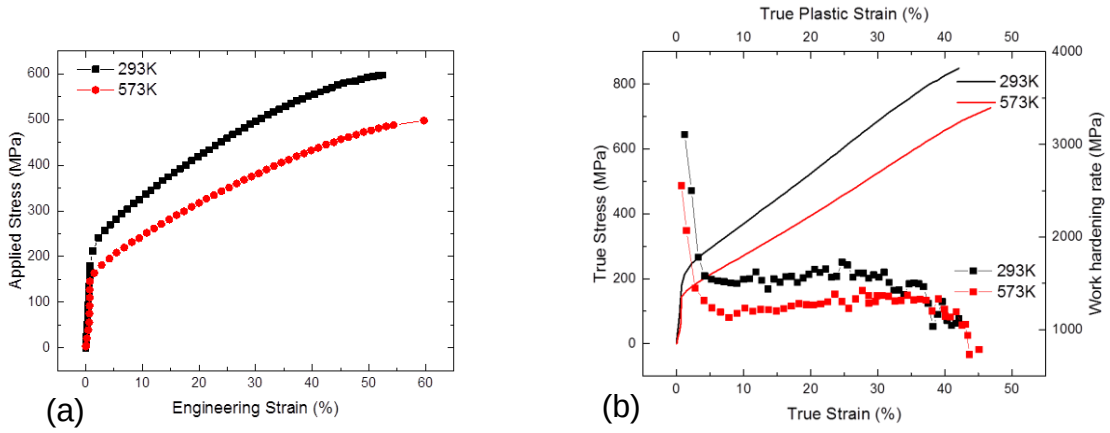

Fig. 4.1 (a) Engineering stress-strain curves, (b) true stress-strain curves and work hardening rate as a function of true plastic strain of tensile tests at 293K and 573K.

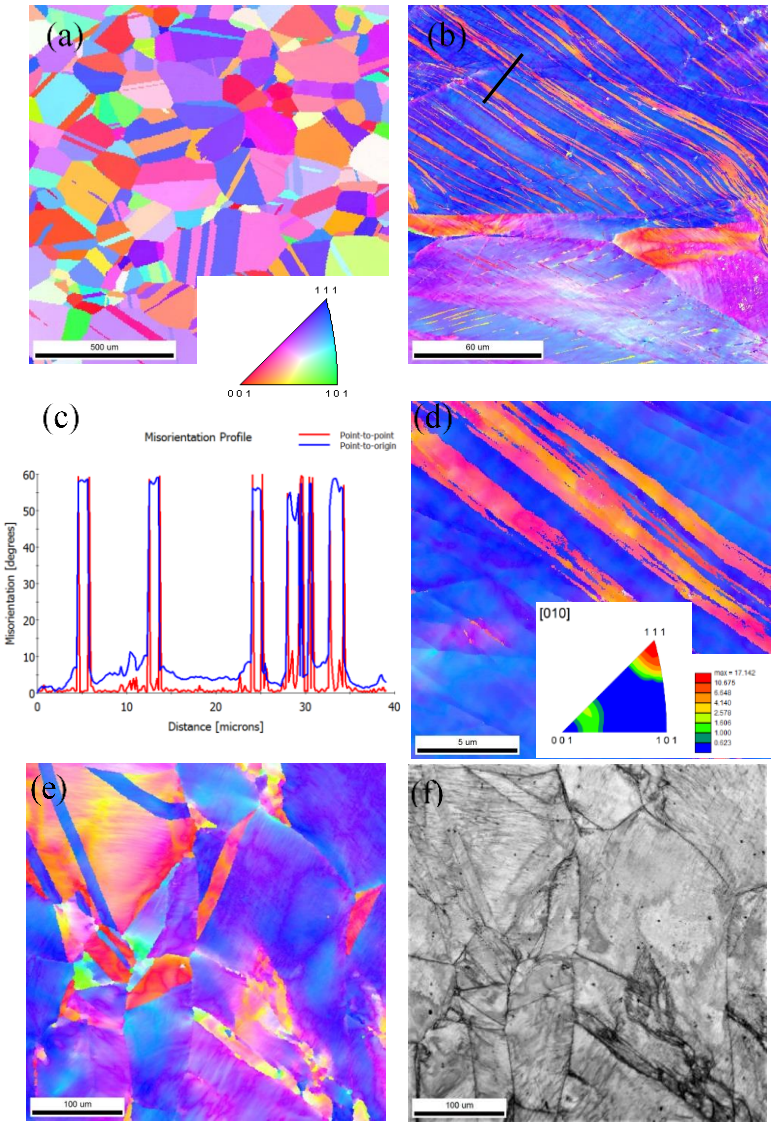

Fig. 4.2 Microstructure of CoCrFeMnNi-0.5C specimens of undeformed and deformed states: (a) EBSD IPF image of annealed microstructure (undeformed), (b) EBSD IPF image of microstructure deformed at 293K, (c) misorientation profile along the black line in (b), (d) high resolution EBSD IPF image showing deformation twins of the specimen deformed at 293K with inserted LD inverse pole figure, (e) EBSD image and (f) image quality map of specimen deformed at 573K. The IPF coloring is projected to LD.

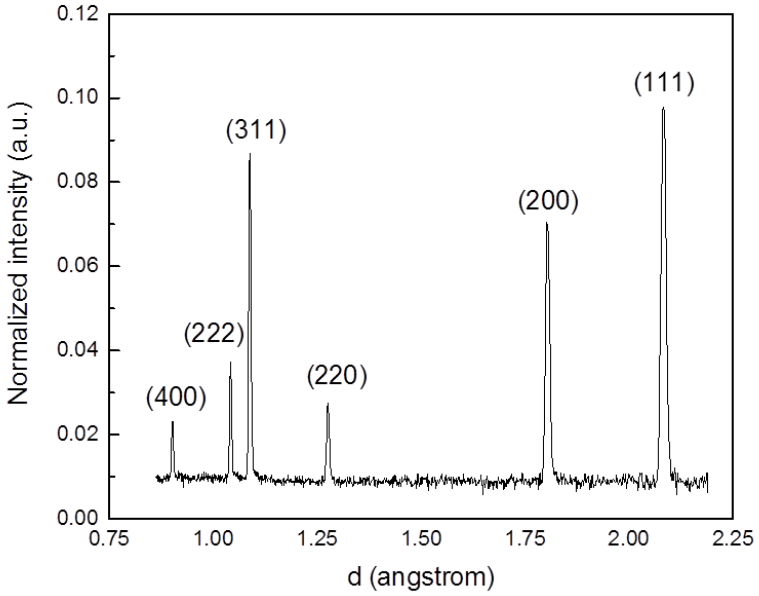

Fig. 4.3 Representative neutron diffraction pattern of CoCrFeMnNi-0.5C specimen annealed at 1,373K

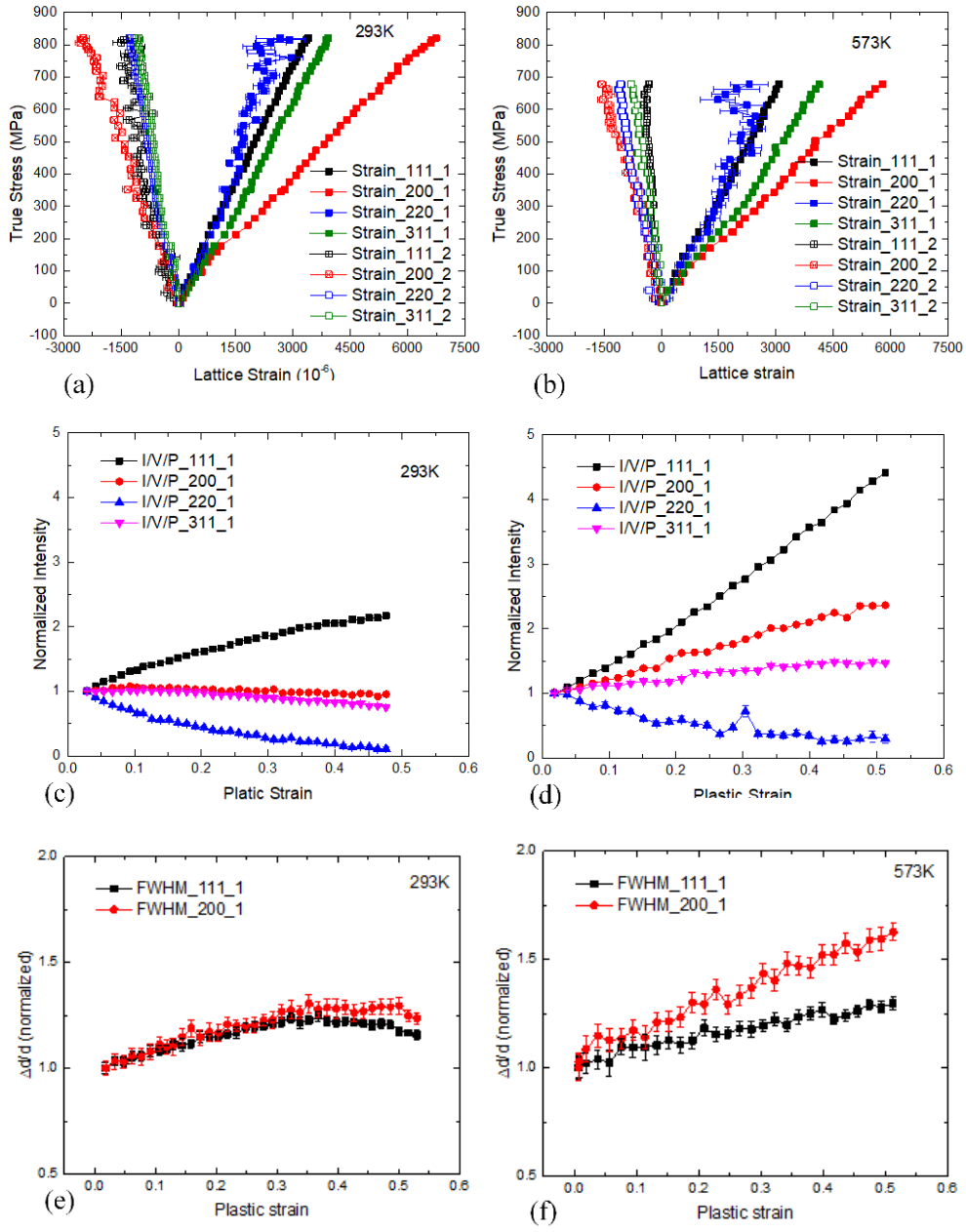

Fig. 4.4 Evolution of lattice strain during tension at (a) 293K and (b) 573K; normalized intensity evolution as a function of plastic strain during tension at (a) 293K and (b) 573K; normalized peak width as a function of plastic strain during tension at (a) 293K and (b) 573K.

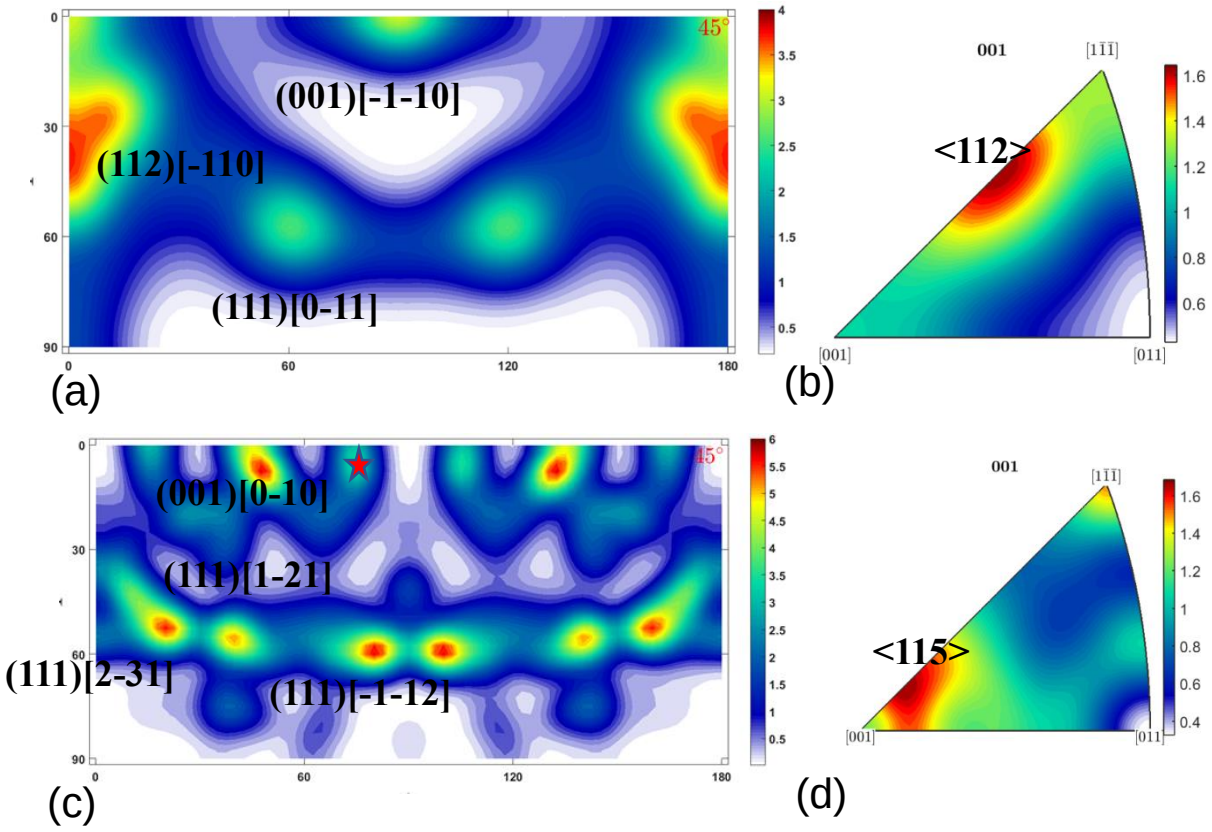

Fig. 4.5 (a) ODF at section of φ_2=45° and (b) loading direction inverse pole figure of the undeformed specimen; (c) ODF at section of φ_2=45° and (b) loading direction inverse pole figure of the specimen after tension test at 293K.

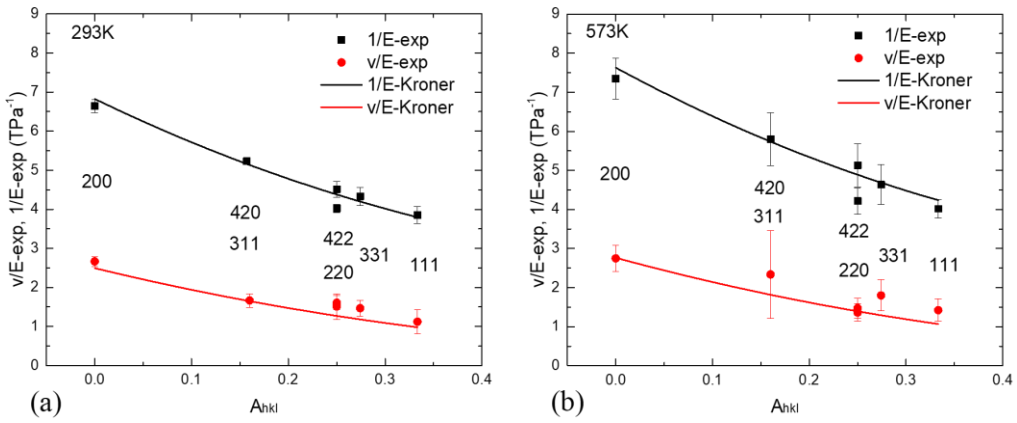

Fig. 4.6 Elastic moduli plotted as a function of elastic anisotropy factor A_{hkl} and fitted with the Kroner model at (a) 293K and (b) 573K. v is the Poisson's ratio and E is the diffraction elastic modulus.

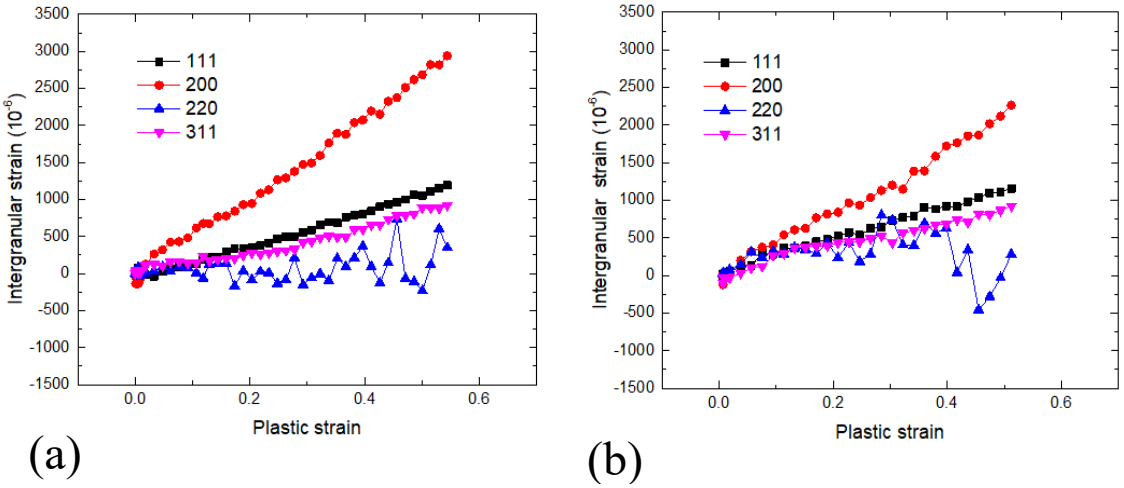

Fig. 4.7 Intergranular strain as a function of plastic strain at (a) 293K and (b) 573K

CONCLUSION

With the advancement of alloy design, more and more elements are applied to the alloys to achieve desired machinal and physical properties. Recently, two classes of chemically complex multicomponent alloys, bulk metallic glasses (BMGs) and high entropy alloys (HEAs), were developed to be potentially utilized as the promising structural and functional materials. Both of the two kinds of materials exhibit excellent mechanical properties such as ultrahigh strength and fracture toughness. The deformation of BMG at room temperature concentrates locally in shear bands controlled by so-called structural heterogeneities. Even crystalline alloys deform locally at the length scales of micro and nanometer featured by planer slip, twining and so on depending on materials and circumstance. Therefore, in such chemically complex multicomponent alloys, the exploration of structural and deformation heterogeneities is the key to uncover the structure-property relationship and to understand underlying deformation mechanisms.

Pre-deformation have been found to be effective methods to enhance ductility by increasing structural heterogeneities in BMGs. Nanoindentation pop-in test is powerful as a mechanical probe of the microscopic structural heterogeneities. A computational method by unifying the homogenous shear band nucleation process and heterogeneous shear band nucleation process characterizes the deformation induced defects as the plastic flow carriers structurally and mechanically. The results indicate that the pre-stress by elastic bending and residual stress by plastic bending of BMG plates dramatically increased density of structural heterogeneity and thus mechanically rejuvenated the glass structure to more deformable states.

In the study of ion irradiation effect on structural and mechanical changes in Zr-base BMGs, mechanical softening and a transition to new amorphous state are observed. The irradiation-induced defects are quantitatively predicted by a statistic model, suggesting those defects increased with the irradiation doses but their strength decreased. Supported with micro-pillar compression tests, all the experimental and numerical findings suggested irradiation induced a different amorphous state from annealing and proved ion irradiation as an effective method to tune the structure and mechanical properties of metallic glasses.

Of most HEAs, CrCoFeMnNi alloys have been studied the most widely, which is single phase solid solution with simple face centered cubic structure. To study the deformation mechanism and texture evolution of CrCoFeMnNi HEAs, electron microscopy and neutron diffraction techniques were adopted. The deformation induced microstructure and texture change was investigated by multiple interrupted cryogenic tensile tests. The micromechanical behavior of carbon strengthened CrCoFeMnNi0.5C HEAs was studied by in situ neutron diffraction. To control the twinning activity, the tensile tests were proposed to conduct at both room temperature and elevated time temperature, since twinning takes place at ambient deformation while it is supposed not to happen at elevated temperature.

The investigation of cryogenic plastic deformation of CrCoFeMnNi indicated that the deformation twins led to the Stage-II constant work hardening rate and resulted in the appearance of <115>//TA texture component, while the dislocation slip was involved all though the entire plastic deformation. The twinning-mediated tensile plastic deformation at cryogenic temperature finally induced the strong {111}<112> texture component and

minor {001}<110> texture component accompanied with twinning-induced {115}<552> texture component.

With in-situ results accompanied with microstructure and texture measurement to investigate CoCrFeMnNi0.5C HEAs, it was found that the plastic deformation is dominated by dislocation slip at an early stage at both room and elevated temperatures. However, at high strain level, deformation is mediated simultaneously by deformation twins and microbands at room temperature, while it is governed solely by microbands at elevated temperature 573K. The evolution of lattice strain, peak intensity and peak width from in-situ neutron diffraction elucidates the micromechanical behaviors regarding to the role of slips and twins. The texture represented by orientation distribution function indicates that the annealed specimen possesses a relatively strong {112}<110> texture component, and the room-temperature tension deformed texture comprises of slip induced fiber texture and twinning induced {115}<552> texture component.

However, the clear definition of structural heterogeneities in BMGs is still missing. Further investigations are needed to discover the atomic structure of structural heterogeneities by experimental methods and numerical simulations. Since simple solid solution strengthening concepts are not adequate for HEAs, deep investigations are necessary to understand the structure and deformation mechanism in atomistic scales.

VITA

Tingkun Liu was born in Changchun, China in 1987. He entered the School of Materials at Beijing Institute of Technology in 2006 and received a bachelor's degree and master's degree in Materials Science and Engineering in 2010 and 2013, respectively. After two-year work at Shanghai Synchrotron Radiation Facility, he started to pursue a doctorate degree in Materials Science and Engineering at the University of Tennessee in 2015. After four-year study and research, He was awarded the PhD degree in 2019.